

Characterization of photoacoustic sources in tissue using time domain measurements

John Andrew Viator

B.S., Physics, University of Washington (1985)

M.S., Mathematics, University of Oregon (1993)

M.S., Applied Physics, Oregon Graduate Institute
of Science and Technology (1997)

A dissertation submitted to the faculty of the
Oregon Graduate Institute of Science & Technology
in partial fulfillment of the
requirements for the degree
Doctor of Philosophy
in
Electrical and Computer Engineering

August 2000

The dissertation “Characterization of photoacoustic sources in tissue using time domain measurements” by John Andrew Viator has been examined and approved by the following Examination Committee:

Scott A. Prah
Assistant Professor
Thesis Research Advisor

Steven L. Jacques
Professor

Kenton W. Gregory
Associate Professor
Director
Oregon Medical Laser Center

J. Fred Holmes
Professor

Dedication

To my parents, John D. and Fujiko G. Viator

Acknowledgements

My thanks should begin with my academic advisors and mentors. First, my primary advisor, Professor Scott A. Prahl, who has given me the opportunity to become a good scientist. He has taught me how to conduct research, how to read scientific papers, and how to give a good scientific talk. These gifts aren't trivial and my future success as a scientist will rest the solid foundation he has made. I also thank my secondary advisor, Professor Steven L. Jacques, who had introduced me to the fascinating realm of photoacoustics. His support, intellectual and financial, were integral in all of my investigations summarized in this dissertation. My gratitude to Steve cannot be expressed enough in these acknowledgments. I would also like to acknowledge Dr. Guenther Paltauf for his help in all phases of this dissertation research. I could not have done this work without his guidance and help. Having one of the world's leading experts in photoacoustics on hand during my research was probably the biggest factor in the success of this dissertation. He and Jolanta always showed me the way with kindness and grace. Finally, to Dr. Kenton W. Gregory, the Director of the Oregon Medical Laser Center, where I spent my research years while matriculated at OGI, I offer my most heartfelt thanks for providing me the opportunity to work with such an outstanding research group. His advice and encouragement has sustained me during my work at OMLC. Also, through OMLC, my work was supported by the Department of Energy, DE-FG03-97-ER62346 and by the Department of the Army Combat Casualty Care Division, US AMRMC contract 95221N-02.

I would like to thank my fellow student, Paulo Bargo, for his constant support. He was the perfect sounding board for my vented frustrations, academic and otherwise. I also thank the other students, Jessica, Ted, Dan, and Jin Shan. I wish them bright futures. I also acknowledge the students, long since graduated, who were at OMLC and OGI when I first arrived, including Ujwal, who gave me an ambitious standard to strive toward. I also

thank HanQun, whom I miss, for his help in my early work. His memory will stay with me always. Thanks also to Sean, Krishna, and Badri.

I must thank the personnel of OMLC. First, to Lisa Buckley, who has been at OMLC since the beginning and maintains the corporate memory of the research center. Her enduring and unconditional kindness is baffling. I also thank the research nurses, Deb Bahlman, Jeff Teach, and Teresa Goodell for teaching me about the principle of indiscriminate care. I must also thank Rob Forrest and Sue Larson for their strong administrative support at OMLC. Sue has been a particular bright spot in my research career. I also thank David Spain for his practical and artistic insights into design and building of experimental devices. To the surgical fellows, especially Yasmin Wadia and Hua Xie, I owe a debt of gratitude for their perspective on clinical application and for their friendship and stock tips. I cannot thank Rui Qing Qian enough for his kindness and wisdom. I thank all of the research assistants, including Jenny, Dhruv, Chris and Dan Sturges, Mason, Kwong, Kristi, and Andrew. A double thanks to Halina Brant-Zawadzki for her excellent medical illustrations and her willingness to give me pie and candy.

I'd like to thank the faculty of the Electrical and Computer Engineering Department, the department formerly known as Electrical Engineering, formerly Electrical Engineering and Applied Physics. My deepest thanks to Professor Robert Jaffe, the first person I met at OGI. His kindness and concern for the students were unmatched by any other faculty person I knew at OGI. I'd also like to thank Professor Fred Holmes, Captain, USNR (ret.), for his perspective on science and engineering and the Navy. I also thank Anne Herman, the OGI Registrar, for her amazing ability to cut through red tape. And I thank President Ed Thompson, for his interest in my progress and goals.

I must thank my professors from the University of Oregon, who helped me gain admission and funded support at OGI. To Professor's Leahy, Isenberg, and Koch of the Mathematics Department and Professor Gregory of the Physics Department, I owe them much for helping me attain this goal. They taught me much about mathematics, but also, their enthusiasm at the blackboard inspires me whenever I give a public talk.

I give thanks to a whole line of friends who have supported me in so many ways during my years at OGI, including Johan, Montse, and Frederik, who have seen me through

most of my Phd studies and supported me with kindness and great conversation. Also, I thank Bernie, Beth, and Gary Gofstein. And I thank Dan and Paula Taylor, who always believed in me. I thank Joe Dowling, whose prayers have sustained me throughout the years. Professor Dr. Yoshihiro Misono was my academic inspiration. And I thank Shannon, my most ardent and wonderful supporter. Finally, my greatest thanks goes to my family, especially my parents, John D. and Fujiko G. Viator, who are responsible for all of my good fortune and accomplishments.

Contents

Dedication	iii
Acknowledgements	iv
List of Tables	xii
List of Figures	xiii
Abstract	xxiii
1 Introduction	1
1.1 Photoacoustic History	5
1.1.1 Photoacoustic Generation of Simple Sources	6
1.1.2 Cavitation and Photoacoustics	6
1.1.3 Photoacoustic Diagnostics and Imaging	7
1.2 Motivation: Medical Imaging	8
1.2.1 X-Ray Techniques	8
1.2.2 Ultrasound	9
1.2.3 Photoacoustic Imaging	10
1.2.4 Breast Cancer Diagnosis	11
1.3 The Current State and Future of Photoacoustic Methods in Biomedicine	11
1.3.1 Tomography and Imaging	11
1.3.2 Analytical Monitoring	13
1.3.3 Interaction of Light and Sound	13
1.4 Acoustic Propagation	14
1.4.1 Equations of State	14
1.4.2 Equation of Continuity	15
1.4.3 Euler Equation	15
1.4.4 Acoustic Wave Equation	16
1.4.5 Velocity Potential	16
1.4.6 Plane Waves	17

1.4.7	Acoustic Impedance	17
1.4.8	Spherical Waves	18
1.4.9	Cylindrical Waves	18
1.4.10	Boundary Conditions	19
1.4.11	Monopoles	19
1.4.12	Dipole Source	20
1.4.13	Line Source	20
1.5	Optically Induced Acoustic Waves	22
1.5.1	A Note on the Grüneisen Coefficient	24
1.5.2	Instrumentation	26
1.6	Goals	26
2	Broadband photoacoustic pulse propagation in tissue phantoms	31
2.1	Introduction	31
2.1.1	Acoustical Theory	33
2.2	Materials and Methods	41
2.2.1	Acoustic Transducer	43
2.2.2	Acoustic Attenuation	44
2.2.3	Acoustic Dispersion	44
2.2.4	Acoustic Diffraction	45
2.3	Results	48
2.3.1	Acoustic Attenuation	48
2.3.2	Acoustic Dispersion	49
2.3.3	Acoustic Diffraction	49
2.4	Discussion	49
2.4.1	Acoustic Attenuation	49
2.4.2	Acoustic Dispersion	51
2.4.3	Acoustic Diffraction	52
2.4.4	Justification of Direct Red Solutions as Tissue Phantoms	52
3	Depth profiling of absorbing soft materials using photoacoustic methods	55
3.1	Introduction	55
3.1.1	Acoustic Wave Theory	57
3.2	Materials and Methods	60
3.2.1	Photoacoustic Set Up	60
3.2.2	India Ink Solution	60
3.2.3	Acrylamide Gel	61
3.2.4	Elastin Biomaterial	61

3.2.5	Acoustic Transducer	62
3.2.6	Sound Speed Measurement in Acrylamide	62
3.2.7	Discrimination of Layered Acrylamide	63
3.2.8	Acoustic Wave Generation	63
3.2.9	Absorption Algorithm	63
3.3	Results	66
3.3.1	Transducer Calibration	66
3.3.2	Sound Speed in Acrylamide	66
3.3.3	Gel Layer Resolution	67
3.3.4	Computer Simulations	67
3.3.5	Gel Absorption Coefficient	68
3.3.6	Elastin Biomaterial	69
3.4	Discussion	69
3.4.1	Gel Layer Resolution	69
3.4.2	Computer Simulations	70
3.4.3	Gel Absorption Coefficient	71
3.4.4	Elastin Biomaterial	72
3.4.5	Applications	72
4	Localization of spherical photoacoustic sources in acrylamide gel phan-	
	toms using time domain measurements	74
4.1	Introduction	74
4.2	Materials and Methods	79
4.2.1	Apparatus	79
4.2.2	Acoustic Transducer	81
4.2.3	Acrylamide Gels	84
4.2.4	Optical Scattering Measurements	86
4.2.5	Acoustic Wave Simulation	87
4.2.6	Backprojection Algorithm	87
4.2.7	Sphere Size Calculations	88
4.3	Results	92
4.3.1	Transducer Calibration	92
4.3.2	Optical Scattering Measurements	93
4.3.3	Acoustic Waveform from Optically Thick Spheres	94
4.3.4	Sphere Size Determination	94
4.3.5	Localization of Spherical Sources	95
4.3.6	Localization of Paired Sources	105

4.4	Discussion	105
4.4.1	Optical Scattering Measurements	105
4.4.2	Acoustic Waveform from Optically Thick Spheres	108
4.4.3	Sphere Size Determination	108
4.4.4	Localization of Spherical Sources	109
4.4.5	Localization of Paired Sources	111
4.4.6	Conclusions	112

5 Design and testing of an endoscopic photoacoustic probe for determining treatment depth after photodynamic therapy of esophageal cancer . . . 114

5.1	Introduction	114
5.1.1	Photodynamic Therapy for Esophageal Cancer	115
5.1.2	Photoacoustic Propagation Time	115
5.2	Materials and Methods	117
5.2.1	Photoacoustic Set Up	117
5.2.2	Probe Construction	119
5.2.3	Amplification	121
5.2.4	Transducer Characteristics	121
5.2.5	Acoustic Testing	125
5.2.6	Sound Speed	125
5.2.7	Vein Model Test	126
5.2.8	<i>In Vivo</i> Testing	127
5.3	Results	127
5.3.1	Transducer Characteristics	127
5.3.2	Acoustic Testing	127
5.3.3	Sound Speed	128
5.3.4	Vein Model Test	128
5.3.5	<i>In Vivo</i> Testing	136
5.4	Discussion	136
5.4.1	Photoacoustic Propagation Time	136
5.4.2	Amplification	136
5.4.3	Acoustic Testing	138
5.4.4	Sound Speed	138
5.4.5	Vein Model	140
5.4.6	<i>In Vivo</i> Testing	140
5.4.7	Probe Design	140
5.5	Conclusions	142

6	General discussion and conclusions	143
6.1	Broadband Photoacoustic Pulse Propagation in Tissue	143
6.2	Depth profiling of absorbing soft materials using photoacoustic methods	145
6.3	Localization of spherical photoacoustic sources in acrylamide gel phantoms using time domain measurements	146
6.4	Design and testing of an endoscopic photoacoustic probe for determining treatment depth after photodynamic therapy of esophageal cancer	147
6.5	Conclusions	148
	Bibliography	150
	Biographical Note	159

List of Tables

2.1	Sound speed, densities, and acoustic impedances for various tissues and water, acrylamide gel, and mineral oil. All tissue impedances are within 10% of 1.5 g/cm ² -s, except bone, which has a value of 6.4 g/cm ² -s. Acrylamide gel is within 7% and water is within 2% of the value. Mineral oil has a much lower acoustic impedance, 1.15 g/cm ² -s, mostly primarily due to its low density. Its usefulness as a phantom comes from its immiscibility with water and its optical clarity.	53
4.1	The reduced scattering coefficients of the 1% Intralipid solutions were calculated by determining the effective attenuation of the solutions of known absorption coefficient. The errors for the effective attenuation coefficients are standard deviations, while the error for the reduced scattering was derived from error propagation.	93

List of Figures

1.1	An illustration of photoacoustic generation. The resultant acoustic field is composed of acoustic radiation from the embedded source and boundary interactions.	2
1.2	A shadowgraph of acoustic propagation created by a 600 μm optical fiber immersed in a 1000 cm^{-1} solution of Orange G in water. A 335 nm laser source deposited energy in the volume directly beneath the fiber face. A plane wave emerged from the area beneath the fiber (indicated by the dark area), while a boundary wave emanated from the circumferential ring about the fiber. The progression of the acoustic wave can be tracked from the top left photograph (70 ns) to the top right photograph (100 ns) to the bottom left photograph (150 ns) to the bottom right photograph (180 ns). These times correspond to a sound speed of 1.5 $\text{mm}/\mu\text{s}$	3
1.3	The pressure amplitude of a dipole source as a function of angle in the far field.	21
1.4	The measured acoustic wave as a function of time. The wave was induced by irradiating a plane surface of optically absorbing acrylamide gel, with $\mu_a = 180 \text{ cm}^{-1}$. Peak “A” denotes the surface of the gel, while “B” represents the tensile wave peak.	23
1.5	The acoustic wave from Figure 1.4 as a function of depth. The highest pressure is at the surface, where the optical energy was highest. The optical energy available for absorption ($\mu_a = 180 \text{ cm}^{-1}$) and subsequent conversion to acoustic energy falls exponentially according to Beer’s Law.	25
1.6	The depth profiling experimental set up relies on optically induced acoustic waves traveling through the acoustic medium and being detected by a piezoelectric transducer. The gels resting on the transducer may be homogeneous or layered, as shown here. Alternatively, a stained biomaterial could be substituted for the gel.	28
1.7	An embedded sphere in turbid acrylamide gel is irradiated with laser light, giving rise to an acoustic field. The acoustic field is sampled by a translating PVDF transducer.	29

2.1	A disk of irradiation is formed by incident laser irradiation. The disk dimensions are given by the laser spot diameter and the absorption depth. In a stress confined laser pulse, the disk may act as a piston head in the fluid, imparting a pressure wave into the fluid, followed by an inverted reflected wave of equal amplitude imparted by the free surface of the air/fluid interface.	32
2.2	Determining phase angle from the product of the wavenumber, k , and the radial displacement, r .	35
2.3	The acoustic field of a plane piston source can be derived by integrating a series of line sources that make up the disk. Here r is the distance from the origin to the observatin point, while r' is the distance from a point on the line source to the observation point.	36
2.4	The calculated beam pattern for a baffled piston is shown here. The main lobe is surrounded by secondary lobes, predicted by the nodes inherent in the Bessel function that describes the pattern.	38
2.5	A photoacoustic pulse from a 5 mm laser spot incident on a 200 cm^{-1} absorbing solution. The frequency content is a sum of all frequencies below some high frequency limit, which may be determined by the duration of the positive peak.	39
2.6	The frequency content of the pulse shown in figure 2.5. The frequency content extends to about 50 MHz, though at about 30 MHz the amplitude is 1% of the maximum amplitude, which occurs at about 3 or 4 MHz. This is close to the frequency maximum predicted by the $1/e$ duration of the original acoustic pulse, 50 ns, corresponding to a frequency of about 20 MHz.	40
2.7	A reconstructed pressure pulse, made by summing frequencies to 20 MHz. Figure 2.5 was used to determine the limit of a finite sum of sinusoids. The resulting broadband pulse is shown here.	41
2.8	The set up for the broadband acoustic pulse propagation experiments. A Q-switched Nd:YAG laser irradiated Direct Red solutions of various depths and absorption coefficients. A PVDF acoustic transducer detected the waveforms in a transmission geometry. The detected waveforms were sent to a digitizing oscilloscope.	42
2.9	The antenna function of the PVDF transducer is shown as a function of angle. The amplitude is an average of two sets of measurements, The curve fit is a $\cos^2 \theta$ curve.	43

2.10	The relationship between the generation of the plane wave and the boundary wave from a disk of irradiation is shown here. The plane wave results from the circular spot, while the boundary wave arises from the band encircling the spot, the thickness of which is equal to the absorption depth.	45
2.11	The set up for the diffraction experiment is shown here. The Q-switched laser discussed previously irradiated a 200 cm^{-1} solution. The beam diameter was determined by an iris diaphragm. The resulting acoustic waves were detected by an optical system using a HeNe laser and a fast photodiode.	46
2.12	The optical detection set up relied on the change in optical index of refraction caused by a pressure wave incident on a water droplet on a prism. A focused HeNe beam was reflected from the water/glass interface and the beam was detected by the photodiode.	47
2.13	The acoustic attenuation is shown as a function of propagation distance and absorption coefficient. The experimental data is shown as discrete points, while the attenuation function fit, derived from equation 2.16, is shown as the continuous lines.	48
2.14	The frequency content of the acoustic waves generated from irradiating the 200 cm^{-1} solutions. The frequency content shows some dispersion at frequencies higher than 30 MHz, though for propagation distances less than 3 cm, dispersion is negligible.	49
2.15	The acoustic diffraction is shown as a small boundary wave slowly merging with the larger plane wave. The predicted boundary wave position is indicated by a black arrow on each waveform. The boundary wave is shown approaching the plane wave as the spot diameter, indicated by the number in the upper right corner, is varied. The boundary wave has fully merged with the plane wave with a 1.4 mm spot.	50
2.16	The attenuation predicted by equation 2.16. The far field shows attenuation of nearly constant slope, similar to the attenuation shown in the experiments. Equation 2.16 is not accurate for the near field.	51
3.1	(top) An acoustic wave generated by irradiating a 160 cm^{-1} acrylamide gel. The negative wave (B) following the positive wave (A) is a reflected tensile wave resulting from the acoustic mismatch of the acrylamide/air boundary. (bottom) The tensile wave was delayed by placing a clear acrylamide sheet before the absorbing acrylamide.	58
3.2	The absorption information of the acoustic wave is shown here as pressure and temperature as a function of depth for a 180 cm^{-1} gel.	59

3.3	The set up for the acoustic wave generation in the absorbing sample. . . .	60
3.4	The absorbing layer discrimination experimental arrangement. The two absorbing gel layers were separated by a clear, non-absorbing layer. . . .	64
3.5	The measured absorption coefficient of the India ink solutions for the spectrophotometer and the acoustic wave exponential curve fit. The linear nature of the curve indicates agreement between the two measurement methods.	67
3.6	Acoustic wave generated in two absorbing gel layers (140 cm^{-1} separated by $70\text{ }\mu\text{m}$ of clear gel. The clear layer is represented by the region of near zero pressure.	67
3.7	The result of running the absorption algorithm on the simulated acoustic waves with the 5% noise level.	68
3.8	The result of running the absorption algorithm on the acoustic waves generated in the various acrylamide gels with the indicated absorption coefficients.	68
3.9	The absorption coefficient of the layered acrylamide gel of figure 3.8. . . .	69
3.10	The acoustic wave generated in the ink stained elastin biomaterial.	69
3.11	The absorption coefficient of the ink stained elastin biomaterial as a function of depth. The ink concentration is highest at the surface and drops with depth.	70
4.1	The absorption of optical radiation in an optically thick sphere occurs in the spherical cap closest to the direction of the laser pulse.	75
4.2	The volume of absorption of an optically thick sphere from a laser pulse is shown here as a red hemispherical cap. The radius of the cap is a , the same as the sphere itself, while the wall thickness of the cap is the absorption depth, δ	76
4.3	The acoustic field from a hemispherical source can be computed by treating the source as a collection of disk sources. Computing new radial distance, r' , angle, θ' , and disk radius, a' , allows the computation of the field due to the additional disks. Δz is the distance from the origin to the new disk face, measured along the horizontal axis.	77

4.4	The spherical cap source is modeled here by creating a hemisphere from 10 successively smaller disks and then subtracting a smaller hemisphere from its core, made by a series of ten smaller disks. The beam pattern is similar to a plane piston source, without any weak deviations on or near the axis, as might have been supposed by the subtraction of the smaller hemisphere. Diffraction lobes are still evident on the beam pattern, as in the piston, though they disappear when the harmonic source is summed over a band of frequencies to create a pulsed source.	78
4.5	The photoacoustic experimental set up. The 532 nm laser pulse was coupled into a 1000 μm fiber. The fiber face was imaged onto the target. A PVDF transducer was used to detect the resultant acoustic waves. The waveform was then sent to a digital oscilloscope.	80
4.6	The acoustic transducer was a PVDF film detector in a brass housing. A BNC was connected to the PVDF electrodes for coupling to the oscilloscope. The $1.8 \times 1.8 \text{ mm}^2$ active area is shown as the crossed region on the top of the transducer.	82
4.7	Three acrylamide spheres are shown here. The sizes are 3 mm, 2 mm, and 1 mm as shown from left to right.	85
4.8	This is a density plot of the location of an absorbing acrylamide sphere in a turbid acrylamide block. The bright spot at the intersection of the backprojection arcs indicates the predicted position of the photoacoustic source. The vertical axis shows the distance above the initial transducer location (5 mm), while the horizontal axis shows the lateral offset of the sphere from the transducer (0.5 mm). The true position was 5 mm above and 0 mm offset.	89
4.9	The acoustic wave generation for the optically thick sphere is shown here. The region marked "1" is the pole, having the longest propagation time to the acoustic detector, while the region marked "2" is the equator, having the shortest propagation time.	90
4.10	The acoustic wave from a 2 mm diameter, 60 cm^{-1} sphere in clear mineral oil. The region marked "1" comes from the pole, as in figure 4.9. Likewise, the region marked "2" comes from the equator.	91
4.11	This is the calibration curve for the large area PVDF transducer. The sensitivity was done for 26, 54, 102, and 151 cm^{-1} Direct Red 81 solutions. The calibration was approximately $12.6 \pm 0.8 \text{ mV/bar}$	92

4.12	This is the calibration curve for the small area PVDF transducer. The sensitivity was done for 25, 48, 101, and 200 cm ⁻¹ Direct Red 81 solutions. The calibration was approximately 11.6 ± 0.4 mV/bar.	93
4.13	This is the waveform from irradiating an optically thick sphere (60 cm ⁻¹) with a 2 mm diameter 15 mm directly above the PVDF transducer. The sphere was immersed in clear mineral oil.	94
4.14	A simulation of a 60 cm ⁻¹ , 2 mm sphere irradiated by a stress confined laser pulse. The sphere was centered 15 mm above the detector.	95
4.15	The experimentally derived diameters, from equation 4.14 are graphed on the vertical axis, while the measurements on the horizontal axis are from the digital micrometer.	96
4.16	The experimentally derived diameters, from equation 4.14 are graphed on the vertical axis, while the measurements on the horizontal axis are from the digital micrometer.	97
4.17	The experimentally derived diameters, from equation 4.14 are graphed on the vertical axis, while the measurements on the horizontal axis are from the digital micrometer.	98
4.18	The experimentally derived diameters, from equation 4.14 are graphed on the vertical axis, while the measurements on the horizontal axis are from the digital micrometer.	99
4.19	The acoustic wave simulation of a 2 mm diameter, 60 cm ⁻¹ sphere directly above a detector.	100
4.20	The acoustic wave simulation of a 2 mm diameter, 60 cm ⁻¹ sphere translated 6 mm laterally from above a detector.	101
4.21	The localization map of the simulated acoustic waves. The source is shown by a sharp peak exactly on the simulate source location, directly above the detector at 18.5 mm.	102
4.22	The two waveforms used for the localization algorithm are shown here. The first waveform (top) was from the initial detector position. The second waveform (bottom) was from the detector translated 6 mm laterally. The first peak on both waveforms was from the actual sphere. The second peak on both waveforms was from the acoustic reflection from the acrylamide surface.	103
4.23	This is a 3-D graphic indicating the position of the spherical source as predicted by the localization algorithm.	104

4.24	The acoustic waves from the irradiated pairs in turbid acrylamide. The spheres were 2 mm in diameter and space 3.5 mm center to center. They had an absorption coefficient of 60 cm^{-1} . The top waveform is from irradiating the spheres with the detector directly below. The lower waveform is after laterally translating the detector 4 mm.	106
4.25	The localization map for the paired source is shown here. Though there is some noise, the two bright spots indicate the paired sources in their actual locations.	107
4.26	This is the velocity potential of the simulated acoustic wave from a 60 cm^{-1} spherical source, 18.5 mm above an acoustic detector. The function has only positive values, as it is the integral of a bipolar pulse with equal energy in the pressure and tensile components. The velocity potential is everywhere zero except where the pressure wave is nonzero.	110
5.1	Photographs of the pre- and post-treatment esophagous. In the left photograph, the tumor area is shown as bulbous obstructions in the esophageal lumen. In the photograph on the right, the region of necrotic tissue is shown as a white, blanched area. The thickness of this blanched area indicates the depth of necrosis and hence, the depth of PDT treatment.	116
5.2	An artist's rendering of the use of the endoscopic photoacoustic probe. The probe emerges from the endoscope and is directed to treated (blanched) areas to determine the depth of necrosis.	117
5.3	The Q-switched laser launched 532 nm, 5 ns pulses into a $600 \mu\text{m}$ fiber. A piezoelectric detector was positioned at the end of the optical fiber. Optically absorbing targets were irradiated by the fiber and the resulting acoustic waves were detected by the piezoelectric element. The signal was sent to the oscilloscope.	118
5.4	The photoacoustic probe is shown here. The 45° polished fiber face directed the laser light in a side firing mode (upwards, out of the plane of the page). The glass tube contained the fiber face and ensured a glass/air interface for proper reflection onto the target. The acoustic detector was positioned alongside the fiber. The detector was composed of a piezoelectric film on a miniature coaxial cable that sent the signal to the oscilloscope.	120
5.5	The acoustic detector was composed of an aluminized PVDF film in contact with the center conductor of a miniature coaxial cable ($860 \mu\text{m}$ diameter), with the other side electrically connected to the conducting shield of the coaxial cable with conducting epoxy.	121

5.6	The photoacoustic probe is shown here. The total width of the fiber–detector pair is 2.1 mm. The glass tube is rounded at the tip to prevent damage to tissue.	122
5.7	The circuit schematic for the operational amplifier is shown here. The operational amplifier was a CLC425 ultra low noise, wideband operational amplifier. The resistor pair, R1 and R2, theoretically provided a gain of 45, though actual resistance values provided a gain of 40.	123
5.8	The set up for determining the directivity of the detector is shown here. A 600 μm optical fiber irradiated an absorbing solution under clear water. The acoustic detector was positioned above the irradiation site and rotated to determine the detector response as a function of angle.	124
5.9	The acoustic testing of the photoacoustic probe was performed by irradiating solutions of various absorption coefficients under clear or turbid solutions of various thicknesses. The resulting acoustic waves were detected by the photoacoustic probe and sent to an oscilloscope.	126
5.10	The sensitivity of the acoustic transducer is shown here as detector response to plane acoustic wave as a function of angle.	128
5.11	The acoustic waves resulting from irradiating a Direct Red solution ($\mu_a = 60 \text{ cm}^{-1}$) with various thicknesses (1–8 mm) of clear water between the absorbing solution and the detector. The signal, easily discernable from the noise level, was delayed as the clear layers become thicker. Zero on the horizontal axis indicates the laser pulse trigger.	129
5.12	The acoustic waves resulting from irradiating a Direct Red solution ($\mu_a = 60 \text{ cm}^{-1}$) with various thicknesses (1–8 mm) of turbid solution ($\mu_s \neq 15 \text{ cm}^{-1}$) between the absorbing solution and the detector. The signal, easily discernable from the noise level, was delayed as the turbid layers become thicker.	130
5.13	The signal to noise ratios for the solutions of various absorption coefficient are shown as a function of depth of clear layer. The maximum signal occurred at 3–4 mm of depth, due to the offset of the acoustic detector from the optical fiber. This offset caused the acoustic wave source to be not directly underneath the detector, decreasing the detector sensitivity. The acoustic signal maximized at about 3–4 mm away, as the resultant larger spot created acoustic waves directly beneath the detector. For greater than 4 mm, the lower radiant exposure dominated the the acoustic signal generation, resulting in a weaker acoustic detection.	131

5.14	The signal to noise ratios for the solutions of various absorption coefficient are shown as a function of depth of turbid layer. The maximum signal occurred at 1 mm, as the highest radiant exposure occurred and optical diffusion was stronger at greater distances, decreasing the acoustic signal strength.	132
5.15	The calculated sound speeds through clear and turbid layers are shown here. All are within 4% of 1.5 mm/ μ s.	133
5.16	This is the acoustic wave on the 7 th of 15 scans on the vein model. The vein model was directly underneath the detector on this scan. The initial peak indicates the detected vein model and the propagation time, though several following peaks occur.	134
5.17	A localization map of the vein model was constructed using all 15 scans. The result is a map showing the vein model in depth and scan position. The small circle, superimposed onto the first region of acoustic energy, indicates the vein model position.	135
5.18	The top graph shows the acoustic waves from the normally perfused and underperfused finger tip. The acoustic signal from the normally perfused fingertip (red) is greater in amplitude than the underperfused fingertip (blue), and the peak of the underperfused fingertip appears to be delayed by about 100 ns, corresponding to 150 μ m (lower graph). The peak times are indicated by the vertical bars. The amount of ringing and noise from the transducer prevent precise analysis of layered structures, though the discrimination of the two perfusion levels is evident by a factor of four difference in acoustic amplitude. A 3 mm water layer separated the fingertip from the acoustic detector, accounting for the 2 μ s delay in the signals. . . .	137
5.19	For the clear intervening layer, the acoustic signal for distances of 1-2 mm is weaker than signals detected at 3-5 mm, as the acoustic sensor is not directly over the acoustic source when the probe is so close. This is due to the antenna function of the probe and the small spot size. After about 5 mm, the decreased radiant exposure results in a weaker acoustic wave, making the detected signal weaker.	139
5.20	Earlier versions of the photoacoustic probe were made from acrylic cylinders housing a side firing optical fiber and a PVDF film between two electrodes. The acrylic cylinder wasn't optically clear enough after machining. At such small dimensions, the acrylic was weak and unsuitable for a robust photoacoustic probe.	141

6.1 A scheme for combining optical and acoustic diagnostic methods. A delivery fiber is used to introduce a stress confined heating in tissue with a fast laser pulse, while simultaneously delivering white light. A collection fiber detects reflectance from the white light for optical property determination. The acoustic transducer detects the resultant acoustic wave from the fast laser pulse. 149

Abstract

Characterization of photoacoustic sources in tissue using time domain measurements

John Andrew Viator, Ph.D.

Oregon Graduate Institute of Science & Technology, 2000

Supervising Professor: Scott A. Prahl

Photoacoustic phenomenon in tissue and tissue phantoms is investigated with the particular goal of discrimination of diseased and healthy tissue.

Propagation of broadband photoacoustic sources in tissue phantoms is studied with emphasis on attenuation, dispersion, and diffraction. Attenuation of photoacoustic waves induced by a circular laser spot on an absorber/air interface is modeled by the on-axis approximation of the acoustic field of a baffled piston source. Dispersion is studied in a diffraction free situation, where the disk of irradiation was created by a 5 mm laser spot on a 200 cm^{-1} solution. The genesis of diffraction in an absorbing solution was displayed by showing the merging of a boundary wave with a plane wave from a circular laser spot on an absorbing solution.

Depth profiling of absorbing tissue phantoms and stained tissue was shown using a photoacoustic method. Acrylamide gels with layers of different optical absorption and stained elastin biomaterials were irradiated with stress confined laser pulses. The resulting acoustic waves were detected with a lithium niobate wideband acoustic transducer and processed in an algorithm to determine absorption coefficient as a function of depth.

Spherical photoacoustic sources were generated in optically clear and turbid tissue phantoms. Propagation time and acoustic pulse duration were used to determine location and size, respectively. The photoacoustic sources were imaged using a multiplicative backprojection scheme. Image sources from acoustic boundaries were detected and dipole sources were detected and imaged.

Finally, an endoscopic photoacoustic probe was designed, built, and tested for use in determining treatment depth after palliative photodynamic therapy of esophageal cancer. The probe was less than 2.5 mm in diameter and consisted of a side firing 600 μm optical fiber to deliver laser energy and a 890 μm diameter, side viewing piezoelectric detector. The sensitivity of the probe was determined. The probe was also tested on coagulated and non-coagulated liver, *ex vivo* and on normally perfused and underperfused human skin, *in vivo*.

Chapter 1

Introduction

The use of lasers as a diagnostic tool in biomedical engineering and research has grown considerably in the last decade. While most applications exploit the optical nature of the light-tissue interaction, the field of *photoacoustics* uses optical energy to generate an acoustic wave which propagates in the tissue environment. The acoustic wave propagation is fundamentally related to various tissue properties and an analysis of the wave dynamics can provide insights into these properties. This dissertation presents background on photoacoustic propagation and shows results of several photoacoustic methods to derive information about tissue and tissue phantoms. This information is analyzed with the ultimate goal of discriminating healthy and diseased tissue.

Photoacoustic effects have been known since the 19th century [1,2] with the discovery by Bell *et al.* of the effect of sunlight on a selenium cell and rapidly modulated sunlight on gases. A renaissance in photoacoustics began with the advent of lasers in the 1960's [3,4], when researchers were able to exploit the short laser pulses for acoustic generation. The photoacoustic phenomena described in this dissertation were all produced by a photothermal interaction, resulting from a deposition of optical energy onto an absorbing target in a stress confined manner *i.e.*, where the optical pulse duration is shorter than the time required for the deposited energy to propagate away acoustically. In this dissertation, the targets were tissue phantoms and tissue, where the assumption that sound speed and density, and hence acoustic impedance, is essentially equal to that of water.

Figure 1.1 shows a pictorial representation of photoacoustic generation from an embedded optical absorber in layered tissue. The tissue constitutes a planar surface in air.

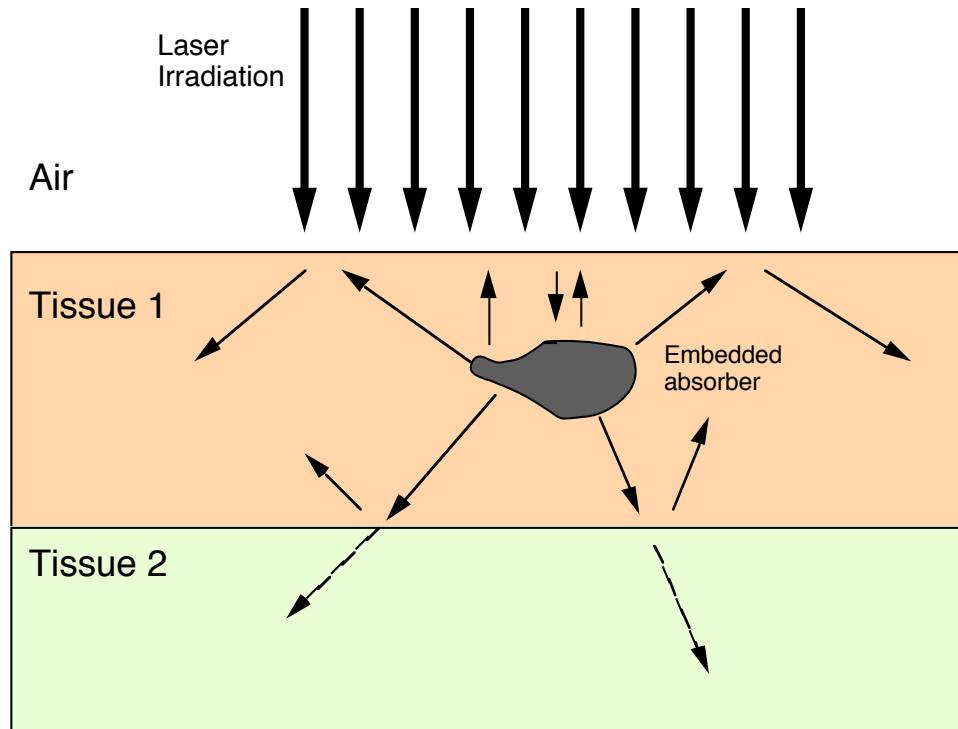


Figure 1.1: An illustration of photoacoustic generation. The resultant acoustic field is composed of acoustic radiation from the embedded source and boundary interactions.

The laser irradiation is scattered in the optically scattering tissue medium, then is absorbed by the embedded source. The resultant acoustic field is composed of radiation from the source and boundary reflections and transmissions. Here, the air/tissue interface constitutes a free surface, in which the acoustic radiation is entirely reflected back into the tissue. The tissue 1/tissue 2 interface causes transmissions and reflections as determined by the acoustic impedance mismatch and Snell's Law.

Figure 1 illustrates the generation of an acoustic wave and its effect on the index of refraction of a solution of Orange G in water, by Paltauf *et al.*. A $600\ \mu\text{m}$ fiber was immersed in the solution. An Nd:YAG laser in the third harmonic at $355\ \text{nm}$ was used to pump an optical parametric oscillator for an output wavelength of about $490\ \text{nm}$, which was the absorption peak of the Orange G at about $1000\ \text{cm}^{-1}$. The pulse duration was about $6\ \text{ns}$. A time gated camera was used to acquire the photos, with a $10\ \text{ns}$ exposure time. The acoustic wave was generated within an absorption depth of the fiber face

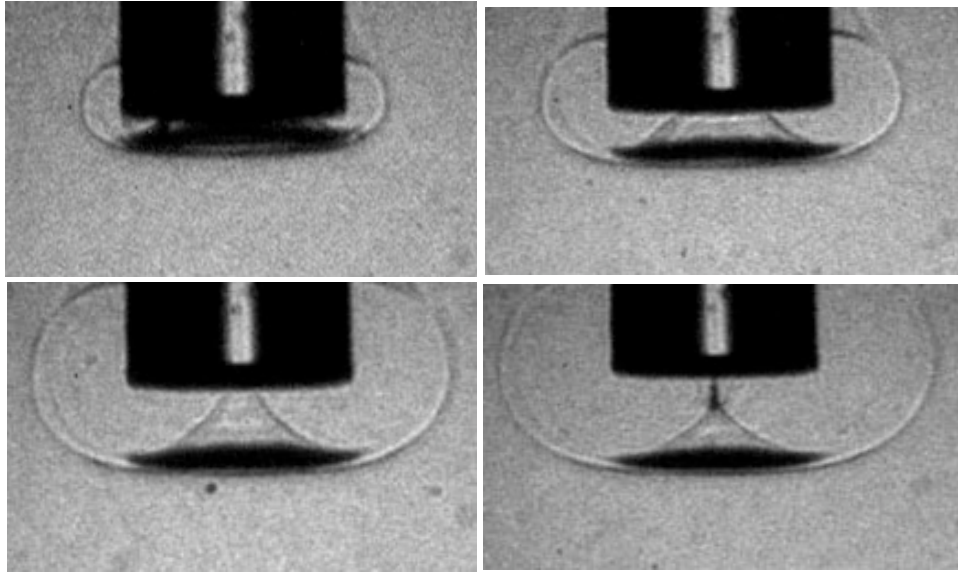


Figure 1.2: A shadowgraph of acoustic propagation created by a $600\ \mu\text{m}$ optical fiber immersed in a $1000\ \text{cm}^{-1}$ solution of Orange G in water. A $335\ \text{nm}$ laser source deposited energy in the volume directly beneath the fiber face. A plane wave emerged from the area beneath the fiber (indicated by the dark area), while a boundary wave emanated from the circumferential ring about the fiber. The progression of the acoustic wave can be tracked from the top left photograph ($70\ \text{ns}$) to the top right photograph ($100\ \text{ns}$) to the bottom left photograph ($150\ \text{ns}$) to the bottom right photograph ($180\ \text{ns}$). These times correspond to a sound speed of $1.5\ \text{mm}/\mu\text{s}$.

($10\ \mu\text{m}$). The progression of the acoustic wave is shown by the top left photo, at about $70\ \text{ns}$ after the laser pulse, followed by the top right photo, at about $100\ \text{ns}$ after the laser pulse. The bottom left photo was taken at about $150\ \text{ns}$ after the pulse, while the last photo was taken at about $180\ \text{ns}$ after the pulse. These times correspond to a sound speed of about $1.5\ \text{mm}/\mu\text{s}$. A plane wave is shown by the dark area directly below the fiber face. The acoustic velocity was monitored by the plane wave progression. The expanding ring in the photographs are acoustic boundary waves emanating from the circumferential ring of the optical absorption volume, which was equal to the product of the area of the fiber face (plane wave) and the absorption depth of the laser deposition.

In the biomedical field, the advantage of photoacoustic over purely optical diagnostic methods is primarily one of signal propagation distance and hence, the size and depth

of the region under investigation. In the regime of biological media, light propagation is dominated by scattering. The difficulty of modeling light scattering in complicated media limits the utility of optical diagnostics. A scattering coefficient in human tissue may be about 200 cm^{-1} , giving a mean free path due to scattering of a few tens of microns. For example, human skin has a scattering coefficient of about 200 cm^{-1} in the red wavelengths, while human aortic tissue has a scattering coefficient of about 300 cm^{-1} [5]. Light propagation distances greater than a few millimeters result in loss of coherence and polarization and hence, the imaging ability. Acoustic wave propagation is not affected by optically turbid media in this way. The effect on the acoustic wave by the turbid media is only in its generation, which is dependent on the optical absorption. Acoustic propagation in tissue can be characterized by interface reflections and viscoelastic attenuation. In this dissertation the acoustic field is modeled using the linear acoustic wave equation in the form of spherical, cylindrical, or plane waves.

Chapter 2 presents theoretical and experimental results of broadband photoacoustic propagation in a tissue phantom. Spherical and piston acoustic sources are modeled and adapted to describe photoacoustic propagation. Acoustic parameters, including attenuation, dispersion, and diffraction are investigated for planar piston sources. Chapter 3 presents a method of depth profiling in a planar tissue geometry. The photoacoustic depth profiling uses plane wave analysis to determine the absorption coefficient as a function of depth in absorbing gels and a stained biomaterial. Chapter 4 uses time domain methods to localize an optically thin spherical acoustic source in turbid acrylamide gels and tissue. The physical size and absorption coefficient of the sphere is varied. The spheres are embedded in clear and turbid acrylamide tissue phantoms, with acoustic propagation depths of up to 20 mm. A dipole photoacoustic source was detected, achieving discrimination of the two spherical sources with a minimum center to center separation distance of 2 mm for two spheres with 2 mm diameters. A computational backprojection method was used to localize the acoustic source. Chapter 5 demonstrates the design, construction, and testing of a photoacoustic probe for endoscopic use for measuring treatment depth after photodynamic therapy (PDT) of esophageal cancer. The post-treatment site is characterized by a layer of turbid, unperfused necrotic layer over a healthy, perfused layer of esophagus.

The photoacoustic probe delivered stress confined laser light via a 600 μm fiber to induce acoustic waves in the underlying perfused layer of esophagus, while a piezoelectric detector was used to determine the acoustic propagation time, which corresponded to the necrotic layer thickness. The probe was tested on clear and turbid phantoms, and on human tissue *in vivo*, with various levels of perfusion.

1.1 Photoacoustic History

After the 19th century investigations by Bell and others, mentioned above, photoacoustic research remained essentially dormant until the 1930's, with trace gas analysis by Viengerov, Pfund, Luft, and others [6]. These early studies were conducted with CW light sources, unlike modern PAS and photoacoustics in general, where photoacoustic signals are typically generated with lasers with nanosecond pulse durations. They used visible and infrared optical sources and microphones to detect gaseous components in samples. These studies were the precursors to modern photoacoustic spectroscopy (PAS), in which an acoustic signal is generated in a photoacoustic cell by a modulated laser source and detected with a microphone. The mechanism of acoustic generation is due to heating by the sample molecules. The modulation is then related to the gas concentration by the modulation of heating in the sample. Sigrist [7] reviewed the state of PAS, demonstrating that absorption coefficients as low as 10^{-8} cm^{-1} could be detected in gaseous samples. More recently, Arnott *et al.* [8] proposed a thermoacoustic enhancement to PAS by increasing the Q factor (the acoustic resonator quality factor) to increase the signal to noise ratio (SNR) in PAS of gases. They showed that an induced thermal gradient in the photoacoustic cell would increase the Q factor in the PAS studies and that a higher Q would increase the SNR. Hand *et al.* [9], in an effort to overcome difficulties with typical microphone detectors, including impedance mismatching with samples, developed a Michaelson-based, optical fiber interferometer for PAS in methanol and water. Beard *et al.* [10] used PAS with a PVDF (polyvinylidene fluoride) membrane hydrophone and a frequency-doubled Nd:YAG laser with a gas filled Raman cell to distinguish normal and atheromatous *post mortem* arterial tissue. They found that at 461 nm, there was a reproducible difference

in the photoacoustic signal of normal and atheromatous tissue. At 532 nm, they found structure and thickness information from the photoacoustic signal.

1.1.1 Photoacoustic Generation of Simple Sources

Diebold *et al.* [11–13] developed a theory of photoacoustic generation in simple sources using a frequency domain method, in which the amplitude and phase of the pressure signals were described using the modulation frequency. The time domain solution was given by its Fourier transform. Boundary discontinuities gave rise to reflection and dispersion. They developed a theory for a spherical droplet in a fluid of dissimilar acoustic properties and for particulate matter. Furthermore, they extended the theory to monopole radiation in one, two, and three dimensions, with experimental results on a fluid layer of methanol, cylinders and spheres of benzaldehyde. They used a frequency-doubled Q-switched, Nd-doped, Nd:YAlG laser. The detection was made with a PVDF film transducer. Khan *et al.* [14, 15] extended the study to optically thin cylinders and spheres, using the same frequency domain approach. Experimental results using immiscible fluids to form cylinders and spheres matched the theory presented previously. They employed an Nd:YAG laser at 532 nm with a pulse duration of about 10 ns.

1.1.2 Cavitation and Photoacoustics

Research and application of photoacoustics in the biomedical field include cavitation and ablation acoustics. Early biomedical studies of photoacoustics, apart from PAS, had to do with damage due to acoustic effects induced by pulsed laser sources. Anderson *et al.* [16] attempted to model tissue damage by thermal effects, including laser induced shock waves. Lauterborn *et al.* [17] reviewed cavitation dynamics as a source of ultrasonic waves by using high speed photography from laser induced bubbles. Vogel *et al.* also studied cavitation dynamics as a source of acoustic waves, with applications including laser lipotripsy and ocular surgery [18, 19]. They used a Q-switched Nd:YAG laser to irradiate bovine corneas *in vitro* and found damage due to acoustic events with a damage range proportional to the cube root of the laser pulse energy. Additionally, Jansen *et al.* [20, 21] studied mechanical damage due to laser irradiation. They used free-running and Q-switched Ho:YAG lasers

to study bubble formation and acoustic energy in tissue phantoms and in ablation of human aortas *in vitro*. They found the acoustic damage most pronounced in the aorta with the Q-switched laser, with a pulse duration of 200 ns, versus the free-running laser with a pulse duration of 250 μ s. In the tissue phantoms, they varied the pulse duration from 500 ns for the Q-switched laser and from 100–1100 μ s for the free-running laser. The result was that increase pulse duration changed the bubble shape from spherical to an elongated bubble. In fact, the only measurable thermoelastic wave came from the Q-switched laser, as the longer pulses did not achieve stress confinement. Topaz *et al.* used a mid-infrared laser at 2.1 μ m with a pulse duration of 250 ms and 500 mJ/pulse to disrupt fibrin clots with photoacoustic energy. Shangguan *et al.* used the photomechanical effect for drug delivery, rather than studying it as a damage mechanism [22, 23]. They found that they could deliver colored oil into gelatin phantoms with a 1 μ s pulsed dye laser, with distribution of a few millimeters. They studied and proposed the photoacoustic drug delivery of fibrinolytic drug to aid in breaking up clots during laser thrombolysis.

1.1.3 Photoacoustic Diagnostics and Imaging

In the 1990's, many researchers have been investigating the use of photoacoustics as a medical diagnostic method, including optical property measurement and detection of embedded optical absorbers in tissue. Oraevsky *et al.* used wideband piezoelectric detectors made from lithium niobate to detect acoustic waves in tissue and tissue phantoms induced by stress confined laser pulses. Analysis of the acoustic wave shape gave information about the optical properties in the media, including absorption and scattering coefficients [24–26]. Paltauf *et al.* used a optical method for detecting acoustic waves, which exploited the change in density of water during pressure pulse propagation to modulate the reflectance of a HeNe beam on a water glass interface [27–30]. They extended this technique to two dimensional imaging with a CCD camera and also made three dimensional maps using slices of the two dimensional images. Jacques *et al.* [31, 32] and Beard *et al.* [33–36] also detected acoustic waves with optical means, though they used interferometric methods. Jacques used a dual beam, common path Michaelson interferometer to sense perturbations on the surface of tissue phantoms due to the embedded

photoacoustic sources. Beard used a optical fiber, low finesse Fabry–Perot interferometer to detect acoustic waves.

1.2 Motivation: Medical Imaging

Imaging of tissue for detection of pathology is an important part of the diagnosis of disease. Choosing the most appropriate imaging method is an important step in diagnosing illness. Considerations include ensuring the greatest efficacy in detection of the pathology, reducing the financial costs, ensuring the least amount of patient discomfort, and reducing the possibility of an imaging technique to interfere with further testing or treatment.

Currently, the field of biomedical imaging is dominated by radiographic methods, which utilizes ionizing radiation as the probing means. Other methods include magnetic resonance imaging (MRI), nuclear medicine imaging, and ultrasound [37, 38]. While these modalities are successful, mature technologies, there exist short comings in each area. Some of these short comings may be appropriately addressed by photoacoustic imaging, particularly in applications that target specific regions on the centimeter scale, while requiring spatial resolution on the order of tens of microns.

1.2.1 X-Ray Techniques

X-ray techniques include conventional radiography, in which shadowgrams from x-ray transmission through a patient are produced, mammography, in which tumors in breast tissue are detected, angiography, in which x-ray images are obtained aided with radiopaque contrast agents, and computed tomography (CT), where x-ray transmissions scans are combined to form images of gross anatomical structures [39]. While these techniques are used widely, the ever present drawback exists with the use of ionizing radiation. The greatest hazard is harming the patient with large doses of radiation which may incite the genesis of cancer at the radiation site. Additionally, expensive, high voltage sources are needed to produce x-rays. Attempts to reduce the x-ray intensity are hampered by low signal to noise ratio as the quantum noise becomes more significant.

Computed Tomography

CT was developed in the 1970's and constituted a revolution in modern radiography [40]. X-ray scans were performed on a patient, creating projections through tissue. The projections were treated by computational methods based on the Radon Transform to produce images [40, 41]. The projections are measured for attenuation and compared to the expected attenuation through water [37, 42]. The projection is assigned a value on the Hounsfield scale, in which water is assigned a value of 0. The scale is 2000 Hounsfield Units (HU) wide. Final spatial resolution is limited by computer resources and radiation dose. Typical resolutions are on the order of millimeters. The set up for CT is expensive, since it requires an x-ray source, scanning machinery, and computer equipment.

Mammography

Mammography is a technique that uses x-rays to detect cancerous tumors in breast tissue. Its principle is based on attenuation of x-rays, similar to conventional radiography [40]. Though it potentially has the ability to detect cancerous lesions well before the palpation threshold, questions remain regarding the genesis of cancerous tissue due to the application of ionizing radiation. Unfortunately, the detection threshold for tumors is about a centimeter in size [37].

1.2.2 Ultrasound

The field of ultrasound has achieved success in imaging, particularly in pre-natal diagnosis and large organ imaging, though the resolution is limited by the low acoustic frequencies (usually 1–10 MHz, though often < 5 MHz) [37, 42–44]. Ultrasonic imaging uses the principle of pulse-echo sonography, where acoustic reflections and scattering from an acoustic transducer are detected and analyzed to determine tissue interfaces. Signal strength, $S(t)$, is determined and modeled as a time domain convolution of the transmitted signal, $T(t)$, transducer properties, $B(t)$, signal attenuation, $A(t)$, and scattering properties, $\eta(t)$ [45]. This is described by the equation,

$$S(t) = A(t) \otimes B(t) \otimes A(t) \otimes \eta(t) \quad (1.1)$$

where \otimes is time domain convolution. Computational burden is usually reduced by converting the convolution above to multiplication of the quantities in the frequency domain.

Ultrasound has achieved popularity in the medical imaging field due to its efficacy, low cost, and use of non-ionizing radiation. Ultrasound units are portable, unlike x-ray and MRI machines. Though ultrasound energy can permanently damage tissue, the level of power used for diagnostics is several orders of magnitude lower than the damage threshold [43].

1.2.3 Photoacoustic Imaging

Of all the current imaging modalities in clinical use, photoacoustic imaging is most closely related to ultrasound. In fact, photoacoustic imaging can be described loosely as an optically induced ultrasound. Its use, however, is significantly different, due to the optical generation of the acoustic waves. First, optical properties of the targeted tissue can be derived from a proper study of the acoustic waves. Second, the acoustic waves generated are broadband and generally have a higher frequency content than traditional ultrasound. Additionally, the acoustic source in traditional ultrasound is an externally positioned transducer. Imaging with ultrasound depends on differentiating tissue by acoustic contrast. Photoacoustic imaging, on the other hand, creates acoustic sources within the tissue, thus enhancing the discrimination of the targeted tissue and surrounded media. In photoacoustics, the acoustic pulse has frequencies as high as 100 MHz. While the high frequencies increase the resolution to the micron scale, acoustic attenuation is aggravated. This causes the propagation distance to be limited to several centimeters. While this is not adequate for imaging large organs or fetuses, the resolution is ideal for detection of tumors and discrimination of tumor margins. Additionally, the acoustic waves are suited for depth profiling of absorbing layers. The first study in this dissertation is directed at such depth profiling, while the time domain methods are directed toward tumor detection and characterization.

Like ultrasound, photoacoustic imaging enjoys the benefit over x-ray methods in that the creation of the acoustic waves involves non-ionizing radiation. Subablative laser pulses are directed at target tissue and at most raise the tissue temperature by only a few degrees.

1.2.4 Breast Cancer Diagnosis

Breast cancer is the leading cause of death of middle aged women; One in eleven women will develop it [44]. Early detection and treatment of cancerous breast lesions significantly improve survivability. While mammograms currently offer the most effective early detection modality, photoacoustic detection of calcified or hypervascular breast masses may prove an attractive alternative or adjunct to mammography.

The anatomy of the female breast consists mainly of fatty and glandular tissue [44,46], which gives rise to minimal acoustic reflections at the interface of these two tissue types, due to good acoustic impedance matching. Because of the matched impedances, the breast can be considered a fairly homogeneous acoustic medium. If a tumor mass in breast tissue selectively absorbs laser light, then this mass will become photoacoustic sources. Detection of laser induced acoustic waves in cancerous breast tissue may be modeled by acoustic propagation in a homogeneous medium. It is an aim in this dissertation to show that such photoacoustic methods can be used to detect and localize small optical absorbers in an acoustically homogenous medium, as an attempt to model the detection of cancerous lesions in breast tissue.

1.3 The Current State and Future of Photoacoustic Methods in Biomedicine

The field of photoacoustics in biomedical optics is rapidly expanding, with research being conducted in glucose and hemoglobin monitoring, optical property measurements, tomography and imaging, photoacoustic spectroscopy, and photomechanical drug delivery. The availability of lasers suitable for inducing acoustic waves in tissue and the need for new diagnostic methods has made photoacoustics a field rich in innovation in the use of laser induced acoustic waves.

1.3.1 Tomography and Imaging

In the area of tomography and imaging, Andreev *et al.* [47] used an arc-array of PVDF transducers and radial backprojection of human breast tissue phantoms. Gelatin

spheres of 1 cm^{-1} at 1064 with 8 mm diameter were detected up to 34 mm in depth in gelatin phantoms using the array, with a total processing time of 32 seconds. Kruger *et al.* [48] used a thermoacoustic computed tomographic system to detect spherical absorbers in tissue phantoms and have performed *in vivo* measurement of human female breasts. Thermoacoustic waves were induced using 434 MHz radio waves. A transducer array in a hemispherical bowl was used to detect the resulting acoustic waves. Imaging was enhanced by determining the impulse response of the imaging system and processing the electronic artifacts. One image showed a tumorous cancer mass of a few centimeters in diameter in a patient prior to chemotherapy. A followup image after therapy showed the same mass reduced in size. Though this particular mass was large, the resolution achievable by this system was claimed to be 1–2 mm.

Paltauf *et al.* [30], used an imaging camera and a HeNe photoacoustic wave detector which utilized the index of refraction change at a glass/water interface to get two dimensional photoacoustic images of small absorbers, including hair and 0.5 mm spheres. Backprojection was used to image the data. Sets of two dimensional images were used to acquire three dimensional reconstructions. Resolution was limited by the magnification of the camera and pixel size, though the pulse duration of the acoustic wave inducing laser, 10 ns, limited the resolution to $15\ \mu\text{m}$.

Viator *et al.* [49] localized 2 mm acrylamide spheres embedded in turbid acrylamide tissue phantoms using a PVDF transducer and a convolution–backprojection scheme, as described in chapter 5. The spheres were localized to within 0.5 mm of their true location at a depth of 20 mm.

Jacques *et al.* [50] investigated the use of a photoacoustic probe for use in determining treatment depth after PDT of esophageal cancer. This study was the preliminary work for the probe design in chapter 6.

This area of photoacoustics may be the most active, though a true *in vivo* application of tumor imaging has yet to be demonstrated. The current imaging methods, including backprojection, will need to overcome the problems of optical scattering and penetration in order to probe deeply embedded ($> 1\text{ cm}$) tumors. The problems of background absorption, which decreases the contrast of the embedded photoacoustic source, need to be addressed

in order to fully develop the imaging techniques.

1.3.2 Analytical Monitoring

Analytic monitoring includes hemoglobin and blood glucose monitoring *in vivo*. Rosen cwaig [51] proposed using photoacoustic spectroscopy to enhance the signal to noise ratio in NIR measurements of glucose in the bloodstream. Bednov *et al.* [52] used photoacoustic means to measure the distribution of light energy in tissue phantoms and in rabbit sclera *in vivo*. They detected changes in μ_{eff} photoacoustically and correlated the change to the glucose concentration in blood. Fainchtein *et al.* [53] used a photoacoustic spectroscopic method to measure hemoglobin content *in vitro* and *in vivo*. Further uses of photoacoustic spectroscopy include work by Sigrist *et al.* and Oomens *et al.* [54, 55]. They performed noninvasive measurements on gases, with the aim of measuring components in exhaled air for diagnostic purposes.

1.3.3 Interaction of Light and Sound

Yao *et al.* [56] used ultrasonic modulation of laser light in order to analyze resultant speckle patterns with a CCD camera to determine optical and mechanical properties of tissue in the light beam. The ultrasound was used to induce changes in the speckle field, which were related to the mechanical properties. Its proposed use was for tomographic imaging of breast cancer. Tissue phantoms made from chicken breast of up to 15 mm thick were used for imaging of buried objects. Two dimensional scan were acheived with an object 4.0 mm X 2.7 mm X 6.2 mm, with an image resolution of about 2 mm.

This area of photoacoustics, more often referred to as acousto-optics [57], has more in common with optical imaging schemes, though the introduction of ultrasonic modulation may lend an additional tool for discriminating diseased from healthy tissue. While different from the photoacoustic imaging discussed above, the acousto-optics may prove to be a useful imagin modality.

1.4 Acoustic Propagation

Acoustic propagation can be described by the mathematical theory of waves [57–67]. Acoustic waves can be generated in fluids and solids, though in both media their propagation is characterized by longitudinal, or compressive, waves. Even though waves in water due to tidal forces are transverse, meaning that the vibrations are in a direction orthogonal to the direction of wave propagation, these waves can be used as a means to illustrate many properties of acoustic propagation. Like water waves, there is no net flow of the particles in the medium during acoustic propagation. The momentum and energy transfer is accomplished by interactions between adjacent particles in the medium. Other properties of photoacoustic waves can also be visualized using water waves, *i.e.*, the circular attenuation of pressure from a point disturbance in a pool of water as $1/r$.

1.4.1 Equations of State

This introduction will concentrate on acoustics in fluids, though they apply in general to solids. The acoustic wave equation can be derived from the equations of state of a fluid. These equations relate the forces on a fluid to the deformations experienced by the fluid as a result of those forces. In a perfect gas, the relation

$$P = \rho r T_k \quad (1.2)$$

where P is the total instantaneous pressure on the gas, ρ is the density, r is a constant that depends on the particular gas, and T_k is the temperature. For a system where the boundaries are adiabatic, and hence the entropy is constant and the temperature varies, the equation of state is

$$\frac{P}{P_0} = \left(\frac{\rho}{\rho_0} \right)^\gamma \quad (1.3)$$

Where the $_0$ subscript denotes the quantity in equilibrium, *i.e.*, in the absence of dynamic forces, and γ is the ratio of specific heats at constant pressure and constant volume. For a fluid other than a perfect gas, the adiabatic equation of state is

$$p = \rho_0 \left(\frac{\partial P}{\partial \rho} \right)_{\rho_0} s \quad (1.4)$$

where p is the acoustic pressure and $s = \frac{\rho - \rho_0}{\rho_0}$ is the condensation.

1.4.2 Equation of Continuity

The equation of continuity is another factor in deriving the acoustic wave equation. It relates the net flow through a volume element with the rate of mass increase and is expressed

$$\frac{\partial \rho}{\partial t} + \nabla \cdot (\rho \vec{u}) = 0 \quad (1.5)$$

where ∇ is the spatial derivative and u is the particle velocity. Using the fact that $\rho = \rho_0(1 + s)$ and ρ_0 is constant for both spatial and time derivatives, then the equation of continuity 1.5 becomes linear

$$\frac{\partial s}{\partial t} + \nabla \cdot \vec{u} = 0 \quad (1.6)$$

1.4.3 Euler Equation

The third component in deriving the acoustic wave equation is the force equation, or Euler equation. For an inviscid fluid, one that has no viscosity, a fluid particle accelerates according to Newton's second law, $\vec{a} = d\vec{f}/dm$, where \vec{a} is the acceleration, $d\vec{f}$ is the force, and dm is the mass of the fluid particle. The force can be written

$$d\vec{f} = -\nabla P dV \quad (1.7)$$

The acceleration is

$$\vec{a} = \frac{\partial \vec{u}}{\partial t} + u_x \frac{\partial \vec{u}}{\partial x} + u_y \frac{\partial \vec{u}}{\partial y} + u_z \frac{\partial \vec{u}}{\partial z} \quad (1.8)$$

With the operator defined as

$$(\vec{u} \cdot \nabla) = u_x \frac{\partial}{\partial x} + u_y \frac{\partial}{\partial y} + u_z \frac{\partial}{\partial z} \quad (1.9)$$

then the acceleration is

$$\vec{a} = \frac{\partial \vec{u}}{\partial t} + (\vec{u} \cdot \nabla) \vec{u} \quad (1.10)$$

With the substitution of $dm = \rho dV$ into $d\vec{f} = \vec{a} dm$ we have the Euler equation

$$-\nabla P = \rho \left[\frac{\partial \vec{u}}{\partial t} + (\vec{u} \cdot \nabla) \vec{u} \right] \quad (1.11)$$

This equation can be linearized to

$$\rho \frac{\partial \vec{u}}{\partial t} = -\nabla p \quad (1.12)$$

recalling that P is the instantaneous pressure of the fluid at any point and p is the acoustic pressure.

1.4.4 Acoustic Wave Equation

Using equations 1.4, 1.6, and 1.13, the linear acoustic wave equation is derived. Taking the time derivative of the continuity equation, 1.6, and the divergence of the Euler equation, 1.13, and the adiabatic equation of state, 1.4, to change the result from condensation to pressure,

$$\nabla^2 p - \frac{1}{c^2} \frac{\partial^2 p}{\partial t^2} = 0 \quad (1.13)$$

where c is the phase speed and is given by the relation $c = (\beta/\rho_0)^{\frac{1}{2}}$, where β is the bulk modulus. ∇^2 is the Laplacian operator. When the wave equation is Fourier transformed, it becomes the Helmholtz equation. This is done by replacing the time derivatives with the appropriate Fourier pair as the coefficient, *i.e.*,

$$\frac{\partial}{\partial t} \longrightarrow -i\omega \quad (1.14)$$

This equation takes away the time dependence, as the time derivatives are replaced by the complex coefficient in equation 1.14. Thus the Helmholtz equation is

$$\nabla^2 p - k^2 p = 0 \quad (1.15)$$

where $k = \frac{2\pi}{\lambda}$ is the wave number.

1.4.5 Velocity Potential

Since the curl of a gradient vanishes, equation 1.13 shows that the particle velocity is irrotational, so that it can be expressed as the gradient of a scalar function, $\vec{u} = \nabla\phi$, where ϕ is the velocity potential. Substituting the velocity potential into the Euler equation, 1.13, shows that the time derivative of the velocity potential is related to the acoustic pressure by the density

$$p = -\rho_0 \frac{\partial \phi}{\partial t} \quad (1.16)$$

Thus, the velocity potential is also a solution to the wave equation. The velocity potential can be interpreted physically as the absence or shear, turbulence, or rotational flow, since

the particle velocity is the gradient of the velocity potential, and thus its curl must vanish. This is true only with the idealized derivation shown here, though this linear model does extremely well for acoustic propagation for non-shock waves [67]. The velocity potential is useful in photoacoustics in that it can be easily obtained by integrating the pressure over time, giving a positive waveform that can be used, for example, in backprojection image reconstruction.

1.4.6 Plane Waves

In plane wave analysis, the acoustic waves vary in time and with one of the three Cartesian coordinates, *i.e.*, x . Then the Laplacian operator takes the form $\nabla^2 = \frac{\partial^2}{\partial x^2}$. Thus the acoustic wave equation becomes simply

$$\frac{\partial^2 p}{\partial x^2} - \frac{1}{c^2} \frac{\partial^2 p}{\partial t^2} = 0 \quad (1.17)$$

The general solution of which is

$$p(x, t) = f(x - ct) + f(x + ct) \quad (1.18)$$

The first term on the right side is a plane wave traveling in the positive x direction, while the second term is the identical wave traveling in the negative x direction, with wave velocity, c . Thus a plane wave is a solution to the wave equation in which the acoustic wave equations vary with time, while the wave has constant phase in any plane orthogonal to the wave propagation. The plane wave model is used throughout this dissertation, including the depth profiling method and the propagation time analysis.

1.4.7 Acoustic Impedance

Acoustic impedance is the ratio of the acoustic pressure and the particle speed.

$$z = \frac{p}{u} \quad (1.19)$$

In the case of plane waves, the simple relation is

$$z = \rho_0 c \quad (1.20)$$

Equation 1.20 is derived by determining the particle velocity of a plane wave by substituting the plane wave solution into Euler's equation and solving for the particle velocity. The ratio of the plane wave solution and the particle velocity yields $z = \omega/k\rho_0 = \rho_0c$. This relation is often called the characteristic acoustic impedance. This impedance is a direct analog to the optical index of refraction for light propagation. This equation describes the acoustic propagation across all boundaries for plane waves, and is also used to justify the use of phantoms with sound speeds and densities similar to tissue.

1.4.8 Spherical Waves

The development of spherical waves is shown in the introduction of chapter two. The result, from symmetry of radial spreading, gives the spherical wave equation,

$$\frac{\partial^2(rp)}{\partial r^2} - \frac{1}{c^2} \frac{\partial^2(rp)}{\partial t^2} = 0 \quad (1.21)$$

with the general solution of

$$p(r, t) = \frac{1}{r} (f(r - ct) + f(r + ct)) \quad (1.22)$$

The harmonic solution is, therefore,

$$p(r, t) = A \frac{e^{i(\omega t - kr)}}{r} \quad (1.23)$$

where A is the expression for amplitude, determined by boundary conditions, ω is the angular frequency of the harmonic wave, and k is the wavenumber. This equation expresses a harmonically oscillating source, scaled by some amplitude, A , and dropping off as $1/r$. This behavior is consistent with that expected from the symmetry afforded by a spherical source.

1.4.9 Cylindrical Waves

For cylindrical symmetry, the wave equation can be transformed into cylindrical coordinates, with the azimuthal and the axial components neglected. The wave equation can then be expressed as

$$\frac{1}{r} \frac{\partial}{\partial r} \left(r \frac{\partial p}{\partial r} \right) - \frac{1}{c^2} \frac{\partial^2 p}{\partial t^2} = 0 \quad (1.24)$$

As in the spherical case, substitution of \sqrt{r} into the solution, due to the attenuation in cylindrical geometry, gives the expression of the wave equation,

$$\frac{\partial^2(\sqrt{r}p)}{\partial r^2} - \frac{1}{c^2} \frac{\partial^2(\sqrt{r}p)}{\partial t^2} + \frac{\sqrt{r}p}{4r^2} = 0 \quad (1.25)$$

The cylindrical Helmholtz equation is

$$\frac{d^2p}{dr^2} + \frac{1}{r} \frac{dp}{dr} + k^2p = 0 \quad (1.26)$$

The solution to this equation is in the form of Hankel functions of the first kind, the real part of which is the Bessel function, which is important in the modeling of plane piston sources. The solution can be expressed,

$$p = AH_0^{(1)}(kr) \quad (1.27)$$

1.4.10 Boundary Conditions

A complete description of acoustic propagation requires not only the solution to the homogeneous wave equations presented here, but includes boundary conditions at interfaces. The requirements of the boundary conditions are the acoustic pressure and normal component of the fluid velocity remain continuous at the interface. These conditions in conjunction with the acoustic impedance yields the reflection and transmission through an interface. Snell's law is used to determine the transmission and reflection, with the reflection at normal incidence, in terms of the impedances, expressed as

$$R = \frac{z_2 - z_1}{z_2 + z_1} \quad (1.28)$$

where R is the ratio of reflected and incident intensities of the wave reflected at an interface between two media, and z_1 is the impedance of the first medium and z_2 is the impedance of the second medium.

1.4.11 Monopoles

Monopole, or simple, sources of acoustic radiation are expressed by the spherical solution to the wave equation, shown above. Solutions of the linear acoustic wave equation can be superimposed upon each other to create solutions for composite sources. Such sources

include the important dipole and line sources, both of which may be used to create even more complex sources, such as the piston source. The piston source is composed of a series of line sources of various lengths, such that they form a disk. This geometry is important in photoacoustics and will be discussed in more depth in chapter two.

1.4.12 Dipole Source

Two monopole sources separated by a distance, d , can be expressed as

$$p(r, t) = \frac{A}{r} \left(\frac{e^{-ik\Delta r_1}}{1 + \Delta r_1/r} - \frac{e^{-ik\Delta r_2}}{1 - \Delta r_2/r} \right) e^{i(\omega t - kr)} \quad (1.29)$$

where r_1 and r_2 are the distances from the first and second sources to the observation point and Δr_1 and Δr_2 are the differences in distance between the line from the origin to the observation point and the line from points r_1 and r_2 , respectively. θ is the angle formed by the horizontal axis and the line from the origin to the observation point. These sources have the same harmonic frequency, ω , though they are 180° out of phase. The radiation pattern is shown in figure 1.3. In the far field, where $r \gg d$ [67], then

$$p(r, \theta, t) = -i \frac{2A}{r} \sin\left(\frac{1}{2}kd \sin \theta\right) e^{i(\omega t - kr)} \quad (1.30)$$

The radiation pattern for a dipole is shown in figure 1.3.

1.4.13 Line Source

The line source can be derived by integrating a series of simple sources in space along a curve of zero curvature. A large number of cylinders of length dx and radius a with total length L have a source strength dQ

$$dQ = U_0 2\pi a dx \quad (1.31)$$

where U_0 is the maximum particle velocity of the sources and a is the cylinder diameter. Each cylinder has an increment of pressure equal to

$$dp = i \frac{\rho_0 c k}{4\pi r'} U_0 2\pi a e^{j(\omega t - kr)} dx \quad (1.32)$$

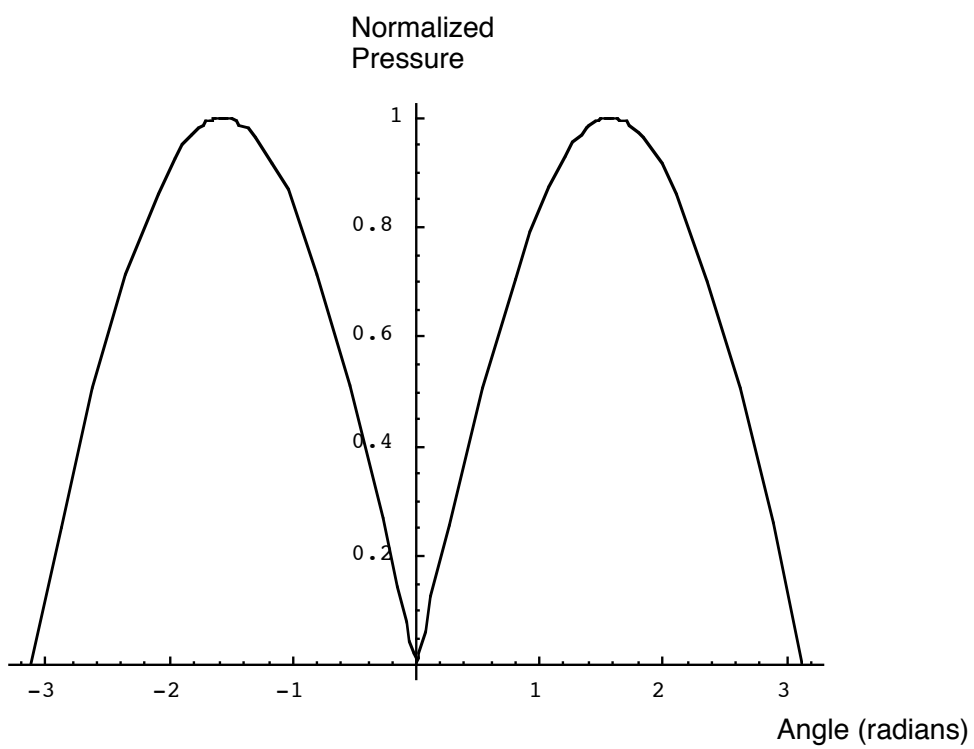


Figure 1.3: The pressure amplitude of a dipole source as a function of angle in the far field.

at (r, θ) , where $r' = r - x \sin(\theta)$. The total pressure is found by integrating the pressure sources over the length of all sources together so that [67]

$$p(r, \theta, t) = \frac{1}{2} j \rho_0 c U_0 \frac{a}{r} k L \exp j(\omega t - kr) \left[\frac{\sin(\frac{1}{2} k L \sin \theta)}{\frac{1}{2} k L \sin \theta} \right] \quad (1.33)$$

1.5 Optically Induced Acoustic Waves

There are several mechanisms for optically inducing acoustic waves [7]. These mechanisms include dielectric breakdown, vaporization and ablation, radiation pressure, and thermoelastic expansion. The methods in this dissertation are all of the latter type. The thermoelastic process depends on a condition known as stress confinement. This condition occurs when optical energy is deposited in an absorbing medium in a period of time shorter than that required for the energy to dissipate acoustically, *i.e.*, the laser pulse is shorter than the time required for sound to traverse the absorption depth. The condition of stress confinement can be expressed by the relation,

$$\tau < \frac{\delta}{c_s} \quad (1.34)$$

where δ is the absorption depth and c_s is the speed of sound in the medium. The absorption depth is the reciprocal of the optical absorption coefficient and is simply the depth at which the optical energy is attenuated by $1/e$. If the pulse duration of a laser is less than δ/c_s , the pulse is considered stress confined.

If a laser pulse is stress confined, then the region of optical energy deposition is heated, creating a stress on the medium. The linear acoustic wave equation may be used to describe the phenomenon, with the addition of a source term that describes the heated region. The full treatment of the generation of photoacoustic waves can be found in Paltauf *et al.* [68] and Gusev *et al.* [4]. Using the velocity potential, it can be written as

$$\nabla^2 \psi - \frac{1}{c^2} \frac{\partial^2 \psi}{\partial t^2} = \frac{\beta}{\rho C_p} S \quad (1.35)$$

where β is the thermal expansion coefficient and C_p is the specific heat at constant pressure and S is the heat generated per unit volume and time. S can be described as an instantaneous heat deposition

$$S(r, t) = W(r) \delta(t) \quad (1.36)$$

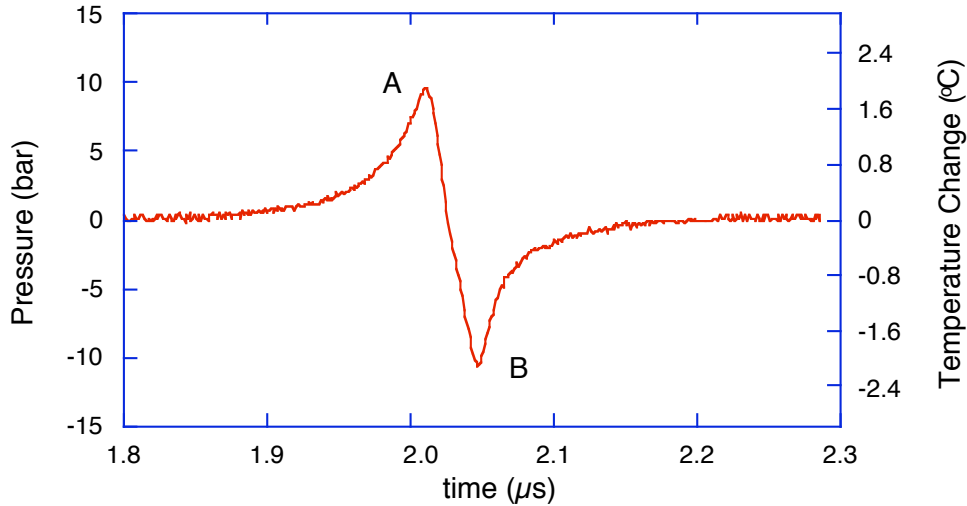


Figure 1.4: The measured acoustic wave as a function of time. The wave was induced by irradiating a plane surface of optically absorbing acrylamide gel, with $\mu_a = 180 \text{ cm}^{-1}$. Peak “A” denotes the surface of the gel, while “B” represents the tensile wave peak.

where $W(r)$ is the absorbed volumetric energy density and $\delta(t)$ is the Dirac delta. Proceeding as Paltauf *et al.* and Gusev *et al.*, the velocity potential is derived, from which the pressure is derived. Using an acoustic interface that approximates laser energy deposition in an absorbing liquid by an optical fiber, the solutions

$$p(z, t) = \frac{1}{2}\Gamma\mu_a H_0 e^{-\mu_a(z-ct)} + \frac{1}{2}\Gamma\mu_a H_0 e^{-\mu_a(z+ct)} \quad (1.37)$$

where Γ is the unitless Grüneisen coefficient, which is the fraction of deposited energy that is available for acoustic energy and H_0 is the radiant exposure. The first term is the downward plane wave, while the second term is the upward plane wave. The generation is detailed experimentally as follows.

A photoacoustic stress giving rise to the traveling acoustic wave is shown in (Figure 1.4).

This acoustic wave was generated by a laser pulse incident on an absorbing gel surface in air. The acoustic wave is shown by pressure as a function of time as seen by the acoustic detector. The peak denoted by “A” indicates the surface of the gel. The region to the left of the peak represents the deeper layers of the gel. The pressure amplitude decreases

with depth, since the optical energy decreases due to the previous absorption at shallower depths. The peak denoted by “B” is a tensile wave created at the surface of the gel. The gel/air interface, being an acoustic mismatch, constituted a free surface which caused the outward going wave to reflect back into the gel with negative amplitude.

The geometry of the energy deposition and the boundary conditions of the medium determine the acoustic wave propagation, though the optical energy deposition describes the initial acoustic wave profile. In the case of a homogeneous optical absorber, such as a dye solution or gel, the initial energy deposition is described by Beer’s law,

$$E(z) = E_0 \exp(-\mu_a z) \quad (1.38)$$

where $E(z)$ is the radiant exposure as a function of depth, E_0 is the radiant exposure at the surface, and μ_a is the optical absorption coefficient. The initial acoustic wave profile shares the same exponential shape, where the amplitude of the wave corresponds to the energy deposition of the laser beam. Figure 1.5 shows the region of the acoustic wave shown in Figure 1.4 as a function of depth in the gel. The portion of the wave shown here is from the peak “A” and the region to the left of it. Thus the initial acoustic wave is shown with an exponential curve fit, using the product of the optical absorption coefficient and depth as the argument of the exponential. For a homogeneous absorbing layer, the absorption coefficient, μ_a , can be derived from such a fit. This thermoelastic description was used in this dissertation along with the wave equation modeling.

1.5.1 A Note on the Grüneisen Coefficient

The Grüneisen coefficient, Γ , is the ratio of laser energy that is available for conversion into acoustic energy. For tissue and tissue-like media, it is approximately 0.11 for 20°C and 0.125 for 25°C At 90°C Γ is 0.5. [24]. Γ is related to the thermal and bulk properties of the medium and can be expressed as

$$\Gamma = \frac{M\beta}{\rho C_p} = \frac{\beta c_s^2}{C_p} \quad (1.39)$$

where M is the bulk modulus, β is the thermal expansivity, ρ is the density, C_p is the heat capacity at constant pressure, and c_s is the sound speed.

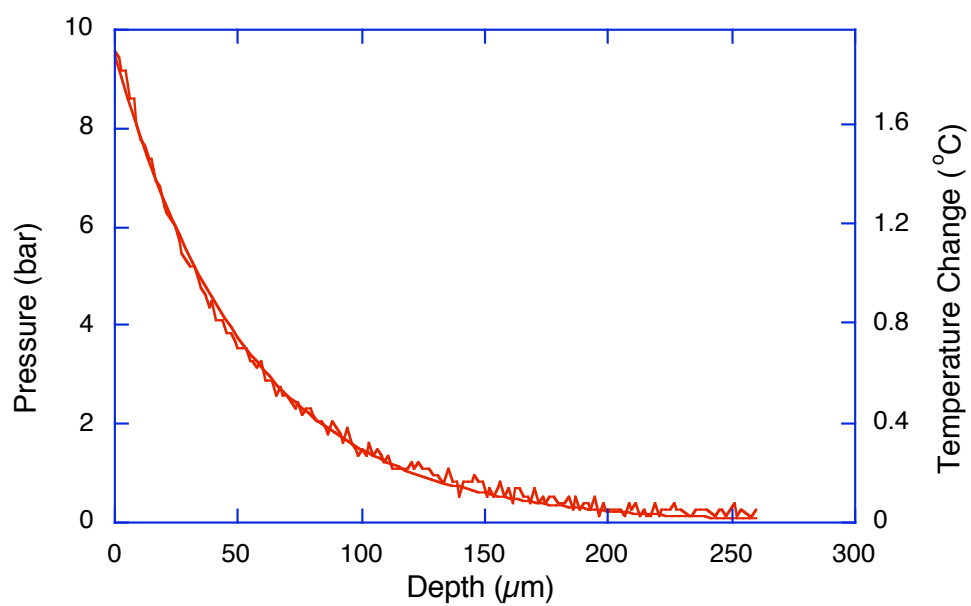


Figure 1.5: The acoustic wave from Figure 1.4 as a function of depth. The highest pressure is at the surface, where the optical energy was highest. The optical energy available for absorption ($\mu_a = 180 \text{ cm}^{-1}$) and subsequent conversion to acoustic energy falls exponentially according to Beer's Law.

1.5.2 Instrumentation

The experiments described in this dissertation usually involve an acoustical stress detected by a piezoelectric detector, either PVDF or lithium niobate. An acoustic wave, induced in tissue or a tissue phantom, propagated until it reached the detector. The detector was coupled to an oscilloscope with an input impedance of $1\text{M}\Omega$ for nonamplified signals. The input impedance for the oscilloscope was 50Ω for amplified signals, as the input impedance of the amplifier was $1\text{k}\Omega$. These high input impedances were used to integrate the charge accumulated on the piezoelectric detectors from acoustic disturbances. In the case of PVDF, the film was coated with aluminum on either side of a $25\ \mu\text{m}$ sheet of PVDF. Deformation of the PVDF created an electric field which in turn accumulated charge on the capacitive aluminum plates on either side of the PVDF. Integrating the charge results in a waveform proportional to the pressure of the acoustic disturbance. An additional integration in time yields the velocity potential, as described in section 1.3.5.

1.6 Goals

Photoacoustic methods in biomedical optics provide a diagnostic tool that probes optical and acoustic properties of tissue media while exploiting the advantages of wave propagation in a homogeneous medium. This dissertation presents a method for depth profiling of optical properties using an acoustic method and a method for localizing an optically induced spherical source by acoustic time domain methods.

Chapter 2 introduces standard acoustical theory of spherical and planar harmonic sources, then shows that the pulsed source can be described as a sum of the harmonic solutions. Acoustic attenuation in an optically absorbing liquid was measured and modeled as the field of a plane piston source on the propagation axis. Acoustic dispersion is measured in a diffraction-free source. Diffraction effects were measured as the interference of a boundary wave with the plane wave in a piston acoustic source. The far field boundary as predicted by Sigrist [7] was confirmed by this interference phenomenon.

Chapter 3 presents a method for determining the absorption coefficient of layered media, where absorption dominates scattering, using plane wave acoustical methods. An

acoustic wave is generated in layered acrylamide gels and a stained biomaterial (Figure 1.6). The wave is detected with a piezoelectric transducer. The signal is analyzed by an algorithm based on Beer's law and the absorption coefficient is derived for the gels and stained biomaterials.

Chapter 4 uses time domain methods to localize spherical photoacoustic sources in acrylamide gels. Small, optically absorbing spheres were made and placed within clear and turbid gel phantom (Figure 1.7). The gels were irradiated with laser energy, resulting in the generation of acoustic waves from the optically spheres. The optically thick spheres were modeled as acoustic sources made from a hemispherical shell. The beam pattern for such a shell was computed and graphed. The acoustic waves are detected by a PVDF transducer which was translated over the surface of the gel to make different detection points. The acoustical propagation time was used in a computational scheme to locate the photoacoustic sources. The computational method used the detected acoustic waveforms and correlated the propagation times from a waveform from a different detector position. The correlation created a density map in two dimensions of the photoacoustic source location. An image source from a reflecting boundary was created and also mapped in the density plot. Analysis of acoustic wave shape of irradiated spheres also provided sphere size information for spheres in clear and turbid media. A simple geometric scheme afforded this information. Finally, dipoles, made from sphere pairs, were irradiated and a minimum center to center distance for sphere discrimination was determined.

Finally, in Chapter 5, an endoscopic photoacoustic probe is designed and tested for use in PDT treatment of esophageal cancer. The probe, measuring less than 2.5 mm in diameter, was designed to fit within the lumen of an endoscope that will be used to observe an esophagus after PDT. PDT treatment resulted in a blanched, necrotic layer of cancerous tissue over a healthy, deeper layer of perfused tissue. The photoacoustic probe was designed to use acoustic propagation time to determine the thickness of the blanched surface of the esophagus, which corresponds to treatment depth. A side-firing 600 μm fiber delivered 532 nm laser light to induce acoustic waves in perfused layers of the esophagus, which lie underneath the blanched (treated) layer. A PVDF transducer detected the induced acoustic waves and sent the signal to an oscilloscope. The probe was tested on clear

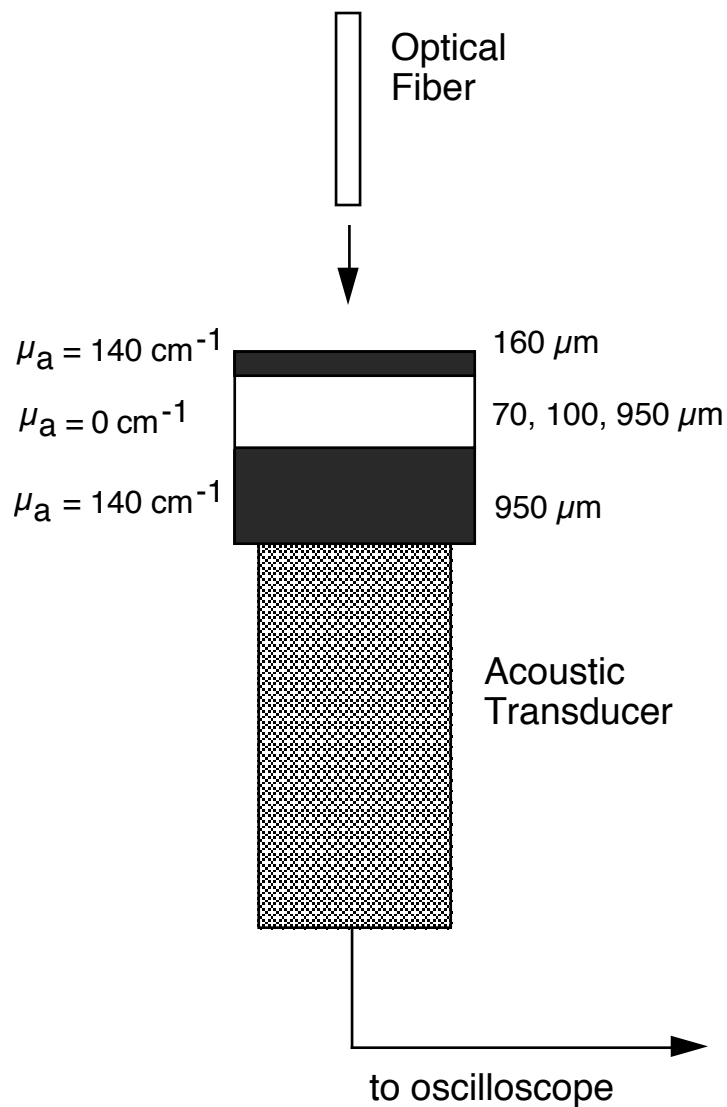


Figure 1.6: The depth profiling experimental set up relies on optically induced acoustic waves traveling through the acoustic medium and being detected by a piezoelectric transducer. The gels resting on the transducer may be homogeneous or layered, as shown here. Alternatively, a stained biomaterial could be substituted for the gel.

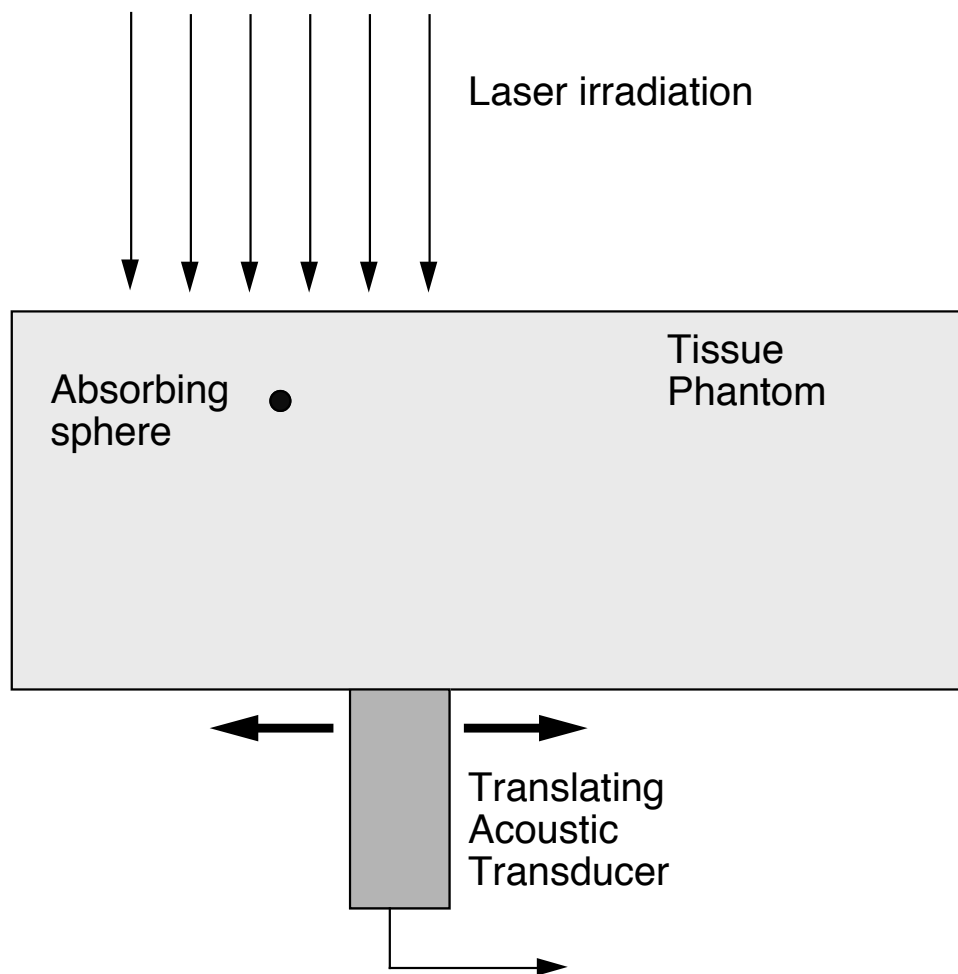


Figure 1.7: An embedded sphere in turbid acrylamide gel is irradiated with laser light, giving rise to an acoustic field. The acoustic field is sampled by a translating PVDF transducer.

and turbid tissue phantom layers over optically absorbing dye solution. Additionally, a vein model was made with a tube filled with red dye submerged in a turbid liquid. The probe scanned the vein and the resulting signals were arranged graphically to localize the vein model. The probe also irradiated normally perfused and underperfused fingertips from a human volunteer, *in vivo*. The underperfusion was induced by applying pressure to the skin surface. The probe indicated the normally perfused finger with acoustic waves of greater amplitude than the underperfused finger.

Chapter 2

Broadband photoacoustic pulse propagation in tissue phantoms

2.1 Introduction

Harmonic acoustic wave propagation is well developed in standard text books in acoustics [57,58,60–63,67]. This chapter will investigate acoustic propagation in tissue phantoms using broadband pulsed sources, originating from stress confined, laser energy deposition. The condition of stress confinement is achieved when the laser energy is deposited in less time than the energy can propagate away acoustically from the deposition volume. In the experiments described in this chapter, stress confinement is achieved by a 5 ns laser pulse. Acoustic attenuation, diffraction, and dispersion are studied in these experiments. The boundary of the near and far fields is shown to agree with the predicted boundary from the equation [7]

$$z_d = \frac{\mu_a d^2}{8} \quad (2.1)$$

Where d is the laser beam diameter and μ_a is the optical absorption coefficient of the absorbing medium. The spherical sources solution is presented, as is the piston source, which is shown to be a model of photoacoustic generation when a circular laser spot is incident upon a planar absorbing medium. Thus a disk of irradiation is formed, the dimensions of which are described by the absorption depth ($1/\mu_a$) of the planar absorbing medium and the diameter of the laser spot (figure 2.1). This disk of irradiation can be modeled as a piston head creating a pressure wave into the medium. A pressure wave is also created out of the medium, though the interface created by the optically absorbing

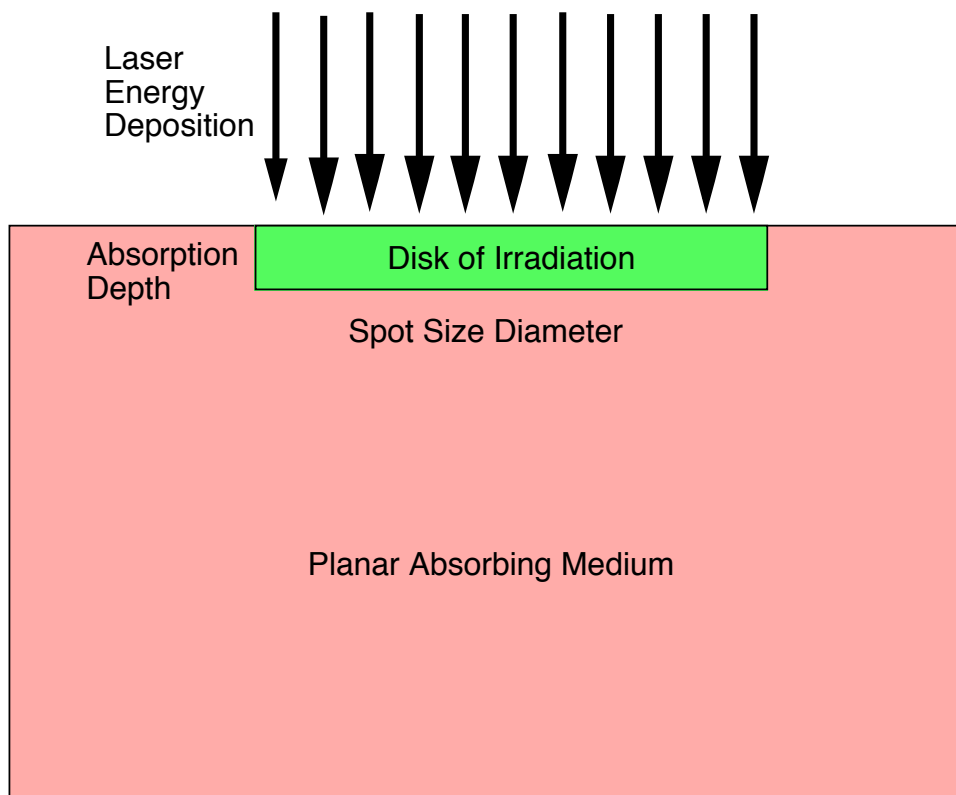


Figure 2.1: A disk of irradiation is formed by incident laser irradiation. The disk dimensions are given by the laser spot diameter and the absorption depth. In a stress confined laser pulse, the disk may act as a piston head in the fluid, imparting a pressure wave into the fluid, followed by an inverted reflected wave of equal amplitude imparted by the free surface of the air/fluid interface.

medium (usually tissue or water) with air creates a reflection resulting in an acoustic wave following the initial wave, though inverted in amplitude.

2.1.1 Acoustical Theory

Acoustic fields from complex sources can be derived by superposition of point sources, as the acoustic wave equation is linear. Thus, the point source solution, given in chapter 1, can be used to construct acoustic sources of arbitrary geometry, though analytic solutions are practical only for a few representative geometries. This section develops the solutions to spherical and plane piston sources, as these forms are applicable to the photoacoustic sources studied in this dissertation. The cylindrical source is not discussed as it is not directly applicable to the methods pursued here.

The spherical source solution is derived below. Stress confined optical absorption of symmetric regions, such as small, bulbous tumors, can be modeled by the spherical source. Other structures *in vivo* may also be applicable to a spherical photoacoustic source, such as a small spot size incident on a homogeneous optical absorber with an absorption coefficient where the optical penetration depth is comparable to the spot diameter. Next, the solution to the plane piston source is derived. The plane piston source is applicable to the situation of a stress confined laser pulse incident upon an absorbing plane layer, where the spot diameter is much greater than the absorption depth. This situation can be found in locally flat tissue surfaces of high optical absorption coefficient. Additionally, dyed tissue layers, such as that found in tissue welding applications, may be suitably modeled by the plane piston in photoacoustic applications [69].

Spherical Sources

A spherical acoustic source can be modeled by the acoustic wave equation in spherical coordinates. The spherical Laplacian is

$$\nabla^2 = \frac{\partial^2}{\partial r^2} + \frac{2}{r} \frac{\partial}{\partial r} + \frac{1}{r^2 \sin \theta} \frac{\partial}{\partial \theta} \left(\sin \theta \frac{\partial}{\partial \theta} \right) + \frac{1}{r^2 \sin^2 \theta} \frac{\partial^2}{\partial \phi^2} \quad (2.2)$$

With spherical symmetry, the pressure is a function of r only, so the wave equation is reduced to

$$\frac{\partial^2 p}{\partial r^2} + \frac{2}{r} \frac{\partial p}{\partial r} = \frac{1}{c^2} \frac{\partial^2 p}{\partial t^2} \quad (2.3)$$

where c is the sound speed and p is the acoustic pressure. Pressure will drop off as $1/r$, as the intensity is given by $I = \frac{p^2}{2\rho_0 c}$. If the quantity rp is used as the dependent variable, then the amplitude will be independent of r , yielding

$$\frac{\partial^2(rp)}{\partial r^2} = \frac{1}{c^2} \frac{\partial^2(rp)}{\partial t^2} \quad (2.4)$$

Thus one can substitute rp into the general solution of the wave equation from section 1.3.6 and solve for p yielding

$$p = \frac{1}{r} f_1(ct - r) + \frac{1}{r} f_2(ct + r) \quad (2.5)$$

where, as in chapter 1, the first term on the right side is the diverging spherical wave from a point source and the second term is the spherical wave converging into the point source. The harmonic solution to this equation is

$$\mathbf{p}(r, t) = \frac{\mathbf{A}}{r} \exp(j\omega t - kr) \quad (2.6)$$

where ω is the harmonic frequency, k is the wavenumber, and \mathbf{A} is the complex amplitude. The bold face indicates a complex quantity. A scalar notion of the pressure can be obtained by looking at the intensity, defined above, or by taking the magnitude of the complex pressure. This is also the equation for a pulsating sphere where the displacement of the surface in a vibration is much less than the radius a . To determine the amplitude \mathbf{A} , assume the sphere surface is vibrating with frequency ω and speed amplitude U_0 . Then,

$$\mathbf{u}(a, t) = U_0 \exp(j\omega t) \quad (2.7)$$

\mathbf{u} is the particle velocity, which is the the actual velocity of the disturbed particles in the acoustic path. It is obtained by taking the first time derivative of the particle displacement. The acoustic impedance at the surface is

$$\mathbf{z}(a) = \rho_0 c \cos \theta_a \exp j\theta_a \quad (2.8)$$

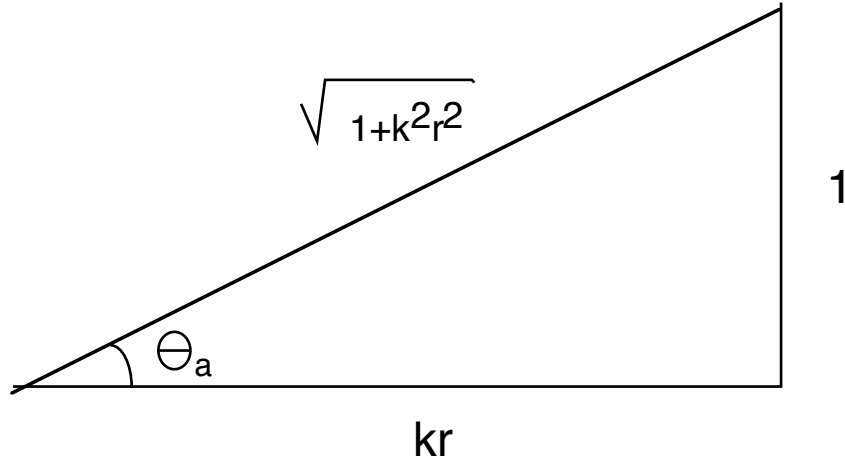


Figure 2.2: Determining phase angle from the product of the wavenumber, k , and the radial displacement, r .

where ρ_0 is the equilibrium density. While the specific acoustic impedance in plane wave theory may be expressed as $z = \rho_0 c$, in spherical waves, the impedance is scaled by the cosine of the phase angle. Geometrically this is shown by figure 2.2 Unlike the plane wave case, particle speed is not in phase with the pressure. The phase diagram (Figure 2.2 shows the relation of the product of the wavenumber, k , and the displacement. In the present case, the displacement is a , so that the angle described in the phase diagram is designated θ_a . Using the simple relation that links acoustic impedance and pressure, $\mathbf{z} = \frac{p}{u}$ (Section 1.3.6),

$$\mathbf{p}(a, t) = \rho_0 c U_0 \cos \theta_a \exp j(\omega t + \theta_a) \quad (2.9)$$

so that equation 2.6 is now

$$\mathbf{p}(r, t) = \rho_0 c U_0 \frac{a}{r} \cos \theta_a \exp j[\omega t - k(r - a) + \theta_a] \quad (2.10)$$

Piston Sources

A baffled source is one which is in close proximity to a large, rigid, reflecting boundary. In the case of a laser spot on an absorbing medium in air, the air/medium interface provides such a boundary, as long as the acoustic impedance for the medium is significantly different

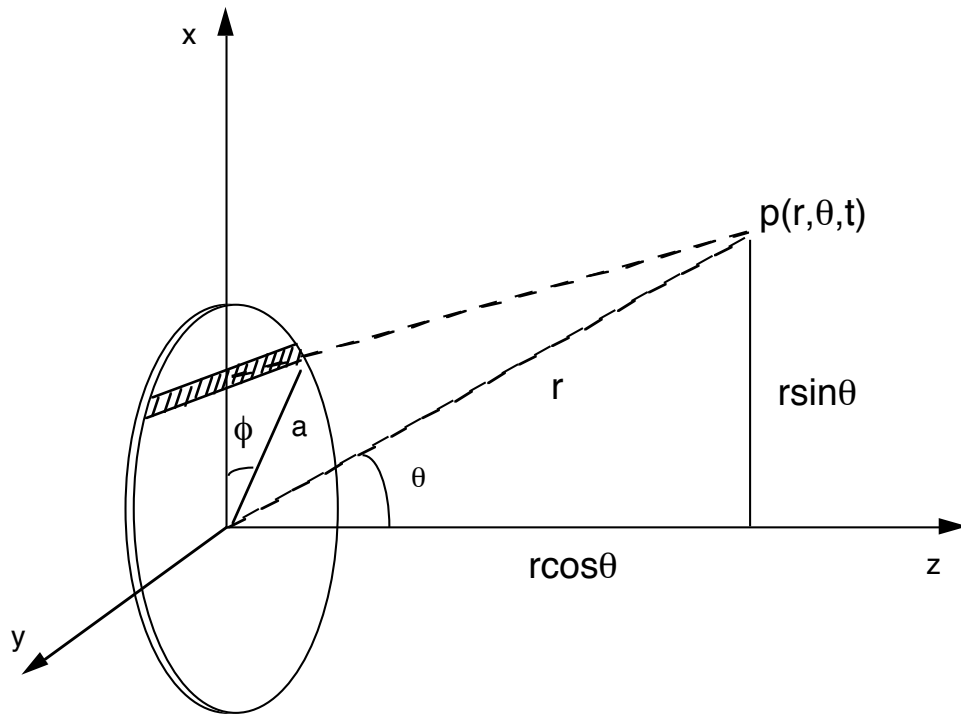


Figure 2.3: The acoustic field of a plane piston source can be derived by integrating a series of line sources that make up the disk. Here r is the distance from the origin to the observatin point, while r' is the distance from a point on the line source to the observation point.

from air. In the case of tissue and tissue-like media, this requirement is fulfilled as the reflectivity is described by the relation,

$$R(\theta) = \frac{\rho_2 k_{1,z} - \rho_1 k_{2,z}}{\rho_2 k_{1,z} + \rho_1 k_{2,z}} \quad (2.11)$$

where $R(\theta)$ is the reflection coefficient (value of 0–1) of the acoustic wave as a function of the incident angle θ , ρ_i is the density of the media, and $k_{i,z} = \frac{\omega}{c_i} \sin \theta_i$ with $i = 1, 2$ for medium 1 or 2, respectively. With the density of tissue-like media at 1 g/cm^3 [70] and the density of air negligible, the reflection is nearly 100%.

The pressure from a baffled, plane circular piston source can be derived by integrating a series of baffled line sources (figure 2.3). If a source is mounted in the rigid boundary, then the reflected wave is in phase and coincident with the wave that generated it, making the pressure amplitude doubled and the intensity quadrupled. This is the basic result of

baffled sources, owing to the Acoustic Reciprocity Theorem [57, 60, 64, 67], which states that if an acoustic source and receiver are switched in space, then the received signal is unchanged. The pressure from a line source can be derived from integrating a line of short cylinders, modeled on a superposition of simple sources of a certain source strength. The pressure can be stated as [57, 60, 65, 67]

$$d\mathbf{p} = j\rho_0 c \frac{U_0}{\pi r'} ka \sin(\phi) \exp j(\omega t - kr') dx \quad (2.12)$$

Where a is the piston radius and U_0 is the maximum particle speed of the cylinders. Integrating the line sources, with the far field approximation allowed by $r \gg a$, giving $r' \approx r - a \sin \theta \cos \phi$, where r' is the distance from the observation point to the source element, gives an expression of the pressure for a baffled piston as [65, 67]

$$\mathbf{p}(r, \theta, t) = j\rho_0 c \frac{U_0}{\pi r} ka \exp j(\omega t - kr) \int_{-a}^a \exp jka \sin \theta \cos \phi \sin \phi dx \quad (2.13)$$

Converting dx to $d\phi$ by $x = a \cos \phi$ gives

$$\mathbf{p}(r, \theta, t) = j\rho_0 c \frac{U_0 a}{\pi r} ka \exp j(\omega t - kr) \int_0^\pi \exp jka \sin \theta \cos \phi \sin^2 \phi d\phi \quad (2.14)$$

The imaginary part of the integral vanishes by symmetry leaving the real part

$$\mathbf{p}(r, \theta, t) = j \frac{\rho_0 c}{2} U_0 \frac{a}{r} ka \exp j(\omega t - kr) \left[\frac{2J_1(ka \sin \theta)}{ka \sin \theta} \right] \quad (2.15)$$

where J_1 is a first order Bessel function. The beam pattern for a baffled piston source is modeled and shown in figure 2.4. The acoustic field on the beam axis, $\theta = 0$ is much simpler and can be described by [67]

$$p(r, 0) = 2\rho_0 c U_0 \left| \sin \left\{ \frac{1}{2} kr \left[\sqrt{1 + \left(\frac{a}{r}\right)^2} - 1 \right] \right\} \right| \quad (2.16)$$

This expression is particularly important in the photoacoustic experiments described in this chapter as the acoustic detector was placed as close to the axis of acoustic propagation as possible.

Broadband Sources

The previous derivations assumed a harmonic source as the fundamental building block of composite sources. In photoacoustic generation, however, the source, though retaining

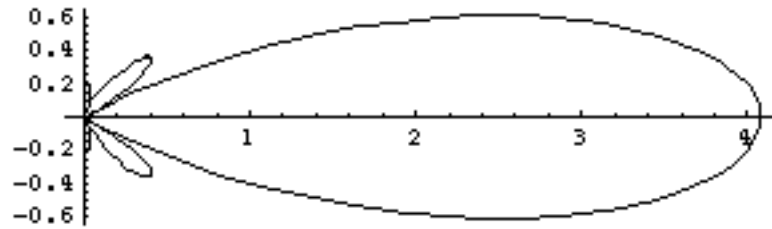


Figure 2.4: The calculated beam pattern for a baffled piston is shown here. The main lobe is surrounded by secondary lobes, predicted by the nodes inherent in the Bessel function that describes the pattern.

the geometry described above, is not a simple harmonic source with a single frequency, but a broadband source containing many frequencies up to the MHz range. The harmonic derivations are useful in that the broadband pulses may be derived by summing all frequencies up to the highest frequency generated by the optical absorption of the photoacoustic medium [64, 71]. The genesis of a pulse can be easily shown by a summation of sine functions.

$$W(t) = \sum_{n=1}^N (A_n \sin(n\omega t)) \quad (2.17)$$

where A_n are the Fourier coefficients and N is chosen appropriately to obtain the highest frequency contained in the pulse. An approximation of the limit of the frequency content of a photoacoustic pulse (figure 2.5) can be taken as the frequency obtained from the wavelength determined by the duration of the rising edge of the positive peak. Thus the maximum frequency can be approximated immediately from the acoustic pulse duration. The acoustic wave shape is exponential, so an arbitrary standard of $1/e$ is chosen to mark the pulse duration. In this case, the duration is approximately 50 ns, giving a frequency of about 20 MHz, $f = 1/(\text{pulseduration})$. The frequency content is shown in figure 2.6. The frequency content was obtained by looking at the power spectrum from an FFT algorithm. The content show frequencies up to about 50 MHz before the spectrum deteriorates into a random noise, although the content below 1% of the maximum content (at about 5 MHz) cuts off at about 30 MHz. As a simple rule, the $1/e$ pulse duration seems to predict the maximum frequency without having to employ FFT algorithms.

A sum of sines up to 20 MHz is shown in figure 2.7.

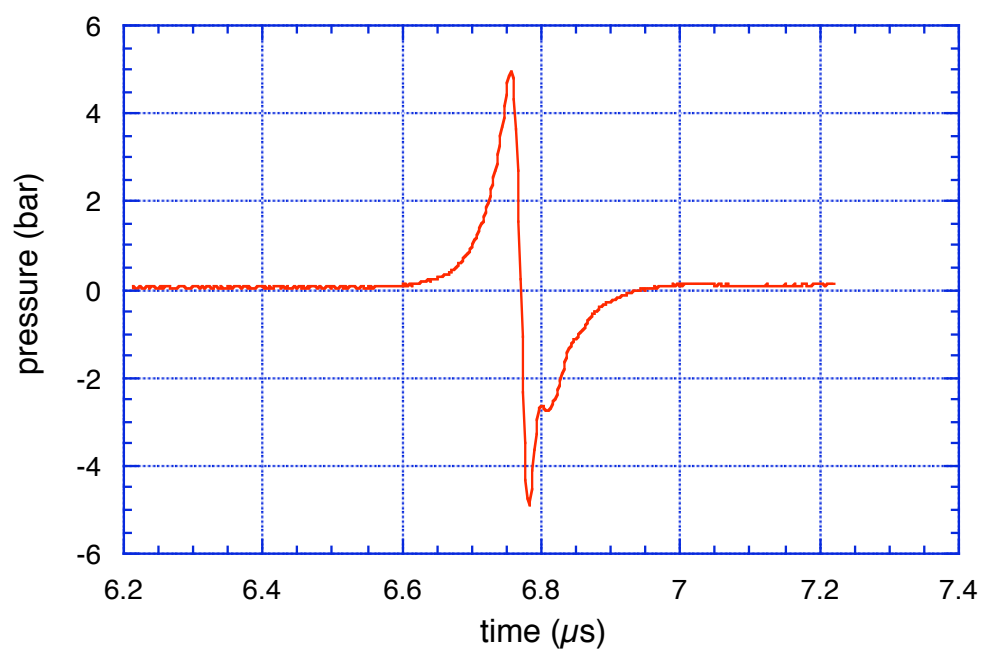


Figure 2.5: A photoacoustic pulse from a 5 mm laser spot incident on a 200 cm^{-1} absorbing solution. The frequency content is a sum of all frequencies below some high frequency limit, which may be determined by the duration of the positive peak.

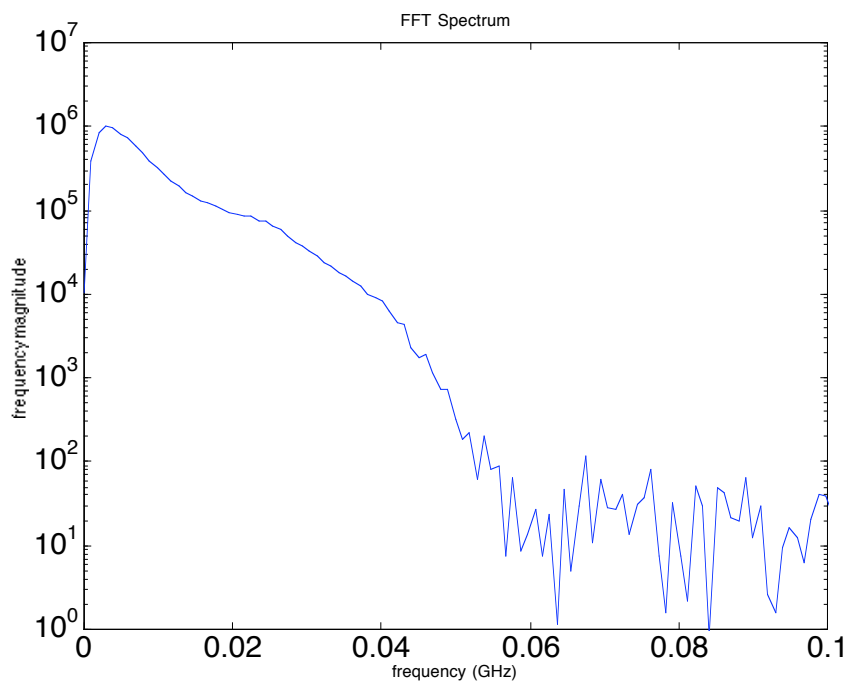


Figure 2.6: The frequency content of the pulse shown in figure 2.5. The frequency content extends to about 50 MHz, though at about 30 MHz the amplitude is 1% of the maximum amplitude, which occurs at about 3 or 4 MHz. This is close to the frequency maximum predicted by the $1/e$ duration of the original acoustic pulse, 50 ns, corresponding to a frequency of about 20 MHz.

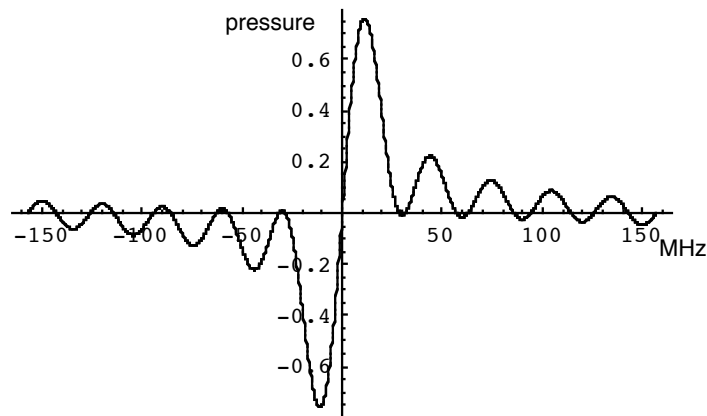


Figure 2.7: A reconstructed pressure pulse, made by summing frequencies to 20 MHz. Figure 2.5 was used to determine the limit of a finite sum of sinusoids. The resulting broadband pulse is shown here.

2.2 Materials and Methods

The attenuation and dispersion experiments in this chapter were conducted on the set up shown in figure 2.8. This set up was also used for a series of the diffraction experiments. A Q-switched, frequency doubled Nd:YAG laser operating at 532 nm with a pulse duration of 5 ns irradiated solutions made from Direct Red 81 dye (Sigma Chemical, St. Louis, MO) of various absorption coefficients. The Direct Red solutions were in an acrylic aquarium with an aluminum base. The 1×1 mm active area of a piezoelectric acoustic transducer was flush with the aluminum base and positioned in the center. The inside of the aquarium measured 113×113×150 mm (length×width×height). The absorption coefficients of the solutions used were 25, 50, 100, and 200 cm⁻¹ at 532 nm. The depths of the solutions were varied from about 4 mm to 4 cm. The minimum depth maintained at least 5 optical depths to protect the detector from direct optical damage from the laser. The Nd:YAG laser light was launched into a 1000 μm quartz optical fiber. The fiber was wound into a figure eight to create a uniform spot. The emitting fiber face was placed above the Direct Red solution surface to deliver a spot size of 5 mm in diameter. The fiber face was imaged onto the solution surface with a biconvex lens to make the uniform laser spot. As the depth of the solution was increased, the fiber was raised to ensure a constant spot size on the solution

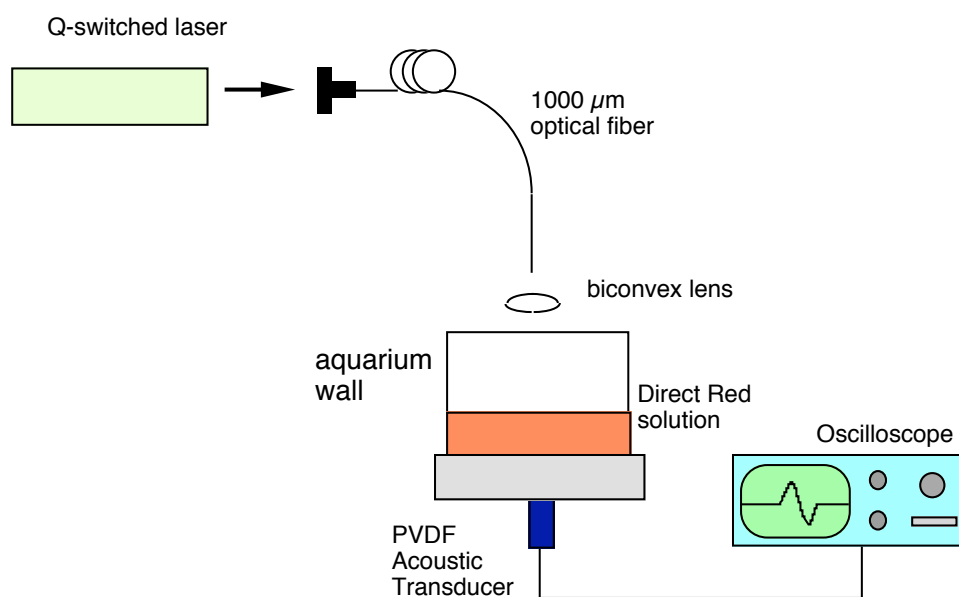


Figure 2.8: The set up for the broadband acoustic pulse propagation experiments. A Q-switched Nd:YAG laser irradiated Direct Red solutions of various depths and absorption coefficients. A PVDF acoustic transducer detected the waveforms in a transmission geometry. The detected waveforms were sent to a digitizing oscilloscope.

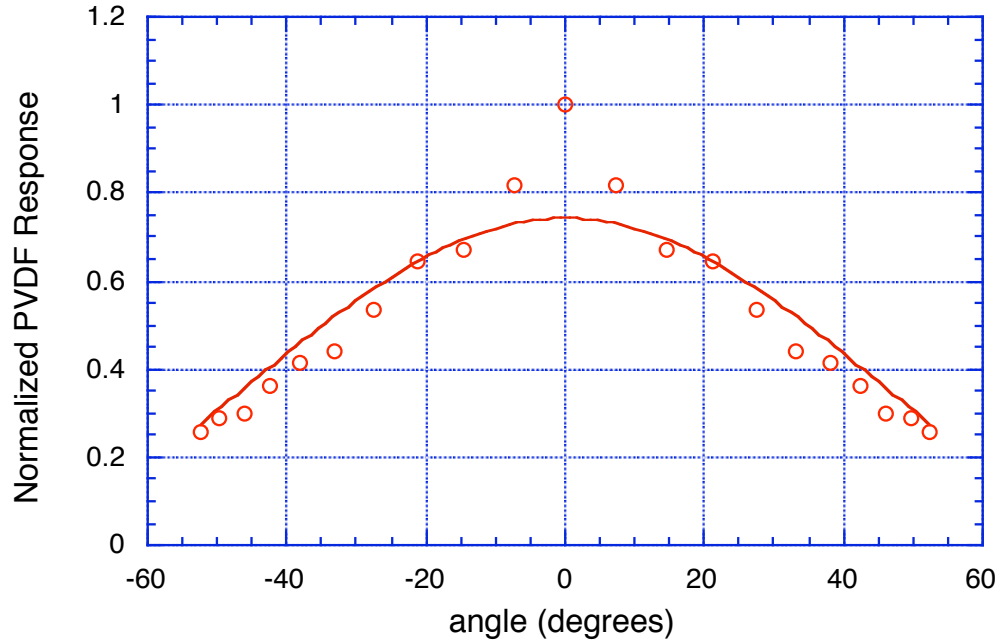


Figure 2.9: The antenna function of the PVDF transducer is shown as a function of angle. The amplitude is an average of two sets of measurements, The curve fit is a $\cos^2 \theta$ curve.

surface. The acoustic transducer was placed directly below the laser spot. The transducer was a piezoelectric detector with a 1×1 mm active area. The sensitivity was 5.5 mV/bar. The acoustic wave signal was sent to an oscilloscope (DSA 602A, Tektronix, Wilsonville, OR). The input impedance was $1 \text{ M}\Omega$, so that the charge signal from the PVDF film was integrated to a pressure signal.

2.2.1 Acoustic Transducer

The acoustic transducer used was a piezoelectric detector (KP-135, Ktech, Albuquerque, NM). The active area was a polyvinylidene fluoride (PVDF) film, with electrodes sputtered on either side of the film. The electrodes crossed to form a 1×1 mm active area. The sensitivity was measured using Direct Red solutions and was determined to be 5.5 mV/bar. The antenna function was measured as a function of angle and is shown in figure 2.9. The data was taken in two measurement sets, consisting of eleven angles each. The measurement sets had different maximum acoustic wave amplitudes, due to a small

inaccuracy in the transducer orientation between measurement sets, thus the amplitudes were all normalized to the maximum (value at $\theta = 0^\circ$). The angle of the detector was changed by translating a small photoacoustic source above the detector active area. This method was achieved by submerging a $400\ \mu\text{m}$ fiber into a $25\ \text{cm}^{-1}$ Direct Red solution, which has an absorption depth of $400\ \mu\text{m}$, thus approximating a small, spherical source. Initially, the source was placed directly above the detector, for an angular measurement of 0° . As the source was laterally translated, the angle increased, giving additional measurement points. The antenna function followed a $\cos^2\theta$ law, except at the center, where the amplitude rose to a sharp peak, probably due to the source being slightly piston-like, rather than being a pure spherical source.

2.2.2 Acoustic Attenuation

Acoustic attenuation was determined using the set up described above and increasing the solution depth, thus increasing the acoustic propagation distance from the laser irradiated disk to the acoustic detector face. The absorbing solutions were the 25, 50, 100, and $200\ \text{cm}^{-1}$ solutions described above. The dimensions of the aquarium were large enough so that any reflection from the boundaries were not detected within the $10\ \mu\text{s}$ window of the oscilloscope. Thus, the solution approximated a homogenous, semi-infinite acoustic medium.

2.2.3 Acoustic Dispersion

Acoustic waveforms were processed with MATLAB code to display the frequency content of the waveform. A Fast Fourier Transform (FFT) was used in the code. The frequency content of acoustic waves were analyzed from the $200\ \text{cm}^{-1}$ absorbing solution at 0.4–3.8 cm propagation distance. The $200\ \text{cm}^{-1}$ solution was chosen so that diffraction effects would be minimized, as a diffraction will also change the apparent frequency content of the acoustic wave. The frequency content of the acoustic waves were analyzed as a function of propagation distance, indicating if dispersion was significant in the 3.4 cm travelled.

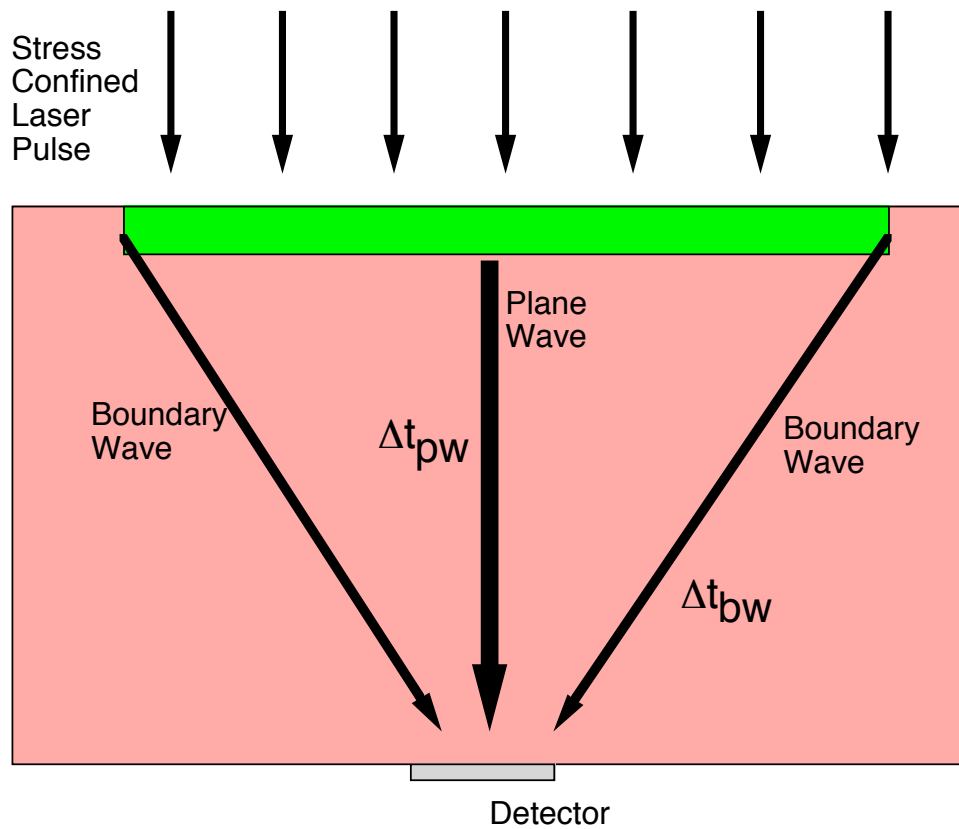


Figure 2.10: The relationship between the generation of the plane wave and the boundary wave from a disk of irradiation is shown here. The plane wave results from the circular spot, while the boundary wave arises from the band encircling the spot, the thickness of which is equal to the absorption depth.

2.2.4 Acoustic Diffraction

The acoustic diffraction experiments were performed with an optical detector of acoustic waves [27, 28]. This type of detector was used so that the active area, which was a focused spot from a HeNe laser ($60 \mu\text{m} \times 130 \mu\text{m}$), was small enough to discriminate between the plane wave and boundary wave from an irradiation of a planar, absorbing layer as shown in figure 2.10. The set up is shown in figure 2.11. A HeNe (Melles Griot, Carlsbad, CA) laser spot as 632 nm was focused to an elliptical spot with major and minor radii of $126 \mu\text{m}$ and $60 \mu\text{m}$, respectively. This spot was incident upon a right angle prism, where the beam was reflected to a 1 GHz photodiode (1601-AC-FS, New Focus,

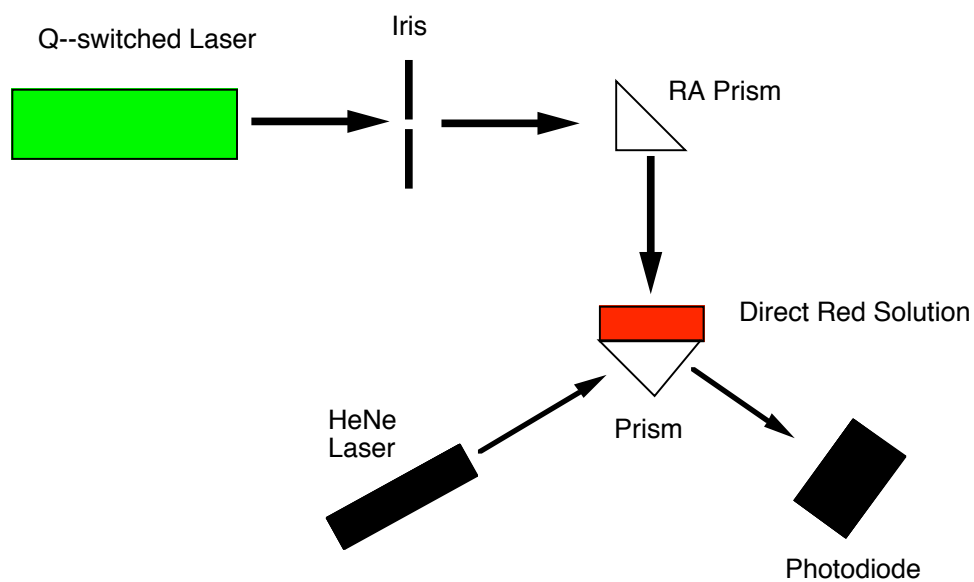


Figure 2.11: The set up for the diffraction experiment is shown here. The Q-switched laser discussed previously irradiated a 200 cm^{-1} solution. The beam diameter was determined by an iris diaphragm. The resulting acoustic waves were detected by an optical system using a HeNe laser and a fast photodiode.

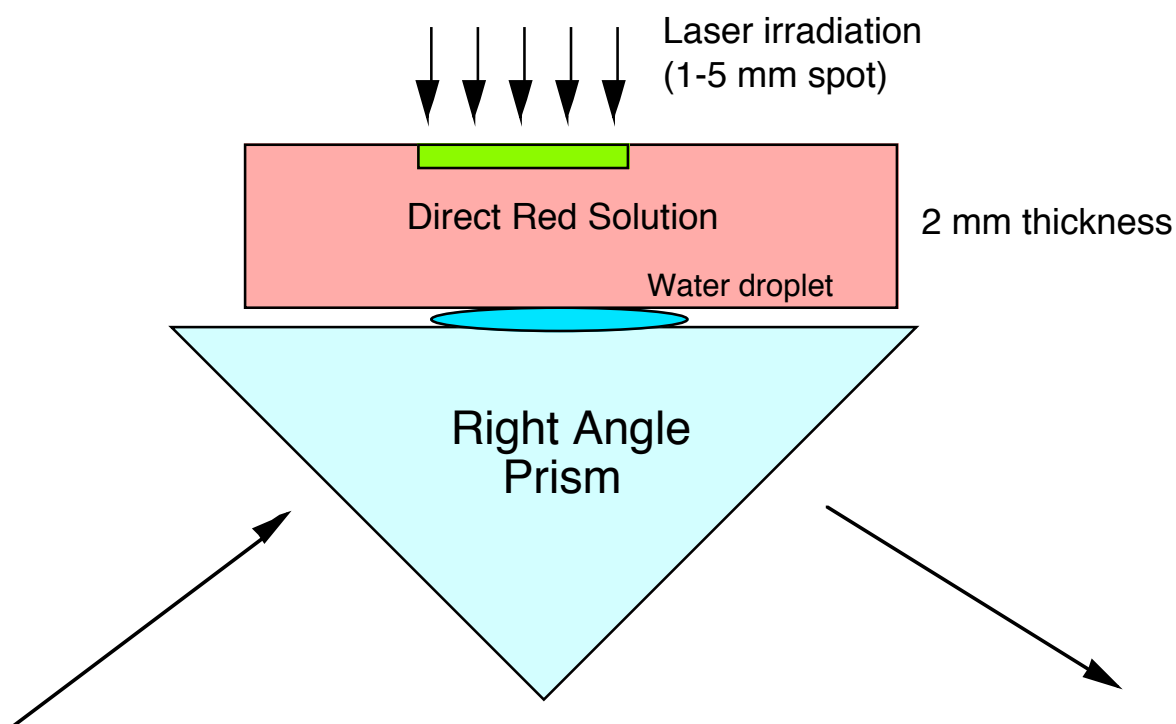


Figure 2.12: The optical detection set up relied on the change in optical index of refraction caused by a pressure wave incident on a water droplet on a prism. A focused HeNe beam was reflected from the water/glass interface and the beam was detected by the photodiode.

Santa Clara, CA) through a 632 nm notch filter. The photodiode had a gain of 700 V/A. A cuvette with 2.0 mm thick 200 cm^{-1} Direct Red solution was placed on the right angle prism. The Q-switched laser used in the attenuation and dispersion experiments was used to delivered stress confined pulses to the Direct Red solution. The laser energy was 8.3 mJ. The laser spot was varied from 1.1–5.0 mm with an iris diaphragm. The beam was then directed to the absorbing solution via a second right angle prism.

The optical detector is described in figure 2.12. The cuvette with the absorbing solution was placed on the water droplet, so that an acoustic wave generated in the solution would propagate into the water droplet and the compression waves would change the optical index of refraction of the water. This index change would alter the HeNe reflection and hence change the signal received at the photodiode. The signal was sent to the oscilloscope described above.

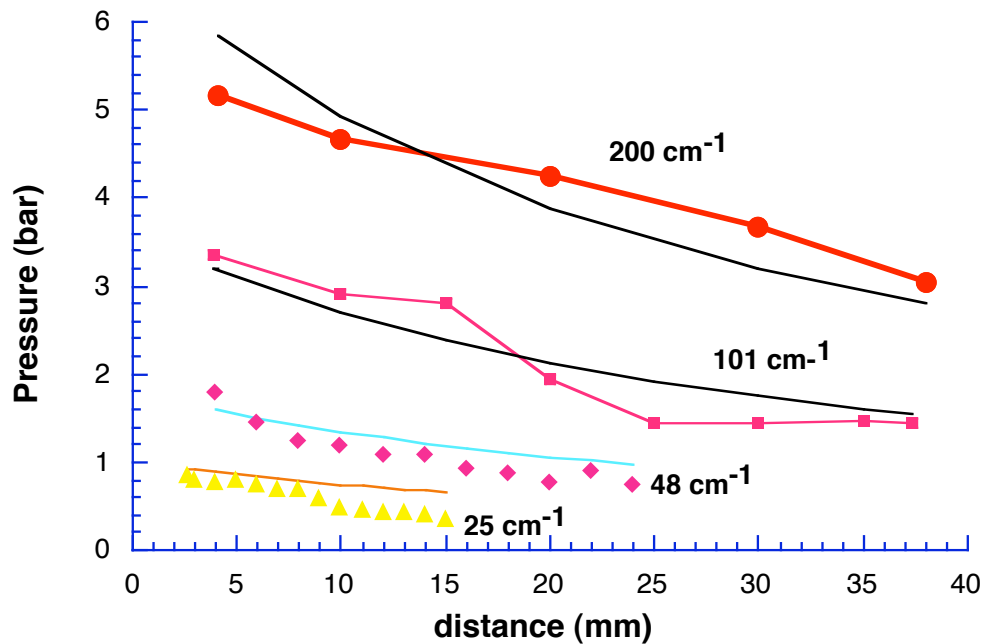


Figure 2.13: The acoustic attenuation is shown as a function of propagation distance and absorption coefficient. The experimental data is shown as discrete points, while the attenuation function fit, derived from equation 2.16, is shown as the continuous lines.

Acoustic diffraction is demonstrated by deformation of the bipolar acoustic waveform in the Direct Red solution. The disk of irradiation was changed from a flat disk to a fat cylinder as the spot changed from 5 mm in diameter to 1.1 mm. The absorption depth was $50\ \mu\text{m}$. For a near/far field boundary of 2.0 mm, equation 2.1 predicted a beam diameter of approximately 1 mm for a $200\ \text{cm}^{-1}$ absorption coefficient. Thus, the boundary wave was tracked in reference to the plane wave as the spot diameter was decreased from 5.0 to 1.1 mm.

2.3 Results

2.3.1 Acoustic Attenuation

The results of the acoustic attenuation experiments are shown graphically in figure 2.13.

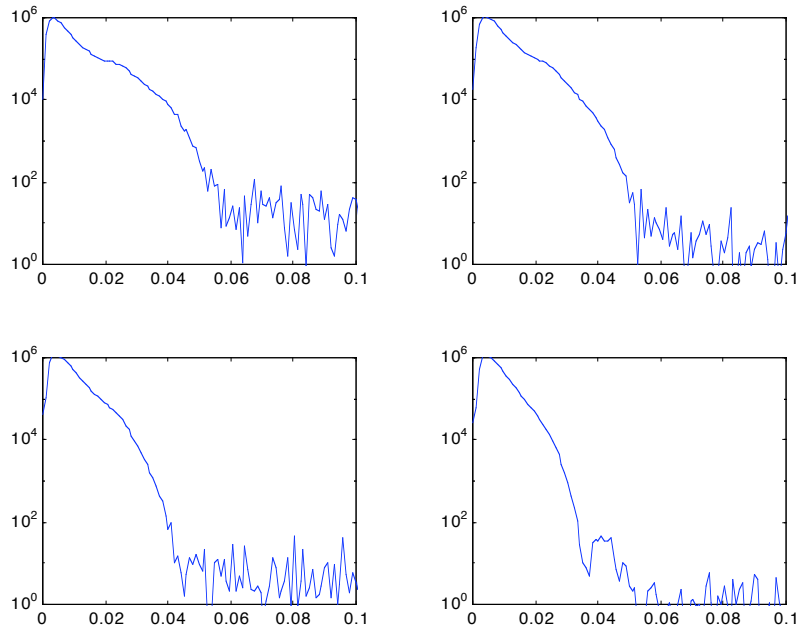


Figure 2.14: The frequency content of the acoustic waves generated from irradiating the 200 cm^{-1} solutions. The frequency content shows some dispersion at frequencies higher than 30 MHz, though for propagation distances less than 3 cm, dispersion is negligible.

2.3.2 Acoustic Dispersion

The results of the acoustic dispersion experiments are shown graphically in figure 2.14.

2.3.3 Acoustic Diffraction

The results of the acoustic diffraction experiments are shown graphically in figure 2.15.

2.4 Discussion

2.4.1 Acoustic Attenuation

The acoustic attenuation curves for the 25, 50, 100, and 200 cm^{-1} Direct Red solutions showed a decrease with constant slope. This is a departure for the attenuation for a

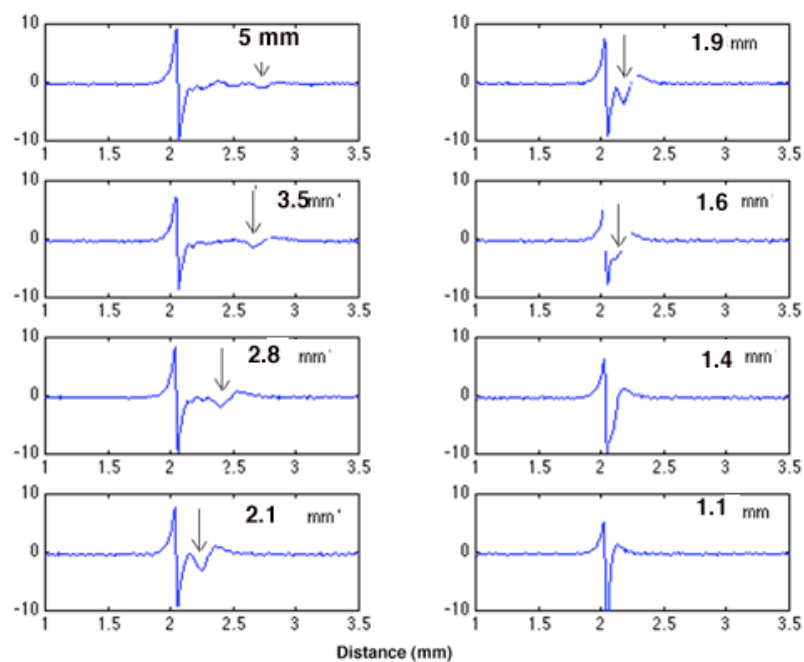


Figure 2.15: The acoustic diffraction is shown as a small boundary wave slowly merging with the larger plane wave. The predicted boundary wave position is indicated by a black arrow on each waveform. The boundary wave is shown approaching the plane wave as the spot diameter, indicated by the number in the upper right corner, is varied. The boundary wave has fully merged with the plane wave with a 1.4 mm spot.

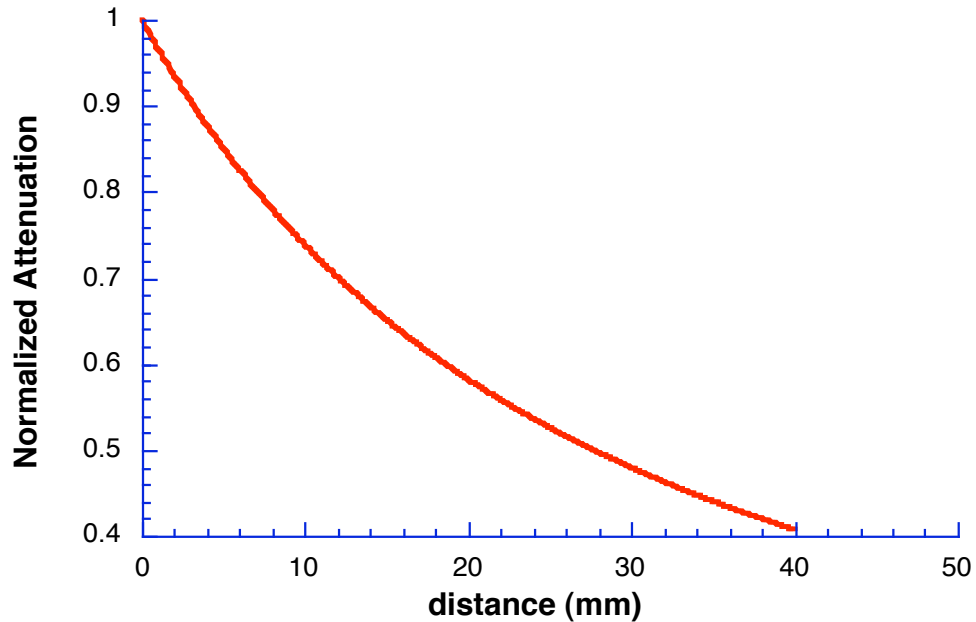


Figure 2.16: The attenuation predicted by equation 2.16. The far field shows attenuation of nearly constant slope, similar to the attenuation shown in the experiments. Equation 2.16 is not accurate for the near field.

spherical source, where the pressure would decrease as $1/r$. However, equation 2.16, has an attenuation shown by figure 2.16 The region after 3 mm shows attenuation of nearly constant slope, similar to the attenuation curves

2.4.2 Acoustic Dispersion

Acoustic dispersion was investigated using the 200 cm^{-1} solution. This absorption was chosen so that the resultant acoustic wave would be nearly entirely planar, with very little boundary component. The laser spot diameter was 5 mm and the absorption depth was $50\text{ }\mu\text{m}$, thus making the boundary component over two orders of magnitude smaller than the plane wave. With so little diffraction, the power spectrum over different propagation distances should have showed only dispersive effects. The graphs of the spectra show a peak at about 5 MHz with a magnitude of about 10^6 . For a two order of magnitude decrease, both the 4 and 10 mm propagation distances showed frequency content up to

40 MHz. For the 20 mm propagation distance, the frequency content was still over 30 MHz. With 40 mm of propagation, the frequency content narrowed to about 20 MHz. Thus, dispersive effects start to become noticeable at 20 mm, with appreciable dispersion of high frequencies (> 30 MHz) at 40 mm. As most measurements in this dissertation occur within 30 mm, dispersion is not a factor when considering propagation of the acoustic wave. In the case where acoustic propagation may occur at distances greater than 40 mm, such as the endoscopic photoacoustic probe of chapter 5, dispersive effects can be neglected, as earliest propagation arrival time is the measured quantity, which would be unaffected by dispersion.

2.4.3 Acoustic Diffraction

Acoustic diffraction is a more significant factor in acoustic wave propagation in this dissertation. Diffraction, as modeled in figure 2.10, occurs in the photoacoustic generation by a circular spot on a planar absorber when the boundary wave, from the circumferential ring, interferes with the plane wave, from the circular spot. Figure 2.15 showed the boundary wave merging with the plane wave.

2.4.4 Justification of Direct Red Solutions as Tissue Phantoms

The Direct Red solutions were used to model tissue as acoustic environments with respect to acoustic attenuation, dispersion, and diffraction. All of these are justified since the acoustic impedances are all very close in magnitude. In plane wave analysis, the acoustic impedance can be described as the product of density and sound speed, or

$$z_{ac} = \rho_0 c \quad (2.18)$$

where z_{ac} is the acoustic impedance, ρ_0 is the density, and c is the sound speed in the medium. The relation of attenuation to impedance is an inverse one, as the acoustic intensity is related to impedance by the equation

$$I = \frac{p^2}{\rho_0 c} \quad (2.19)$$

where I is the acoustic intensity and p is the pressure. Thus, attenuation and dispersion (wavelength dependent attenuation) are related to acoustic impedance. Diffraction is

Table 2.1: Sound speed, densities, and acoustic impedances for various tissues and water, acrylamide gel, and mineral oil. All tissue impedances are within 10% of 1.5 g/cm²-s, except bone, which has a value of 6.4 g/cm²-s. Acrylamide gel is within 7% and water is within 2% of the value. Mineral oil has a much lower acoustic impedance, 1.15 g/cm²-s, mostly primarily due to its low density. Its usefulness as a phantom comes from its immiscibility with water and its optical clarity.

Acoustic medium	sound speed(10 ⁵ cm/s)	density(g/cm ³)	impedance (g/cm ² -s)
water	1.00	1.48	1.48
acrylamide (gelled)	1.05	1.52	1.60
mineral oil	0.83	1.38	1.15
bone	3.2	2.0	6.4
fat	1.47	.92	1.35
skeletal muscle	1.56	1.04	1.62
premenstrual breast	1.52	.92	1.40
fetal skin	1.54	1.11	1.70
spleen	1.55	1.05	1.63
milk	1.53	1.03	1.58
normal saline (37°C)	1.55	1.0	1.55
eye, vitreous	1.52	1.01	1.54
CSF	1.51	1.01	1.52
bovine blood vessel	1.57	1.07	1.68
whole blood (37°C)	1.53	1.05	1.61

modeled here geometrically, making the propagation model independent of tissue type, so long as the impedances, and hence propagation, are the same. Table 2.1 shows the densities and sound speeds of several tissues and water from Duck [70], Wells [72], Geleskie *et al* [73], and Mol *et al* [74]. The impedance values for the tissues, excepting bone, in table 2.1 are all within about 10% of a value of 1.5 g/cm²-s. Even though there may be a good contrast between tissues, the impedance values are all close, thus the acoustic propagation, with respect to attenuation, diffraction, and dispersion, should be similar. The value for bone, 6.4 g/cm²-s, being four times higher than tissue, may prove to be a useful measure to discriminate bone interfaces within tissue. The density for bone given here is not for whole bone, which includes marrow. The density given in this table is for the hard part of the bone, which is what would provide the acoustic interface with softer tissue. Thus, it may be possible to perform high resolution, small scale bone imaging because of the high acoustic contrast. Water and acrylamide gels fall within the range of

values for these tissues, making them excellent phantoms. Mineral oil has a much lower acoustic impedance, primarily due to its low density. Its usefulness as a tissue phantom comes from its optical clarity, when clarity is needed, and due to its immiscibility with water, allowing the experimenter to make layered media between water and oil, while still remaining within 25% of the respective acoustic impedances.

Chapter 3

Depth profiling of absorbing soft materials using photoacoustic methods

*

3.1 Introduction

Acoustic waves can be generated in optically absorbing materials by rapidly depositing laser energy into the material. The waves can then be detected with an acoustic transducer. In media with layers of different absorbing properties, an analysis of the acoustic wave can reveal the boundaries of the layers as well as the absorption properties of the layers themselves. Using a laser and a piezoelectric transducer, this chapter takes the acoustic wave data and applies it to a numerical algorithm in order to characterize layered media with respect to absorption coefficient.

Light propagation in biological media is determined by optical absorption and scattering as described by the radiative transport equation. Typical attenuation depths may be less than 1 mm. Acoustic waves propagate deep into turbid tissue before signal degradation from attenuation and diffraction effects take place. Near field models for acoustic wave propagation using plane waves provide simple, accurate analysis of pressure waves within the first few centimeters depending on the geometry of the initial pressure distribution. Far field models using the acoustic wave equation predict acoustic fields beyond the range afforded by plane wave theory.

*This chapter was originally published in the IEEE Journal of Selected Topics in Quantum Electronics, *Lasers in Medicine and Biology*, July/August 1999, Vol 5, No. 4.

Optically induced acoustic phenomena have been studied extensively and used to derive information about optical and acoustic properties of materials. An excellent account of the theory and experimental processes of optically induced acoustic waves in liquids and gases can be found in Sigrist [7]. More recently, acoustic waves have been generated in biological media and phantoms for the purpose of deriving their optical properties. Kruger [75] used a Xenon flashlamp with a $1\ \mu\text{s}$ pulse duration to excite acoustic pulses in a scattering medium. Oraevsky *et al.* [24, 25] used a lithium niobate piezoelectric transducer to perform time-resolved stress detection on pressure waves induced by a Q-switched Nd:YAG laser operating at 335 nm, 532 nm and 1064 nm. The targets were both purely absorbing and turbid media. They also displayed an acoustic profile of a two layer collagen gel, where a two peaked waveform was generated indicating the two regions of differing absorption coefficients. Paltauf *et al.* [27] introduced a method of detecting acoustic waves generated by irradiating an absorbing dye solution with a Q-switched Nd:YAG laser at 532 nm. They used a novel optical transducer based on pressure induced reflectivity changes on a glass-water interface and a continuous probe beam. Their scheme minimized the signal distortion due to acoustic diffraction and they successfully derived the absorption coefficient of the dye solution. Viator *et al.* [76] attempted to derive the absorption coefficient as a function of depth in Indocyanine Green (ICG) stained elastin biomaterial. Characterization of the stain depth profile was important to tissue welding applications, as the ICG absorption of laser irradiation determines the temperature change of the biomaterial. This temperature change is an important parameter in laser-tissue welding. They used a numerical algorithm applied to data from the acoustic wave induced by irradiation from a Q-switched Nd:YAG laser coupled to an optical parametric oscillator tuned to 800 nm.

This chapter used India ink as a photostable absorber in water solutions and acrylamide gels. We also used India ink to stain elastin biomaterials. Layered absorbing media were constructed out of acrylamide gel and spatial discrimination between layers was shown for a $70\ \mu\text{m}$ separation. A numerical algorithm for determining the absorption coefficient as a function of depth was derived and applied to the layered gels and to the stained elastin biomaterial.

3.1.1 Acoustic Wave Theory

Acoustic waves can be generated by light through various mechanisms, including radiation pressure, material ablation, and dielectric breakdown [7]. This chapter studies acoustic generation in an absorbing medium by a thermoelastic process, whereby light is absorbed in a stress confined manner resulting in rapid expansion that manifests as a pressure wave. Stress confinement is a condition where optical energy is deposited before the energy can propagate away acoustically. This effect is also referred to as acoustic confinement. The condition of stress confinement can be described by the equation,

$$\tau = \frac{\delta}{c_s} \quad (3.1)$$

where δ is the absorption depth and c_s is the speed of sound in the medium. If the pulse width of a laser is less than τ , the pulse is considered stress confined. Thus, a stress confined laser pulse will create a pressure wave in an absorbing sample the profile of which is commensurate with the initial optical energy deposition.

If μ_a is the absorption coefficient of the medium, the initial pressure distribution can be described as

$$p_0(z) = \mu_a \Gamma H_0 \exp(-\mu_a z) \quad (3.2)$$

where Γ is the unitless Grüneisen coefficient. The value $\Gamma = 0.12$ was used in this chapter [77]. The Grüneisen coefficient describes the fraction of optical energy that is translated into thermoelastic expansion. The depth in the medium is given by z . H_0 is the incident laser radiant exposure. This pressure wave, considered as a plane wave with propagation in one dimension, will divide into two waves that travel forward and backward along the laser beam axis. The waves have equal amplitudes. With an air/medium interface, there is an acoustic mismatch that causes a delayed, reflected tensile wave from the surface. This tensile wave is shown graphically in the top half of figure 3.1 as a negative peak, B. If the boundary is matched with respect to acoustic impedance the tensile wave will be eliminated. The bottom of figure 3.1 shows a delayed tensile wave created by placing an optically clear, but acoustically matched layer on the irradiated surface. The matched layer was $150 \mu\text{m}$, thus the wave traveled an additional $300 \mu\text{m}$ before being reflected.

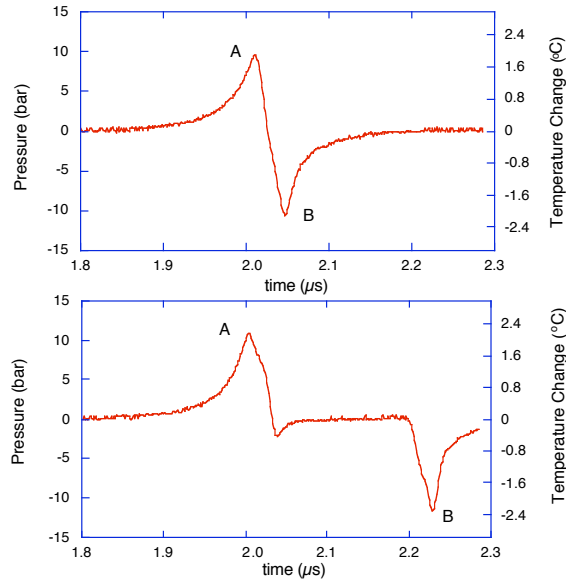


Figure 3.1: (top) An acoustic wave generated by irradiating a 160 cm^{-1} acrylamide gel. The negative wave (B) following the positive wave (A) is a reflected tensile wave resulting from the acoustic mismatch of the acrylamide/air boundary. (bottom) The tensile wave was delayed by placing a clear acrylamide sheet before the absorbing acrylamide.

That additional $300\text{ }\mu\text{m}$ is shown in the bottom half of figure 3.1 as a 200 ns delay. With a sound speed of $1.5\text{ mm}/\mu\text{s}$, this delay corresponds to the extra $300\text{ }\mu\text{m}$ of travel.

For the acoustic wave shown in figure 3.1, the leading edge of the positive peak, A, is the region containing the absorption information of the medium. Graphically, it is the part of the acoustic wave from $1.8\text{--}2.0\text{ }\mu\text{s}$. The peak indicates the acoustic wave amplitude initially induced by the laser pulse at the surface of the medium. The surface peak was detected $2.0\text{ }\mu\text{s}$ after the laser pulse, since it had to travel through the intervening gel to the transducer. As illustrated in the figure, the amount of light absorbed versus depth decreases exponentially according to Beer's Law. Converting the time axis to depth in tissue by using a sound speed, c_s of $1.5\text{ mm}/\mu\text{s}$ and the relation $z = (t_{\text{peak}} - t)c_s$, where t_{peak} is the time of the surface peak and t is time, the result is the representation as shown in figure 3.2. The exponential curve fit of this acoustic wave contains the absorption coefficient in the exponent,

$$p(z) = 9.5 \exp(-185z) \quad (3.3)$$

where $p(z)$ is the pressure at depth z in centimeters. This gives an absorption coefficient of

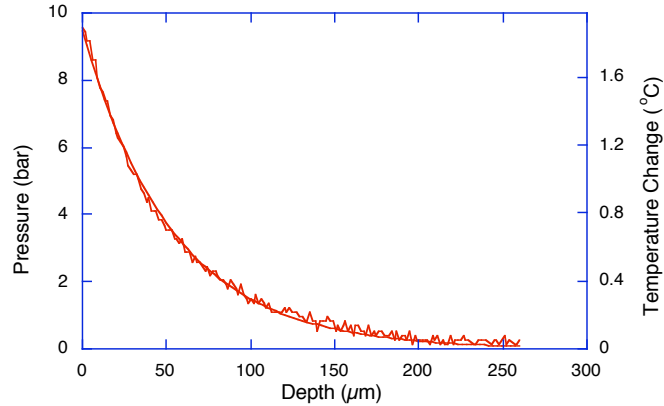


Figure 3.2: The absorption information of the acoustic wave is shown here as pressure and temperature as a function of depth for a 180 cm^{-1} gel.

185 cm^{-1} from the fit, where the measured absorption coefficient from a spectrophotometer was 180 cm^{-1} .

As stated before, two acoustic waves are generated, one traveling into the medium. The other travels in the opposite direction. This plane wave analysis is appropriate in the near field [7] where the near field/far field boundary is determined to be

$$z_d = \frac{d^2 \mu_a}{8} \quad (3.4)$$

where z_d is the boundary, d is the laser beam diameter, and μ_a is the absorption coefficient. With the geometry considered in this paper, a laser beam irradiates a medium with a circular spot with an absorption depth of δ .

A relationship between pressure and temperature rise can be described by

$$T = \frac{P}{\rho C T} \quad (3.5)$$

where P is pressure [J/cm^3], ρ is the density [g/cm^3], C is the specific heat [$\text{J}/\text{g}^\circ\text{C}$]. Additionally, the relation

$$10 \text{ bar} = 1 \text{ J}/\text{cm}^3 \quad (3.6)$$

should be used to convert pressures in bars to pressure as energy density.

When considering the theory noted above, it is clear that a plane wave analysis of acoustic waves detected in the near field can offer information about the initial temperature

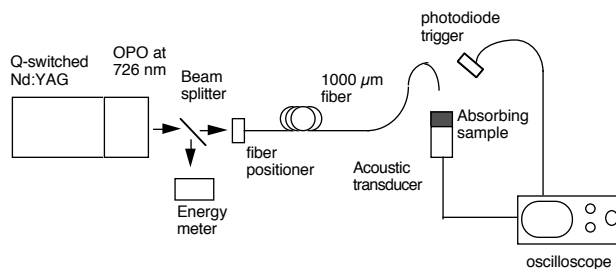


Figure 3.3: The set up for the acoustic wave generation in the absorbing sample.

and pressure in absorbing media. While the previous discussion on acoustic wave theory considers a homogeneous absorber, the theory can be easily adapted to account for layered absorbing media.

3.2 Materials and Methods

3.2.1 Photoacoustic Set Up

The photoacoustic set up used a Q-switched, frequency doubled Nd:YAG laser (Quantel Brilliant) operating at 532 nm coupled to an optical parametric oscillator (OPOTEK) tuned to 726 nm (figure 3.3). The laser beam was directed to a beamsplitter so that pulse to pulse variations could be monitored. The laser beam was focused into a 1000 μm quartz optical fiber. The output of the fiber was a circular, azimuthally symmetric beam profile. The laser spot sizes were in the range of 3–5 mm in diameter. Laser radiant exposure was in the range of 0.8–1.2 J/cm^2 . The fiber was positioned above the acoustic transducer. Samples were placed between the fiber and the transducer face while proper acoustic coupling was ensured between the sample and the transducer. The output of the transducer was sent to a digitizing signal analyzer (DSA 602A, Tektronix). The data was then stored and analyzed using a Macintosh PowerPC (Apple Computer).

3.2.2 India Ink Solution

An absorbing solution was used in these experiments to calibrate the sensitivity of the acoustic transducer in mV/bar . India ink (Black ink #723, Eberhard Faber) with an absorption coefficient of 2650 cm^{-1} at 726 nm was used to make absorbing solutions in

deionized water in the range of 30 to 188 cm^{-1} . The absorption coefficients of the solutions were measured with a spectrophotometer (HP 8452A Diode Array Spectrophotometer) by measuring the absorbance of a known thickness of solution. The absorption spectrum slightly decreased with increasing wavelength. The spectrum was without peaks and varied by only 10% over a 50 nm range about 726 nm. The ink solutions were poured into a container attached to the acoustic transducer so that the solution was in direct contact with the quartz window of the transducer, maintaining proper acoustic coupling between the solution and the sensor. We ensured at least four optical depths between the surface and the transducer face to protect the sensing element from optical damage.

3.2.3 Acrylamide Gel

Acrylamide gels were used to create layers of absorbers with constant absorption coefficients. The use of acrylamide allowed the formation of strong sheets of gel as thin as 70 μm . These sheets were then used in acoustic propagation experiments either singly or in layered combinations.

The acrylamide was made according to the procedure outlined by Sathyam *et al.* [78]. 9.735 g of acrylamide and 0.265 g of bis-acrylamide (Sigma Chemical) were dissolved in 50 ml of deionized water to form a 20% polyacrylamide gel. The acrylamide solution was filtered and degassed prior to polymerization to remove contaminants and prevent air bubbles from forming in the gel. Polymerization was induced by adding an initiator of 0.02 g of ammonium persulfate and 0.2 ml of TEMED (Sigma Chemical). Most preparations included adding India ink to the acrylamide solution in order to give the gel an absorption spectrum. For higher concentrations of ink, the amount of initiator had to be increased in order for the acrylamide to polymerize. As with the India ink solutions, the absorption coefficient of the gels was measured with a spectrophotometer.

3.2.4 Elastin Biomaterial

Elastin biomaterial was formed from the elastin component of an aorta as described by Crissman *et al.* [79]. In these experiments the elastin biomaterial was derived from porcine aorta harvested from domestic swine. The aorta was cleaned and placed in a

500 mM sodium hydroxide solution at 65°C. The vessels were sonicated for 60 minutes. The vessels were then rinsed in deionized water. This process resulted in the removal of all constituents of the artery except for the elastin layer. The thickness of the tissue was measured with a micrometer and was approximately 1 mm. The biomaterial was cut open so that a flat, rectangular piece could be positioned in the path of the laser beam. The intimal surface was stained by brushing an India ink solution with absorption coefficient of 78 cm^{-1} at 726 nm onto the biomaterial. The solution was allowed to soak into the biomaterial for 5 minutes. The excess solution was removed. The opposite surface was in contact with a piezoelectric transducer.

3.2.5 Acoustic Transducer

The acoustic transducer was a piezoelectric sensor (Science Brothers, WAT-13) with a lithium niobate crystal used for detecting acoustic pulses of nanosecond duration. The sensing element is protected by a quartz window. The transducer delay was 800 ns. The transducer delay was determined during the sound speed experiment described below.

The transducer sensitivity was determined by creating a calibration curve using known concentrations of India ink in solution. The known absorption coefficients were determined with a spectrophotometer as described above. The absorption coefficient of the solution was used to predict the acoustic wave peak amplitude in accordance with equation 2 with a factor of 0.5 included to account for the bipolar waveform. The resultant data was reconciled with the predicted values, thus giving a calibration factor in mV/bar. The ink solutions, being uniformly absorbing, were also verified for absorption coefficient by analyzing the acoustic wave shape and fitting it to an exponential curve in accordance with a Beer's Law model of absorption.

3.2.6 Sound Speed Measurement in Acrylamide

Acrylamide sheets of $950 \mu\text{m}$ thickness were produced with India ink as an absorber. The thickness was measured with a feeler gauge on the gel mold and measured again directly with a digital micrometer. The absorption coefficient was measured by a spectrophotometer to be 87 cm^{-1} . First, a single layer was placed on the face of the transducer

and irradiated with the laser, resulting in an acoustic wave. The transit time of the acoustic wave from its inception to its detection at the transducer was recorded by the digitizing signal analyzer. This measurement was repeated with a second 950 μm layer placed over the first layer. These measurements were repeated for a third and fourth layer. By measuring the incremental travel time and the extra thickness of gel, the sound speed in acrylamide was calculated. The transducer delay was also determined by this method.

3.2.7 Discrimination of Layered Acrylamide

Acrylamide sheets of varying thickness were made. Sheets with ink absorber were made at 950 μm and 160 μm thickness. The sheets had an absorption coefficient of 140 cm^{-1} . Clear sheets were made of 950 μm , 100 μm , and 70 μm thickness. The clear sheets were placed between the absorbing sheets so that no light would be absorbed, hence no acoustic wave would be generated from this layer. The 160 μm layer allowed approximately 10% of the light to pass through to the 950 μm layer when the layers were placed in the arrangement shown in figure 3.4.

3.2.8 Acoustic Wave Generation

Samples of acrylamide gel sheets of 950 μm were formed with absorption coefficients of 30, 43, 67, 117, 147, and 188 cm^{-1} . Each sample was placed on the acoustic transducer and irradiated with the laser to produce an acoustic wave. A minimum of 3 optical depths was ensured between the gel surface and the transducer to protect the sensing element from optical energy.

3.2.9 Absorption Algorithm

The graphic representation of the acoustic wave as shown in figure 3.1 and figure 3.2 directly show the pressure and temperature relative to the depth in the tissue. The variation in absorption coefficient, however, is implicit. In media where scattering is negligible ($\mu_a \gg \mu_s$), Beer's Law can represent the attenuation of light in the tissue optics. To calculate the intrinsic absorption as a function of depth, an algorithm was developed using a simple model based on a highly absorbing medium.

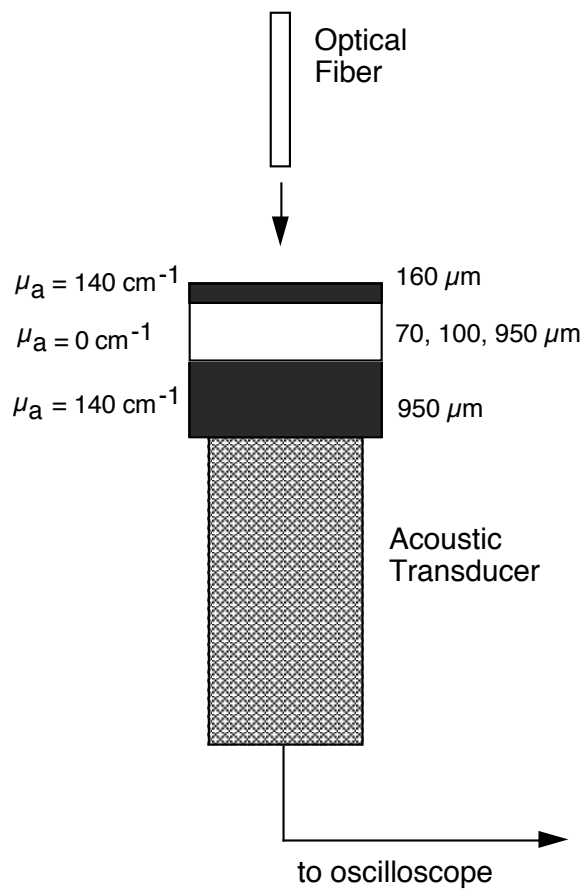


Figure 3.4: The absorbing layer discrimination experimental arrangement. The two absorbing gel layers were separated by a clear, non-absorbing layer.

For a uniformly absorbing medium, one where the absorption coefficient is constant, the energy A_1 absorbed per unit area in a layer of thickness Δx_1 is

$$A_1 = H_0(1 - \exp(-\mu_a \Delta x_1)) \quad (3.7)$$

where H_0 is the radiant exposure of the laser pulse and μ_a is the absorption coefficient of the medium. For a two layered medium, the energy absorbed per unit area in the second layer of thickness Δx_2 is reduced by the amount of energy absorbed in passing through the first layer,

$$A_2 = H_0(1 - \exp(-\mu_{a2} \Delta x_2)) \exp(-\mu_{a1} \Delta x_1) \quad (3.8)$$

Extending this to a multi-layer case of constant layer thicknesses, the energy per unit area absorbed in the n^{th} layer is

$$A_n = H_0(1 - \exp(-\mu_{an} \Delta x)) \exp\left(-\sum_{i=1}^{n-1} \mu_{ai} \Delta x\right) \quad (3.9)$$

Since the equation (3.9) is expressed in terms of energy per unit area, the relationship $P_n = \Gamma A_n / \Delta x$ may be used to obtain the pressures that propagate in each direction,

$$P_n = \frac{\Gamma H_0}{2\Delta x} (1 - \exp(-\mu_{an} \Delta x)) \exp\left(-\sum_{i=1}^{n-1} \mu_{ai} \Delta x\right) \quad (3.10)$$

(The factor of two arises because half the energy propagates in each direction along the axis of the laser beam.) Note that if the radiant exposure is given in J/cm^2 and the layer thickness is in cm , then equation (3.10) will generate pressures with units of J/cm^3 . To obtain pressures in bars, then equation (3.6) should be used.

An equation for the absorption coefficient of each layer can be derived from equation (3.10).

$$\mu_{an} = -\frac{1}{\Delta x} \ln \left(1 - \frac{2\Delta x P_n}{\Gamma H_0} \exp\left(\sum_{i=1}^{n-1} \mu_{ai} \Delta x\right) \right) \quad (3.11)$$

Again, the pressure P should be in J/cm^3 , the layer thickness Δx should be in centimeters, and the radiant exposure H_0 should be in J/cm^2 . If the target material is divided into layers corresponding to the resolution of the waveform on the digitizing signal analyzer, the absorption coefficient can be derived for each of these layers using the algorithm described

above. The absorption coefficients are obtained with increasing depths, starting with the first layer and propagating downwards into the sample.

In all numerical simulations and experiments, a running average of the data was done with a 9 element width.

As a first test of the algorithm, MATLAB code was written to simulate acoustic waves. Simulations were run with and without random noise. The random noise was added as a percentage of the maximum acoustic wave amplitude. The acoustic waves were simulated for media of constant absorption coefficient. These simulated acoustic waves were then analyzed with the absorption coefficient algorithm. Additional code was written to create a smoothed acoustic wave from the noisy simulations.

Next, data from absorbing acrylamide sheets were analyzed with the absorption algorithm. Additionally, acoustic wave data from two 140 cm^{-1} acrylamide sheets separated by a clear layer were analyzed. Finally, data from an acoustic wave from an elastin bio-material stained with ink was analyzed.

3.3 Results

3.3.1 Transducer Calibration

The calibration factor for the acoustic transducer was $1.05 \pm 0.10\text{mV}/\text{bar}$. The correlation between acoustic wave exponential fit and spectrophotometer is shown in figure 3.5. The curve is linear and is approximated by the polynomial

$$y = 1.02x - 0.4 \tag{3.12}$$

The slope near unity indicates agreement between the spectrophotometer and the acoustic wave exponential fits.

3.3.2 Sound Speed in Acrylamide

The sound speed in the acrylamide was determined to be $1.52 \pm 0.01\text{ mm}/\mu\text{s}$. The transducer delay was determined from these measurements to be 800 ns.

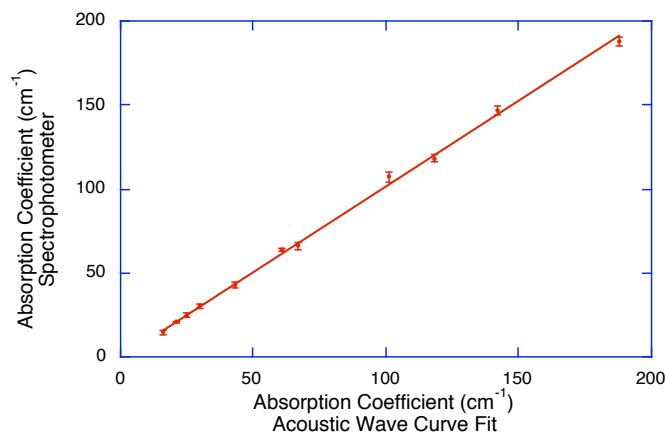


Figure 3.5: The measured absorption coefficient of the India ink solutions for the spectrophotometer and the acoustic wave exponential curve fit. The linear nature of the curve indicates agreement between the two measurement methods.

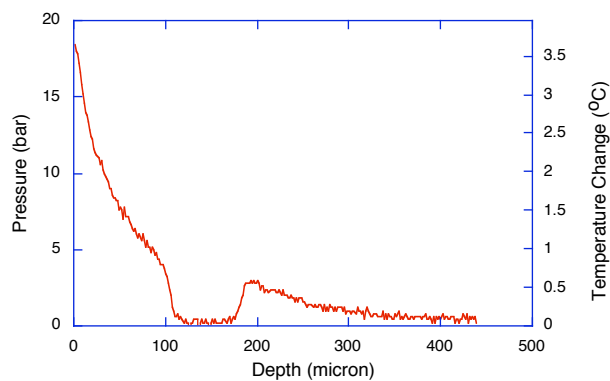


Figure 3.6: Acoustic wave generated in two absorbing gel layers (140 cm^{-1} separated by $70\text{ }\mu\text{m}$ of clear gel. The clear layer is represented by the region of near zero pressure.

3.3.3 Gel Layer Resolution

The acoustic wave discriminated two layers of absorbing gel separated by $70\text{ }\mu\text{m}$ of clear gel as shown in figure 3.6. The clear gel is indicated by the region of near zero pressure.

3.3.4 Computer Simulations

Acoustic waves were simulated as the pressure induced in 30, 43, 67, 117, 147, and 188 cm^{-1} gel of $1000\text{ }\mu\text{m}$ thickness. These values were chosen to match the experimental

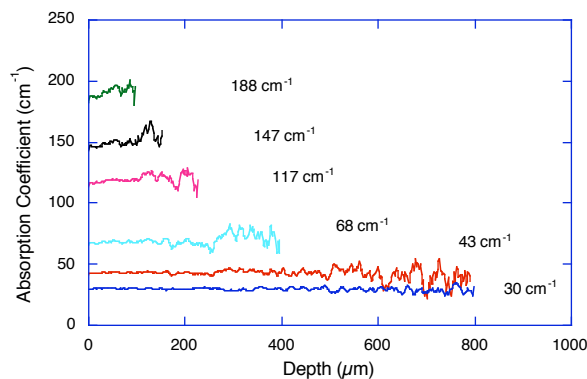


Figure 3.7: The result of running the absorption algorithm on the simulated acoustic waves with the 5% noise level.

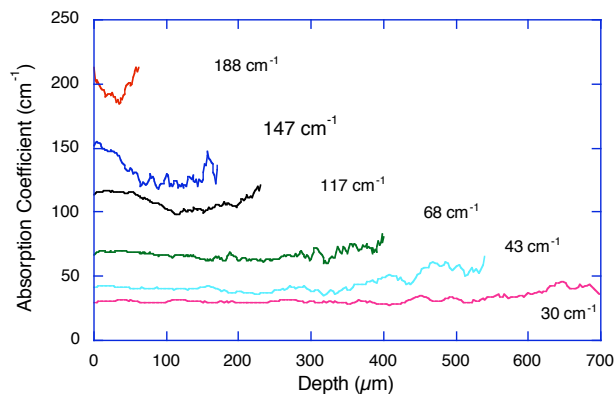


Figure 3.8: The result of running the absorption algorithm on the acoustic waves generated in the various acrylamide gels with the indicated absorption coefficients.

data. Random noise was added to the 5% level. The waveform was then applied to the absorption algorithm. The result is shown in figure 3.7.

3.3.5 Gel Absorption Coefficient

The acoustic waves were generated in the acrylamide gels. The gel data were applied to the absorption algorithm. The results are shown graphically in figure 3.8.

The data for the layered gel was applied to the absorption algorithm and the result is shown in figure 3.9.

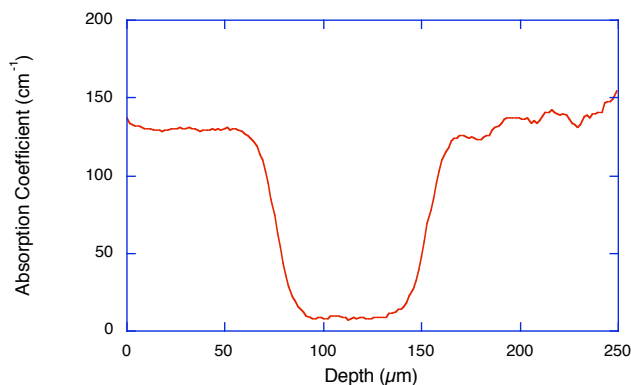


Figure 3.9: The absorption coefficient of the layered acrylamide gel of figure 3.8.

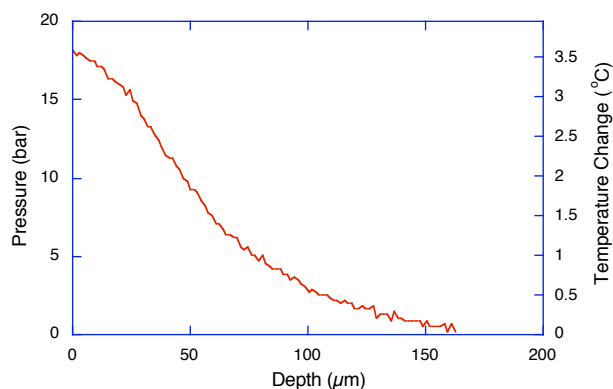


Figure 3.10: The acoustic wave generated in the ink stained elastin biomaterial.

3.3.6 Elastin Biomaterial

The acoustic wave generated in the ink stained elastin biomaterial is shown in figure 3.10. The data from the biomaterial was applied to the absorption algorithm. The result is shown in figure 3.11.

3.4 Discussion

3.4.1 Gel Layer Resolution

Figure 3.6 shows two distinct regions of induced pressure. The regions clearly correspond to the absorbing acrylamide sheets separated by the $70\ \mu\text{m}$ clear sheet. This depth discrimination was expected and was limited by transducer rise time and data sampling

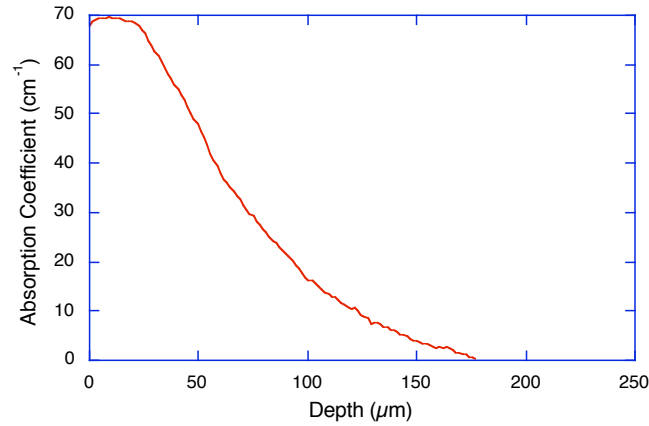


Figure 3.11: The absorption coefficient of the ink stained elastin biomaterial as a function of depth. The ink concentration is highest at the surface and drops with depth.

rate. The 1 GHz sampling of the signal analyzer allowed for $1.5 \mu\text{m}$ resolution for acoustic waves with sound speed of $1.5 \text{ mm}/\mu\text{s}$. On the other hand, the acrylamide sheets cannot currently be made less than about $70 \mu\text{m}$. This experimental limitation does not preclude measurement of thin layers occurring by other means, such as the diffusion of ink stain on the elastin biomaterial. However, when considering the boundary interface regions, i.e. the sharp drop in pressure amplitude indicating the layer of no absorption, we found a drop with a $10 \mu\text{m}$ width. Assuming a sound speed of $1.52 \mu\text{m}/\text{ns}$, this gave a decay width of about 7 ns. Accounting for the 4.75 ns pulse width of the laser, there exists an additional 2 ns of delay in the slew between regions of different pressure amplitude. Although the effect was minimal here, it may be explained by the attenuation of high frequency components of the acoustic wave, resulting in a less responsive waveform. Such dispersive effects are known in acoustic propagation and should be considered when propagation distances approach the far field regime.

3.4.2 Computer Simulations

The computer simulations allowed an initial test of the absorption algorithm. Simulations could have included ideal, noiseless data, where the absorption algorithm would have reproduced the absorption coefficient in a stable manner. This chapter presented simulations with random noise, since it was more representative of actual data and tested

the algorithm's stability. For most of the simulations the results were within 5% for about 2 optical depths. For the 147 and 188 cm^{-1} gels, the results were within 10% for slightly less than 2 optical depths.

The instability at greater depths was due to the decreasing signal to noise ratio, when the signal amplitude became weaker due to the attenuation of optical energy with depth. Also, at higher absorption coefficients, namely for those greater than 140 cm^{-1} , decreased numerical stability occurs. This fact is due to higher values in the exponential term of equation 3.11, causing greater fluctuations in the value of the absorption coefficient.

3.4.3 Gel Absorption Coefficient

The acoustic waves generated in the acrylamide gels were exponentially decaying in accordance with Beer's Law, since the gels were homogeneous. The stability was slightly less than for the simulations for absorption coefficients of 30, 43, and 68 cm^{-1} . For the 117 cm^{-1} gel, stability of about 10% was shown for about 2.5 optical depths. For the 147 and 188 cm^{-1} gels, stability of only 20% was shown for less than 2 optical depths. The instability was due to the same reasons cited in the computer simulations, though the effect is aggravated for the more highly absorbing gels, probably due to measurement inaccuracies in the transducer.

The acoustic wave generated in the two layered acrylamide gel showed a two layered structure, as demonstrated by the two regions of decay. The result of the algorithm showed a value of about 130 cm^{-1} for the two regions of absorption, slightly lower than the 140 cm^{-1} value obtained by measurement from the spectrophotometer. The region of clear gel was delineated by the central region of low absorption coefficient. The value of the central region was not identically zero, probably due to noise in the signal. This noise was interpreted by the algorithm as a region of low absorption. The acoustic wave traveled through 1.16 mm of gel before being received by the transducer, indicating the data could be transmitted over ranges much greater than an optical depth without degradation. The limit would be the near/far field boundary. For an absorption coefficient of 30 cm^{-1} and a laser spot size of 0.3 cm, equation 3.4 gives a boundary of 0.6 cm.

3.4.4 Elastin Biomaterial

The acoustic wave of the stained biomaterial showed an exponential decay as the deposition of the ink could not be expected to be uniform. Diffusion of the ink in the biomaterial was likely to cause high concentrations near the surface, with decreasing concentration with depth. The result of the absorption coefficient algorithm shows a μ_a of about 70 cm^{-1} at the surface with a drop to zero at about $180 \mu\text{m}$. The partition coefficient is the ratio of the applied concentration to the surface concentration. Since it is the ratio of the concentrations, it suffices to use the ratio of the absorption coefficients. In this case, the applied absorption coefficient was 78 cm^{-1} . The surface absorption coefficient was 70 cm^{-1} , giving a partition coefficient of 0.9. This diffusion process can be modeled by the equation [80]

$$C(x, t) = C_{surface} \left(1 - \text{erf} \left(\frac{z}{2(\alpha t)^{1/2}} \right) \right) \quad (3.13)$$

where $C(x, t)$ is the concentration of the dye, $C_{surface}$ is the surface concentration, and α is the diffusion constant. Applying this model to the diffusion process of the ink stained biomaterial yields a diffusion constant of approximately $1 \times 10^{-6} \text{ cm}^2/\text{s}$. This model fit the absorption curve of figure 3.11, enforcing the applicability of the diffusion model to the data obtained by the acoustic analysis of the staining process.

3.4.5 Applications

Determination of absorption coefficient of soft, absorbing materials has obvious application in tissue optics. Numerous tissues are treated as homogeneous when they are clearly layered, e.g. human skin. The acoustic wave would be generated according to the absorption of the separate layers and then travel through more tissue unimpeded by optical attenuation. As long as the distance the acoustic wave travels is within the near/far field boundary mentioned in equation 3.4, a plane wave analysis would apply. The ability to characterize such layers by absorption in addition to the increased sensing range is advantageous over many purely optical methods. Further applications can be found in the characterization of absorption of stained tissues, as was shown with the elastin biomaterial. These diffusive stains can be looked upon as finely layered media, and may possibly

be better suited to the method of numerical analysis shown in this chapter, since successive layers would be similar, without harsh changes in the absorption values that contribute to the algorithms instability.

The application of characterizing the finely layered, or stained, media may be suitable for laser-tissue welding, since a tissue or biomaterial is typically stained with a chromophore to absorb laser light. While the exact mechanism of tissue welding is unknown, knowledge of the chromophore deposition and hence the initial temperature profile may be used to study the welding process.

Chapter 4

Localization of spherical photoacoustic sources in acrylamide gel phantoms using time domain measurements

*

4.1 Introduction

Photoacoustic methods have been used to obtain information about optical properties of laser irradiated targets [24, 26, 27, 31, 77, 81, 82]. The optical contrast between a hypervascular mass and the surrounding medium, such as a tumor in fatty tissue, may allow the generation of photoacoustic waves that can be used to localize the hypervascular mass. Analysis of the acoustic wave, particularly with respect to propagation time, may be used to determine the location, size, and optical properties of the photoacoustic source. Such information may be used for tumor imaging. This chapter offers an experimental set up and a simple computational algorithm that localizes the photoacoustic source. Sphere size is also studied and is computed using the duration of the acoustic pressure wave. Multiple spherical photoacoustic sources are also detected and the resulting acoustic waves are analyzed to discriminate the individual sources.

There are several ways in which laser light can be converted into acoustic radiation [7, 81]. This chapter investigates only the photothermal effect of a stress confined laser

*Parts of this chapter were submitted to the Journal of Applied Optics.

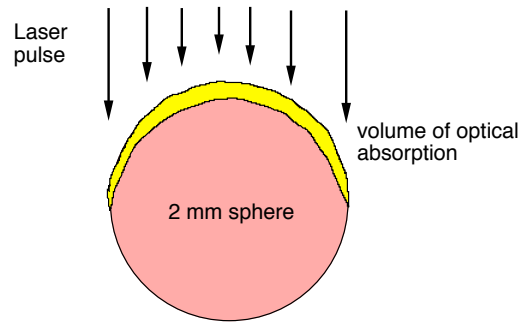


Figure 4.1: The absorption of optical radiation in an optically thick sphere occurs in the spherical cap closest to the direction of the laser pulse.

pulse resulting in a thermoelastic expansion. This thermoelastic expansion gives rise to an acoustic wave. A laser pulse can be considered stress confined if the pulse duration is shorter than the time required for the energy to acoustically radiate away from the region of optical absorption. This can be represented by the equation [27, 77, 82]

$$\tau < \frac{\delta}{c_s} \quad (4.1)$$

where τ is the pulse duration of the laser, δ is the absorption depth, and c_s is the speed of sound in the medium. The condition of stress confinement is met in the experiments described in this paper as the pulse duration of the laser was 5 ns, the speed of sound in the media is 1.5 mm/mms and the absorption depth of the absorbing sphere was *leq* 300 μm .

For an absorption coefficient of 60 cm^{-1} , a 2 mm sphere is not optically thin, meaning the absorption of optical energy is not homogeneous throughout the volume of the sphere. The absorption depth for a 60 cm^{-1} sphere is approximately 300 μm , thus the region of absorption in the sphere is a cap, as shown in figure 4.1. As the spheres were not optically thin, the localization algorithm determined the position of the spherical cap source, with the highest amplitude occurring with the acoustic wave peak. This peak corresponded to the central point of the surface of the cap, where absorption was the highest. The acoustic source with this geometry may be modeled by a hemispherical source with a radius equal to the original sphere with a smaller hemispherical source with negative

Laser Irradiation

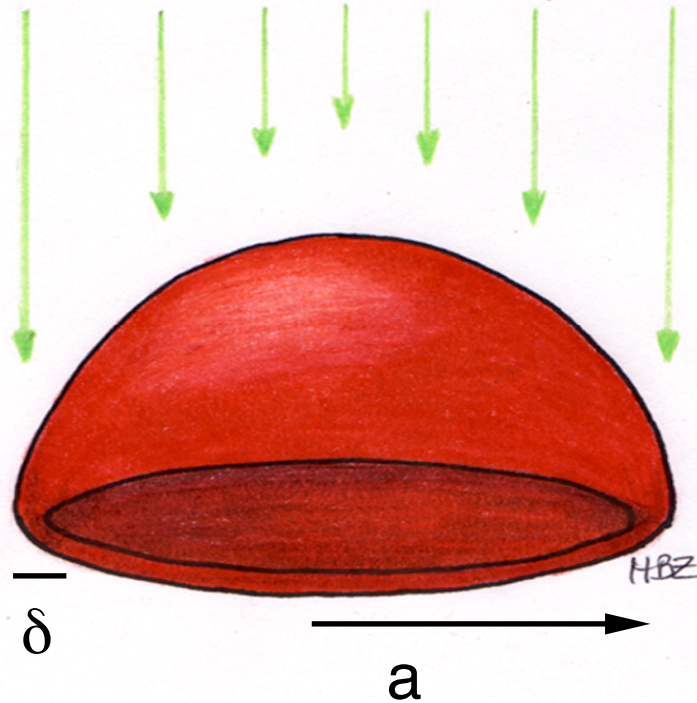


Figure 4.2: The volume of absorption of an optically thick sphere from a laser pulse is shown here as a red hemispherical cap. The radius of the cap is a , the same as the sphere itself, while the wall thickness of the cap is the absorption depth, δ .

amplitude with a radius equal to the radius of the sphere minus the absorption depth of the sphere (figure 4.2). Thus, the model would consist of an acoustic source in the shape of a spherical cap, similar to the absorption volume in an optically thick sphere, created by hollowing out the inner part of a hemisphere. The analytic form of the solution can be derived by integrating the spherical disks (Chapter 2) for form a hemisphere. A disk integrated from 0 to a_0 , where a_0 is the sphere diameter, gives the primary hemispherical source segment,

$$P(r, t) = \int_0^a j \frac{\rho_0 c}{2} U_0 \frac{a}{r} k a e^{j(\omega t - kr)} \left[\frac{2J_1(ka \sin \theta)}{ka \sin \theta} \right] da \quad (4.2)$$

where ρ_0 is the equilibrium density, c is the phase speed of the acoustic wave, U_0 is

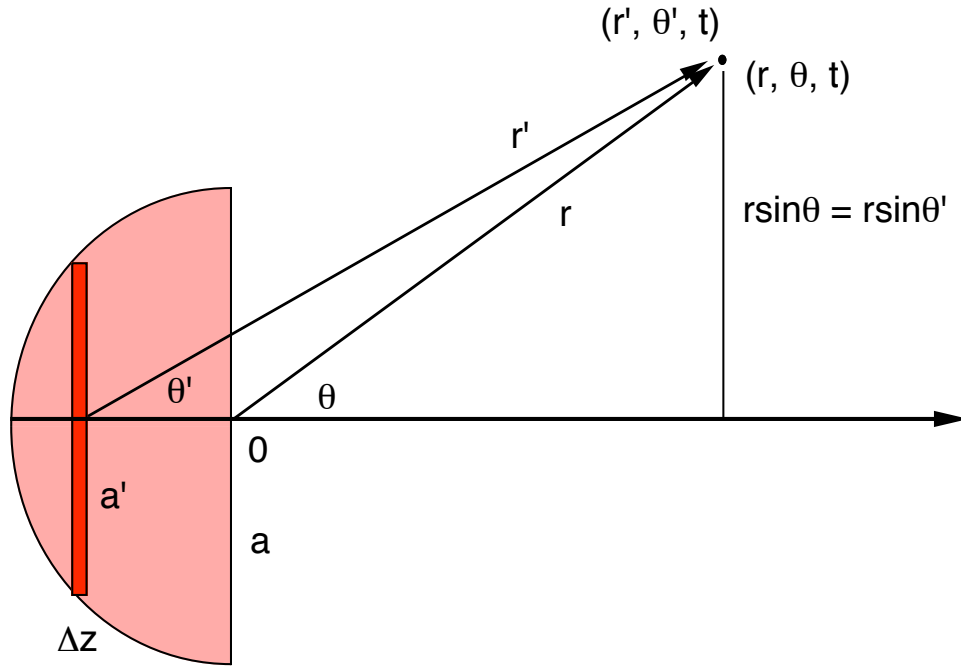


Figure 4.3: The acoustic field from a hemispherical source can be computed by treating the source as a collection of disk sources. Computing new radial distance, r' , angle, θ' , and disk radius, a' , allows the computation of the field due to the additional disks. Δz is the distance from the origin to the new disk face, measured along the horizontal axis.

the maximum particle velocity, k is the wavenumber, and ω is the harmonic frequency. Meanwhile, a disk integrated from 0 to $a - \delta$, where δ is the optical absorption depth gives the secondary hemispherical source which acts as a negative source. The result is a spherical cap source. Hence, the resultant acoustic field is given by the sum of the two hemispheres as

$$P(r, t) = \int_0^a p(r, z', t) dz - \int_0^{a-\delta} p(r, z', t) dz \quad (4.3)$$

This sum is valid as the acoustic wave equation is linear.

Computationally, the source is modeled by taking the disk sources and computing the new field according to the new radius, radial distance, and angle (figure 4.3 The disk diameters are expressed as

$$a' = a \sin(\arccos(\frac{\Delta z}{a})) \quad (4.4)$$

Δz is the distance that each subsequent disk used to construct the hemisphere is displaced

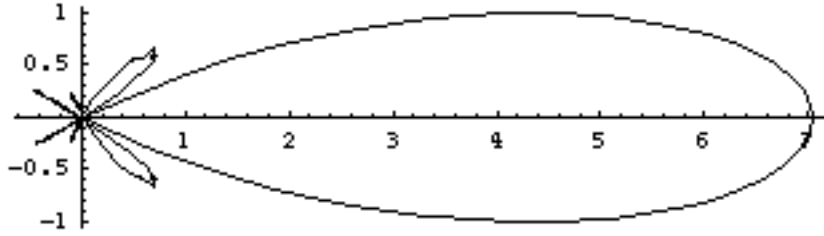


Figure 4.4: The spherical cap source is modeled here by creating a hemisphere from 10 successively smaller disks and then subtracting a smaller hemisphere from its core, made by a series of ten smaller disks. The beam pattern is similar to a plane piston source, without any weak deviations on or near the axis, as might have been supposed by the subtraction of the smaller hemisphere. Diffraction lobes are still evident on the beam pattern, as in the piston, though they disappear when the harmonic source is summed over a band of frequencies to create a pulsed source.

from the origin. This expression makes sense, as for $\Delta z = 0$, then $a' = a$. The new radial distance from the smaller disks, that are displaced from the origin, is

$$r' = (r^2 + \Delta z^2 - 2r\Delta z \cos(\pi - \theta))^{\frac{1}{2}} \quad (4.5)$$

The new angle is given as

$$\theta' = \arcsin\left(\frac{r}{r'} \sin(\theta)\right) \quad (4.6)$$

Thus, using the new expressions, r' , a' , and θ' , the fields due to each of the disks making up the hemisphere can be computed. The sum of the fields of the positive and negative hemispheres noted above make up the spherical cap. Thus the field due to a harmonically vibrating cap is given by the integrals in equation 4.3. A sum of such field using all frequencies up to several megahertz would give an approximation of the field due to an optically thick sphere irradiated by a stress confined laser pulse. Using these expressions, the beam pattern for a spherical cap harmonic source is shown in figure 4.4. The beam pattern was calculated by concatenating ten successively smaller disks, with the largest disk having unit size. The core of the hemisphere was removed by modeling ten disks, 10% smaller than the original series of disks. Thus, a spherical cap was produced. The resultant beam pattern is very similar to a plane piston. One may have supposed that the on axis portion of the beam would have been altered by the removal of the core of

the hemispherical source. This is clearly not the case for the harmonic case shown here and for a broadband case, which would appear the same with fewer diffraction lobes. This modeling was done to show that the detection scheme for optically thick spheres would not have to correct for some on axis deficiency in signal. Actual modeling of acoustic waves from optically thick spheres was performed using thermoelastic modeling, which wouldn't provide a beam pattern, is optimal for producing acoustic waves from pulsed sources.

In this chapter, spheres of various size were irradiated with stress confined laser energy giving rise to photoacoustic waves. The waves were detected and analyzed with respect to propagation time. This analysis resulted in localization of the spheres, recognizing the fact, noted above, that the sources may not have been truly spherical with respect to photoacoustic generation. The analysis, using multiplicative backprojection of the data, resulted in a 2-D map of the source location. An algorithm was implemented to more precisely resolve an image of the source. The irradiated sphere was localized to within 5% of its true position, as indicated on the localization map. The spheres also created an image source, due to the proximity of a reflecting boundary caused by the air/phantom interface at the phantom surface. The source was approximately 4 mm from the surface, creating an image 8 mm away, which was indicated in the localization map. The acoustic waves were then analyzed to determine the size of the spheres. Spheres of 1–5 mm in diameter with four absorption coefficients were studied. Finally, multiple spheres were irradiated to create paired sources. The final images discriminated the individual sources and a minimum center to center distance was measured.

4.2 Materials and Methods

4.2.1 Apparatus

The photoacoustic setup is shown in figure 4.5. A Q-switched, frequency-doubled Nd:YAG laser operating at 532 nm with a pulse duration of 5 ns was used to irradiate tissue phantoms. The laser operated at 10 Hz. The phantoms were either a turbid acrylamide block or a cuvette with mineral oil. The phantoms contained optically absorbing

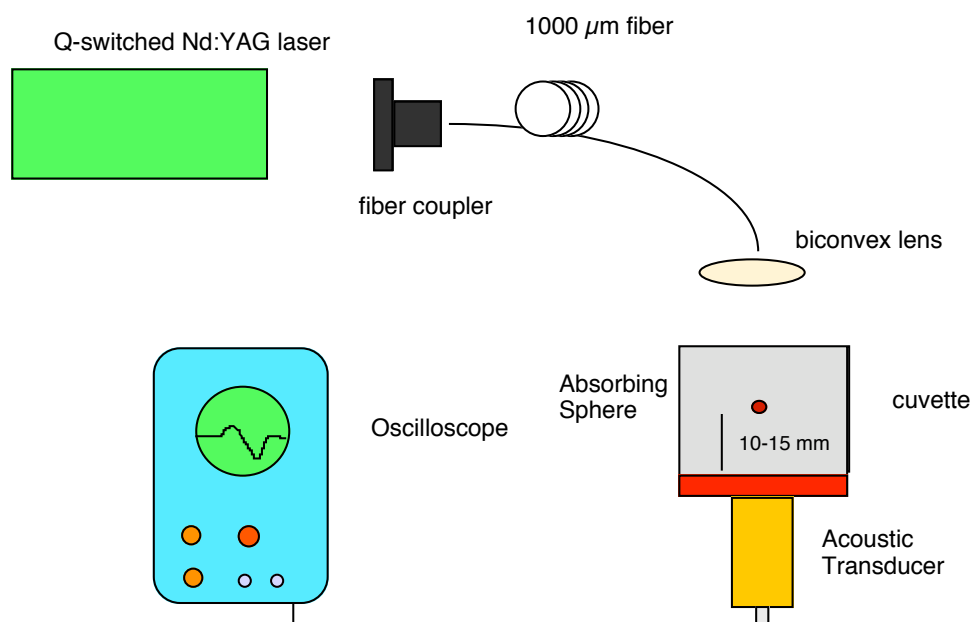


Figure 4.5: The photoacoustic experimental set up. The 532 nm laser pulse was coupled into a 1000 μm fiber. The fiber face was imaged onto the target. A PVDF transducer was used to detect the resultant acoustic waves. The waveform was then sent to a digital oscilloscope.

acrylamide spheres. The spheres used in the mineral oil experiments were 1–5 mm in diameter with absorption coefficients of 8, 16, 25, 50, and 60 cm^{-1} . The absorption coefficients for the spheres in the turbid blocks were 8, 25, and 50 cm^{-1} . The laser pulse was either coupled into a 1000 μm fiber or delivered as a free beam. The fiber coupling was used for irradiating the sphere in clear mineral oil, in order to provide a uniform laser spot. The free beam was used to irradiate the spheres in turbid acrylamide blocks in order to provide more laser energy. Due to optical diffusion by the turbid acrylamide block, the free beam was homogenized so that the spheres were irradiated uniformly.

For the spheres in oil, the output of the fiber was imaged onto the target via a biconvex lens with a focal length of 19 mm. The resultant laser spot was 3.3 mm in diameter with a pulse energy of 5.6 mJ. This gave a radiant exposure of 0.066 J/cm^2 . The laser pulse, being stress confined, created a photoacoustic wave which propagated through the phantom and was detected by a piezoelectric transducer. The transducer output was connected to a digital storage oscilloscope (DSA 602A, Tektronics, Wilsonville, OR). For the free beam, the spot size was approximately 5 mm at the gel surface and the energy delivered was about 70 mJ/pulse, for a radiant exposure of 0.365 J/cm^2 . The free beam, being more energetic, was used to irradiate the spheres in turbid acrylamide.

For the initial sphere detection scheme, a sphere was placed 15 mm above the detection plane, so that the detector was 15 mm directly below the bottom of the 2 mm acrylamide sphere. Thus, the acoustic signal was generated approximately 17 mm above the detector. The sphere was immersed in clear mineral oil. Next, the spheres were placed in a turbid acrylamide gel 10 mm above the detector plane, directly above the detector active area. Thus the acoustic signal was generated approximately 12 mm above the detector plane. The transducer was translated ± 6 mm laterally in 2 mm increments for additional detection points.

4.2.2 Acoustic Transducer

Two different acoustic transducers were used in this chapter. The acoustic transducers were piezoelectric detectors using polyvinylidene fluoride (PVDF) elements (figure 4.6). The first transducer, referred to as the small area transducer, was a small active area

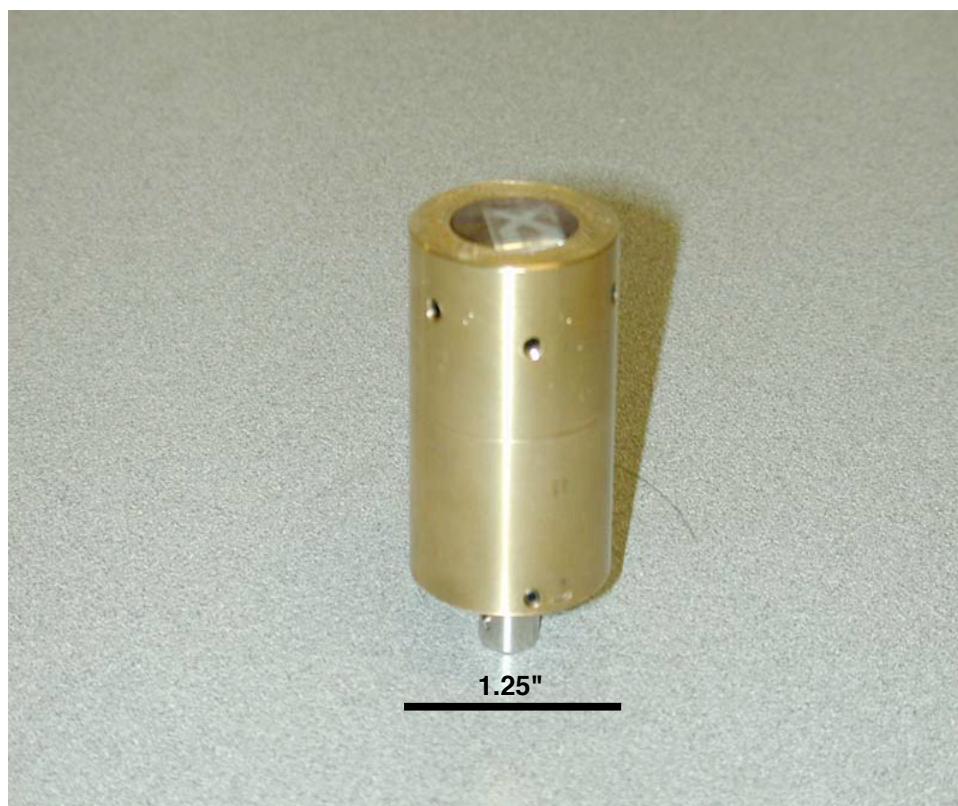


Figure 4.6: The acoustic transducer was a PVDF film detector in a brass housing. A BNC was connected to the PVDF electrodes for coupling to the oscilloscope. The $1.8 \times 1.8 \text{ mm}^2$ active area is shown as the crossed region on the top of the transducer.

transducer (KP-135, Ktech, Albuquerque, NM). A 25 μm thick PVDF element was placed on a plastic substrate. The active area was made by sputtering electrodes on either side of the PVDF. The area where the electrodes overlapped created the active area. The active area was $1.0 \times 1.0 \text{ mm}^2$. This transducer, having the smaller active area, was used for the sphere localization experiments.

The second transducer, referred to as the large area transducer, was built and tested from a PVDF element and a brass housing. The PVDF film was coated on both sides with aluminum, which was etched with FeCl_3 to form the active area. The active area was in the form of two crossed aluminum electrodes. The PVDF active area was 1.8 mm by 1.8 mm and placed on a 2 cm long cylindrical plug of acrylic. The acrylic plug served as a base for the sensing element and was housed in a brass cylinder. The negative and positive electrodes were connected to a BNC connector. This transducer was used for the sphere size experiments.

The transducer sensitivities were calibrated using absorbing solutions made from Direct Red 81 (Sigma Chemical) and deionized water. The solutions were purely absorbing and had absorption coefficients of approximately 25, 50, 100, 150, and 200 cm^{-1} as determined with a spectrophotometer (Hewlett Packard, 8452A Diode Array Spectrophotometer). The calibration setup is shown in figure 4.5, with an absorbing Direct Red 81 solution used instead of an absorbing sphere. The 532 nm Nd:YAG laser was coupled to the 1000 μm optical fiber and the fiber face was imaged onto the surface of the Direct Red solutions by a biconvex lens. The spot on the surface was 3.3 mm in diameter. The energy of the laser pulse was 5.6 J, giving a radiant exposure of 0.066 J/cm^2 . The acoustic waves were averaged over 32 pulses. The pressure of the resulting acoustic wave was calculated using [27, 82]

$$p_0(z) = \frac{1}{2} \mu_a \Gamma H_0 \exp(-\mu_a z) \quad (4.7)$$

where Γ is the unitless Grüneisen coefficient. The value $\Gamma = 0.12$ was used [27, 77]. The Grüneisen coefficient describes the fraction of optical energy that is translated into thermoelastic expansion. The depth in the medium is given by z . H_0 is the incident laser radiant exposure. For $z = 0$, the pressure can be calculated and the corresponding voltage on the acoustic peak will indicate the transducer calibration factor in mV/bar .

The actual voltage from the transducer can be expressed as

$$V(t_0 - t) = \frac{\Gamma\mu_a}{2H_0} \exp -\mu_a c_s(t_0 - t) C_{cal} \quad (4.8)$$

where $V(t_0 - t)$ is the voltage signal received after the event at time, t_0 , c_s is the sound speed, and C_{cal} is the calibration factor to convert the pressure into a voltage signal. The inverse of this calibration factor is determined experimentally and used to convert the voltage signals into pressure.

4.2.3 Acrylamide Gels

Tissue phantoms were made with acrylamide gels. Acrylamide gels were used to create small spheres with Direct Red 81 (Sigma Chemical) as an absorber. The spheres were 2 mm with $\mu_a = 8, 25$, and 50 cm^{-1} . These spheres were placed in turbid acrylamide blocks and were subsequently immersed in turbid acrylamide solution that was gelled, making the spheres embedded within the turbid blocks. The spheres were also submerged in mineral oil (Mineral Oil, Fleet Pharmaceuticals, Lynchburg, VA). These spheres were 1–5 mm in diameter with $\mu_a = 8, 16, 30$, and 60 cm^{-1} . The spheres were then irradiated with the laser to create acoustic waves. The spheres used in the sphere size determination experiments were 8, 20, 38, and 59 cm^{-1} .

The acrylamide was made according to the procedure outlined by Sathyam *et al.* [78] and Viator *et al.* [82]. 9.735 g of acrylamide and 0.265 g of bis-acrylamide (Sigma Chemical) were dissolved in 50 ml of deionized water to form a 20% polyacrylamide gel. Polymerization was induced by adding an initiator of 0.02 g of ammonium persulfate and 0.2 ml of TEMED (Sigma Chemical). For the turbid blocks, a 1:20 dilution of Intralipid in deionized water (Liposyn II, Abbott Laboratories, North Chicago, IL) was used instead of pure deionized water.

The absorbing spheres were made by injecting small quantities of acrylamide solution into heated mineral oil. The acrylamide had been chemically initiated, so that the spherical drops of acrylamide in the mineral oil would gel. The oil was heated to 80°C to accelerate the gelling process. The amount of injected acrylamide solution determined the size of the spheres. Three small spheres are shown in figure 4.7.

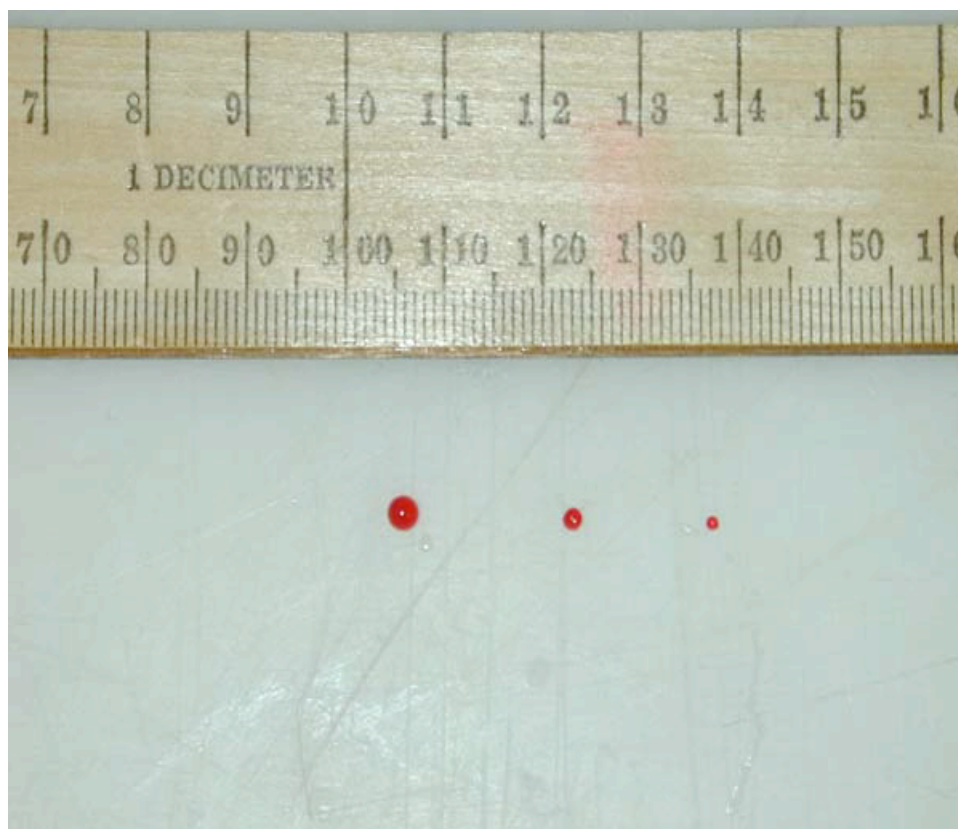


Figure 4.7: Three acrylamide spheres are shown here. The sizes are 3 mm, 2 mm, and 1 mm as shown from left to right.

4.2.4 Optical Scattering Measurements

The turbid phantoms were made by making acrylamide gels with Intralipid as an added scatterer. The proportion of Intralipid was 1%, to simulate tissue with a reduced scattering coefficient of 15 cm^{-1} . The 1% solutions were tested for scattering properties using experiments based on diffusion theory and by a photoacoustic method, which derived the reduced scattering coefficient from the effective attenuation.

The diffusion theory method used fluence measurements by taking the spectrum of three solutions of 1% Intralipid. The fluence measurements and "added absorber" method is described in Wilson *et al.* [83–85]. One solution was purely scattering (the absorption of Intralipid and water at 532 nm was neglected), a second solution had an absorption coefficient of 0.5 cm^{-1} at 532 nm due to the addition of Direct Red dye (Sigma Chemical, St. Louis, MO), while a third solution had an absorption coefficient of 1.0 cm^{-1} from Direct Red. A fixed $400 \mu\text{m}$ optical fiber delivered light from a broadband source (Ocean Optics Inc., Dunedin, FL) and collected with a radially translated $400 \mu\text{m}$ fiber, which was connected to a spectrometer (Ocean Optics Inc., Dunedin, FL). The spectra were stored and analyzed by diffusion theory code that computed the optical properties of the solutions.

The photoacoustic method determined the scattering coefficient by fitting the acoustic waveform with an exponential fit and deriving μ_{eff} , the effective attenuation coefficient. By generating acoustic waves in turbid media where μ_a , the absorption coefficient is known, μ_s' , the reduced scattering coefficient can be derived according to the following identity.

$$\mu_s' = \frac{\mu_{\text{eff}}}{3\mu_a} - \mu_a \quad (4.9)$$

In these experiments, three solutions of 1% Intralipid were used with absorption coefficients of approximately 1, 2, and 3 cm^{-1} at 532 nm. The absorption was provided by adding Direct Red dye. The solutions were irradiated from above by the 532 nm laser connected to a $1000 \mu\text{m}$ optical fiber. The acoustic waves were detected in transmission by the large area transducer. The resultant acoustic waves were analyzed for effective attenuation, from which the reduced scattering coefficient was derived.

4.2.5 Acoustic Wave Simulation

Acoustic waves generated from irradiating spherical absorbers were simulated using MATLAB code (The Mathworks, Natick, MA). The acoustic waves were modeled by thermoelastic expansion following stress confined heating as described by Beer's Law attenuation in laser irradiated spherical absorbers. The theory is delineated in Paltauf *et al.* [68] in the theory of photoacoustic generation in liquids. The detection point was simulated to match the geometry used in the experiments, where the spheres were irradiated from above and the detection point was below the sphere and laterally translated for additional detection points.

4.2.6 Backprojection Algorithm

A localization algorithm was written in Mathematica (Wolfram Research, Urbana-Champaign, IL). The algorithm is expressed as a product

$$M(x, z) = W_1(t) \otimes W_2(t) \quad (4.10)$$

where $M(x, z)$ is the two dimensional localization map that indicates the source location and $W_i(t)$ is the i^{th} acoustic waveform, normalized by its maximum value. Higher values of $M(x, z)$ correspond to higher certainties of source location. The product is given by \otimes . The localization takes each point of the first acoustic waveform and correlates its value with each point of the second waveform. Alternatively, the relation between the localization map and the waveforms can be described as operations on the x and z coordinates

$$M(x, z) = W\left(\frac{1}{c}\sqrt{(x-d_1)^2+z^2}\right) \cdot W\left(\frac{1}{c}\sqrt{(x-d_2)^2+z^2}\right) \quad (4.11)$$

where the multiplication is carried through for x and z , the lateral and vertical distances, respectively. $M(x, z)$ is unitless and has values from 0 – 1, similar to a probability distribution, where higher values correspond to higher probabilities of source location. The transducer translation distance from directly beneath the sphere is denoted as d . A typical localization map as a density plot is shown in figure 4.8. A 2 mm acrylamide sphere was irradiated in a turbid gel block 5 mm above the acoustic transducer. A second detection point was taken by translating the detector 2 mm laterally. The two resultant waveforms

were used in the backprojection algorithm and the localization map was produced. The backprojection arcs are visible in the density plot. The density plot indicated the source location by the single bright spot at the intersection of the arcs. The source was indicated at a distance of 5 mm, offset to the side by about 1 mm, indicating either a measurement error in the initial placement of the sphere in the acrylamide or an error in the implementation of the algorithm or a combination of the factors.

4.2.7 Sphere Size Calculations

Sphere size was determined by a simple, geometric analysis of the acoustic waves. Referring to figure 4.9 the propagation time, t_1 , for the pole of the sphere (region "1") is

$$t_1 = \frac{z + 2r}{c} \quad (4.12)$$

where z is the distance from the bottom of the sphere to the acoustic detector and r is the sphere radius. This is so, as the propagation path is the diameter of the sphere (twice the radius) and the distance from the bottom of the sphere to the detector. The propagation time, t_2 , for the equator of the sphere (region "2") is

$$t_2 = \sqrt{(z + r)^2 + r^2} \quad (4.13)$$

since the propagation path is the hypotenuse of the right triangle created by the radius of the sphere and the radius with the distance from the bottom of the sphere to the detector. Using the relation, $z = ct_1 - 2r$ from equation 4.12 and substituting it into equation 4.13 yields

$$r = \frac{2ct_1 \pm \sqrt{4c^2t_1^2 + 8(c^2t_1^2 - c^2t_2^2)}}{4} \quad (4.14)$$

This relation gives the sphere radius. An acoustic wave from a 2 mm diameter, 60 cm^{-1} sphere is shown in figure 4.10. The pole and equator times are obtained by equating the regions "1" and "2" with the pole and equator, respectively.

In the sphere size experiments, the large area transducer was used to detect acoustic waveforms from spheres of various size. The transducer was placed directly below the sphere location. The sphere location could be determined using the backprojection scheme. 8, 20, 38, and 59 cm^{-1} spheres were used. The size of the 8 cm^{-1} spheres were 1, 1.9, 2.7,

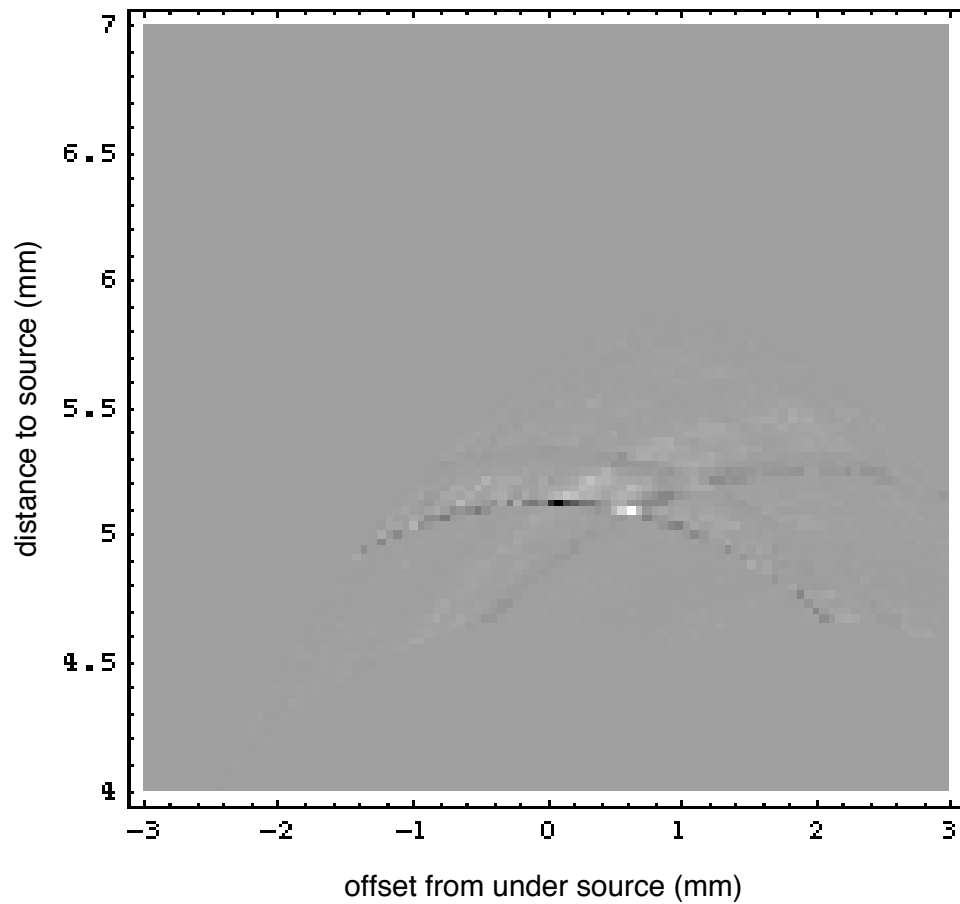


Figure 4.8: This is a density plot of the location of an absorbing acrylamide sphere in a turbid acrylamide block. The bright spot at the intersection of the backprojection arcs indicates the predicted position of the photoacoustic source. The vertical axis shows the distance above the initial transducer location (5 mm), while the horizontal axis shows the lateral offset of the sphere from the transducer (0.5 mm). The true position was 5 mm above and 0 mm offset.

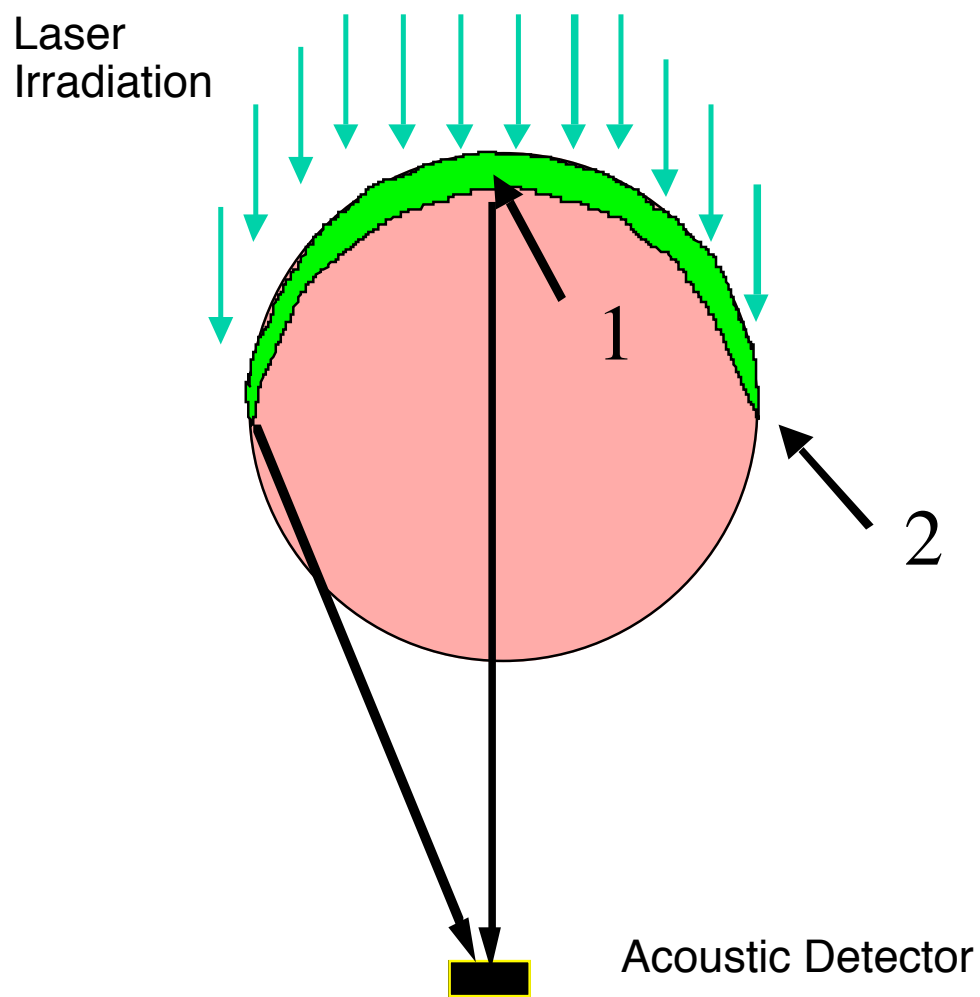


Figure 4.9: The acoustic wave generation for the optically thick sphere is shown here. The region marked "1" is the pole, having the longest propagation time to the acoustic detector, while the region marked "2" is the equator, having the shortest propagation time.

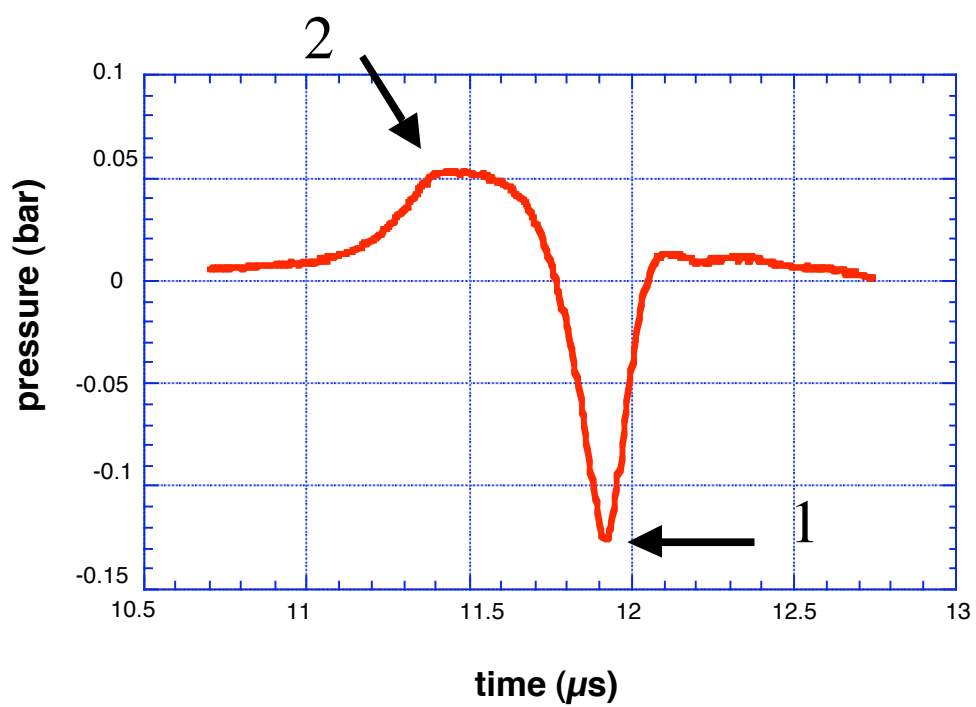


Figure 4.10: The acoustic wave from a 2 mm diameter, 60 cm^{-1} sphere in clear mineral oil. The region marked "1" comes from the pole, as in figure 4.9. Likewise, the region marked "2" comes from the equator.

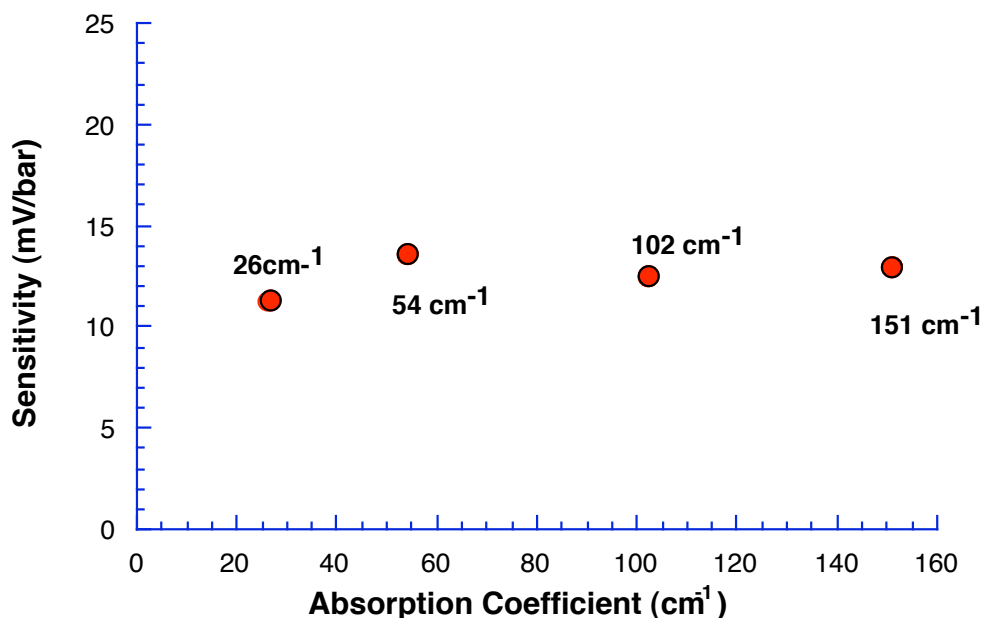


Figure 4.11: This is the calibration curve for the large area PVDF transducer. The sensitivity was done for 26, 54, 102, and 151 cm^{-1} Direct Red 81 solutions. The calibration was approximately $12.6 \pm 0.8 \text{ mV}/\text{bar}$.

and 3.6 mm. The size of the 20 cm^{-1} spheres were 1.1, 1.6, 2.3, 3.1, and 4.8 mm. The size of the 38 cm^{-1} spheres were 1.1, 1.8, 2.4, 3.2, and 4.8 mm. The size of the 58 cm^{-1} spheres were 0.9, 1.5, 2.3, 3.3, and 4.5 mm. The sphere sizes were measured with a digital micrometer.

4.3 Results

4.3.1 Transducer Calibration

The calibration curve for the large area transducer sensitivity is shown in figure 4.11. The transducer sensitivity was $12.6 \pm 0.8 \text{ mV}/\text{bar}$ over the range of 26, 54, 102, and 151 cm^{-1} Direct Red solutions. The calibration curve for the small area transducer sensitivity is shown in figure 4.12. The transducer sensitivity was $11.6 \pm 0.4 \text{ mV}/\text{bar}$ over the range of 25, 48, 101, and 200 cm^{-1} Direct Red solutions. This result was applicable to the absorption coefficient of the optically thick spheres, being 60 cm^{-1} .

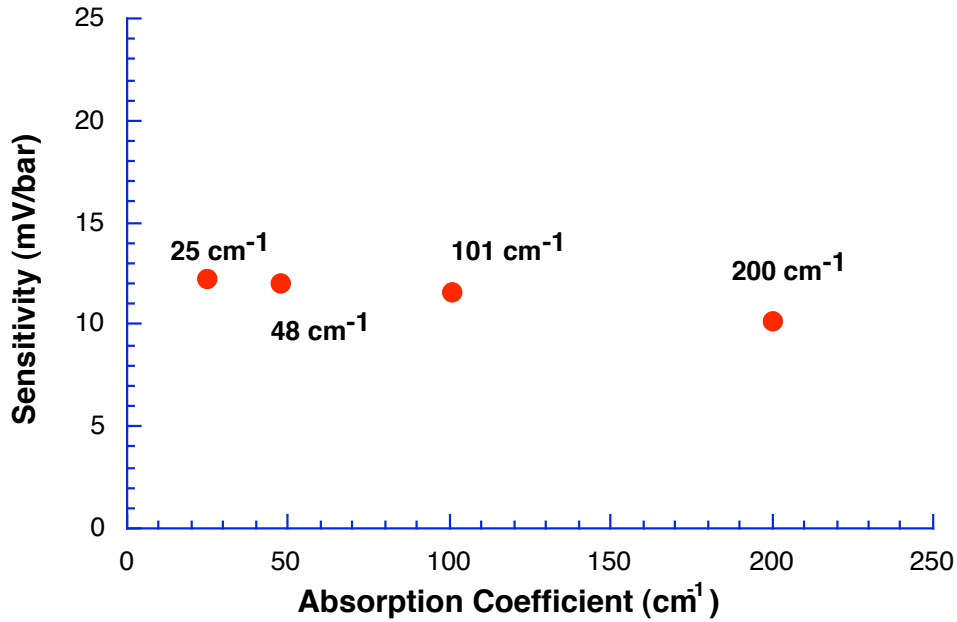


Figure 4.12: This is the calibration curve for the small area PVDF transducer. The sensitivity was done for 25, 48, 101, and 200 cm^{-1} Direct Red 81 solutions. The calibration was approximately 11.6 ± 0.4 mV/bar.

4.3.2 Optical Scattering Measurements

The reduced scattering coefficient of the 1% Intralipid solution was determined by the fluence measurement method to be $19.6 \pm 1.6 \text{ cm}^{-1}$ at 532 nm. The reduced scattering coefficient of the photoacoustic method is shown in Table 4.1.

Table 4.1: The reduced scattering coefficients of the 1% Intralipid solutions were calculated by determining the effective attenuation of the solutions of known absorption coefficient. The errors for the effective attenuation coefficients are standard deviations, while the error for the reduced scattering was derived from error propagation.

Solution	μ_{eff} (cm^{-1})	μ_a (cm^{-1})	μ_s' (cm^{-1})
solution 1	9.0 ± 0.9	1.07	23.8 ± 5.2
solution 2	11.2 ± 0.4	2.14	17.3 ± 1.4
solution 3	13.8 ± 0.3	3.126	16.4 ± 0.8

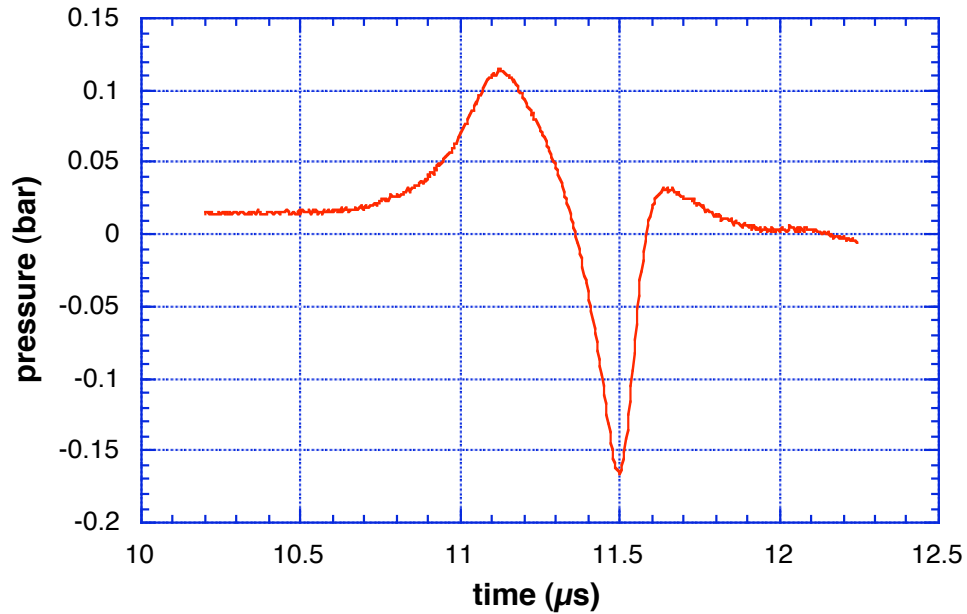


Figure 4.13: This is the waveform from irradiating an optically thick sphere (60 cm^{-1}) with a 2 mm diameter 15 mm directly above the PVDF transducer. The sphere was immersed in clear mineral oil.

4.3.3 Acoustic Waveform from Optically Thick Spheres

A photoacoustic waveform for a 2 mm sphere with an absorption coefficient of 60 cm^{-1} is shown in figure 4.13. In this case, the sphere was directly above the detector at a distance of 15 mm. The negative peak corresponding to the center of the spherical cap was detected at $11.5 \mu\text{s}$, indicating a distance of 17.25 mm. Since the actual source was the top cap of the sphere, this corresponded to the correct propagation time of the acoustic wave. The waveform is similar to the computer simulation for a 60 cm^{-1} , 2 mm sphere positioned 15 mm from the detector (figure 4.14).

4.3.4 Sphere Size Determination

The result for the sphere size determination experiments are shown here. The results for the 59 cm^{-1} spheres are shown in figure 4.15 The results for the 38 cm^{-1} spheres are shown in figure 4.16. The results for the 20 cm^{-1} spheres are shown in figure 4.17. The

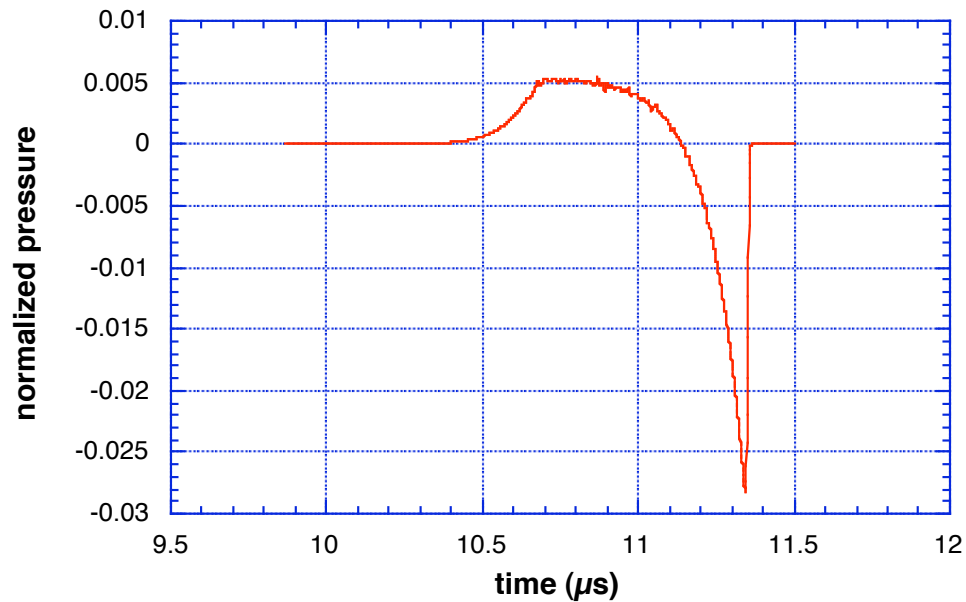


Figure 4.14: A simulation of a 60 cm^{-1} , 2 mm sphere irradiated by a stress confined laser pulse. The sphere was centered 15 mm above the detector.

results for the 8 cm^{-1} spheres are shown in figure 4.18.

4.3.5 Localization of Spherical Sources

A simulation of an acoustic wave from irradiating a 2 mm diameter, 60 cm^{-1} sphere 18.5 mm directly above a detector is shown in figure 4.19. A simulation of an acoustic wave from irradiating a 2 mm diameter, 60 cm^{-1} sphere 18.5 mm translated 6 mm laterally from above a detector is shown in figure 4.20. The result of the backprojection algorithm on the two simulated waveforms is shown in figure 4.21.

Two acoustic waveforms from the photoacoustic source are shown in figure 4.22. In each graph, the first waveform is the initial acoustic wave detected by the small area PVDF transducer. The second waveform is a reflection from the surface of the tissue phantom. This image source was included in the localization algorithm. The three dimensional rendering of the localization map of the acoustic waveforms is shown in figure 4.23. The map indicates that the sphere position was directly above the initial detector position at a

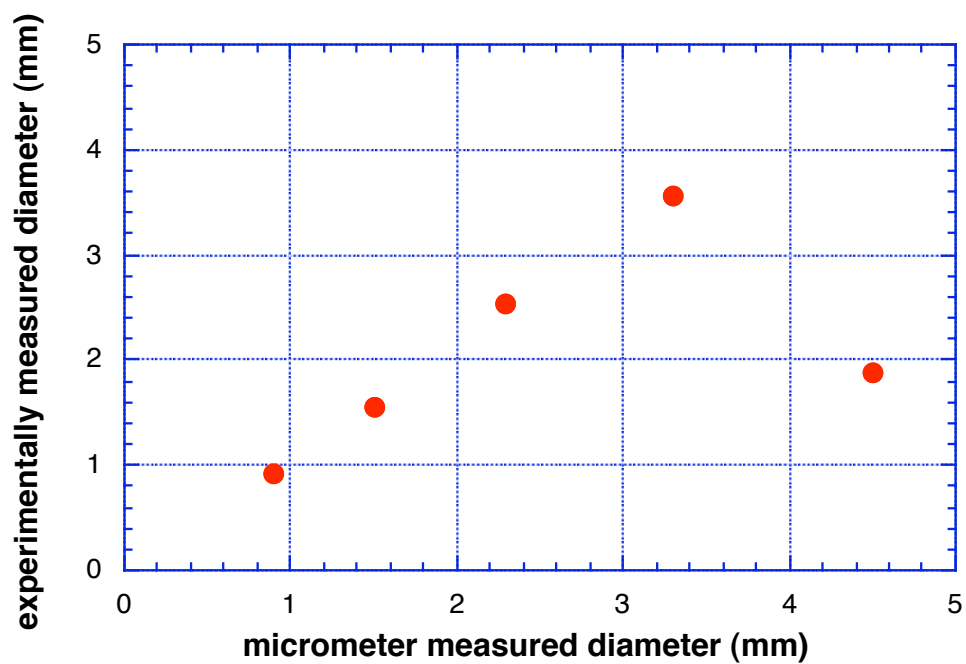


Figure 4.15: The experimentally derived diameters, from equation 4.14 are graphed on the vertical axis, while the measurements on the horizontal axis are from the digital micrometer.

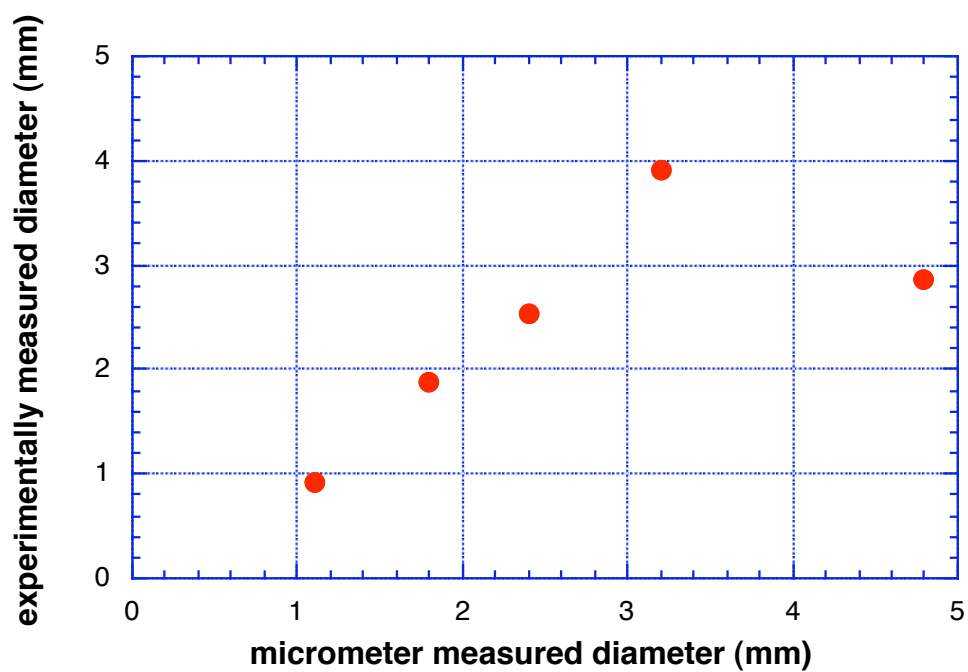


Figure 4.16: The experimentally derived diameters, from equation 4.14 are graphed on the vertical axis, while the measurements on the horizontal axis are from the digital micrometer.

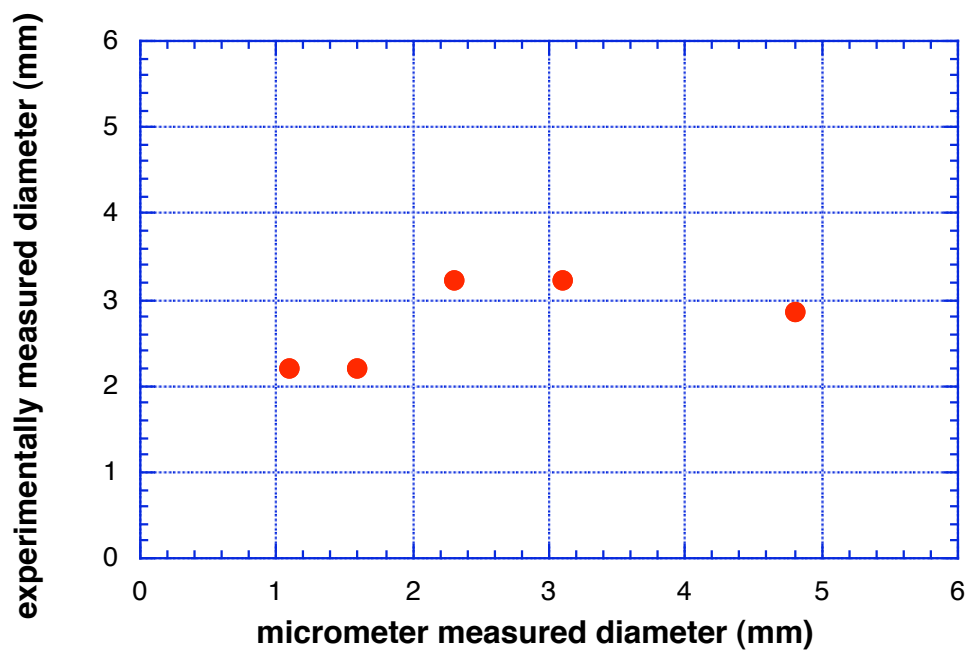


Figure 4.17: The experimentally derived diameters, from equation 4.14 are graphed on the vertical axis, while the measurements on the horizontal axis are from the digital micrometer.

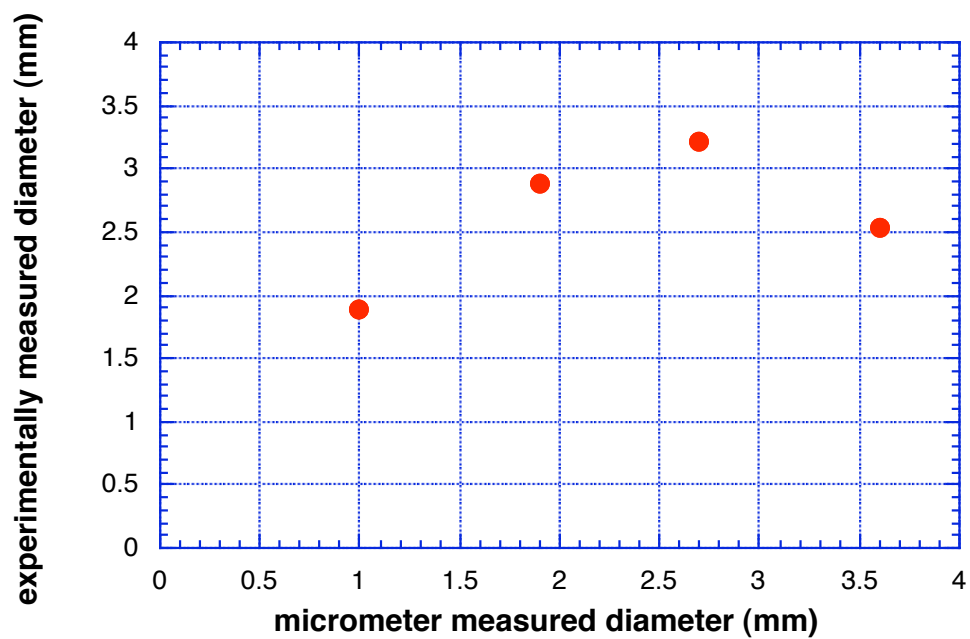


Figure 4.18: The experimentally derived diameters, from equation 4.14 are graphed on the vertical axis, while the measurements on the horizontal axis are from the digital micrometer.

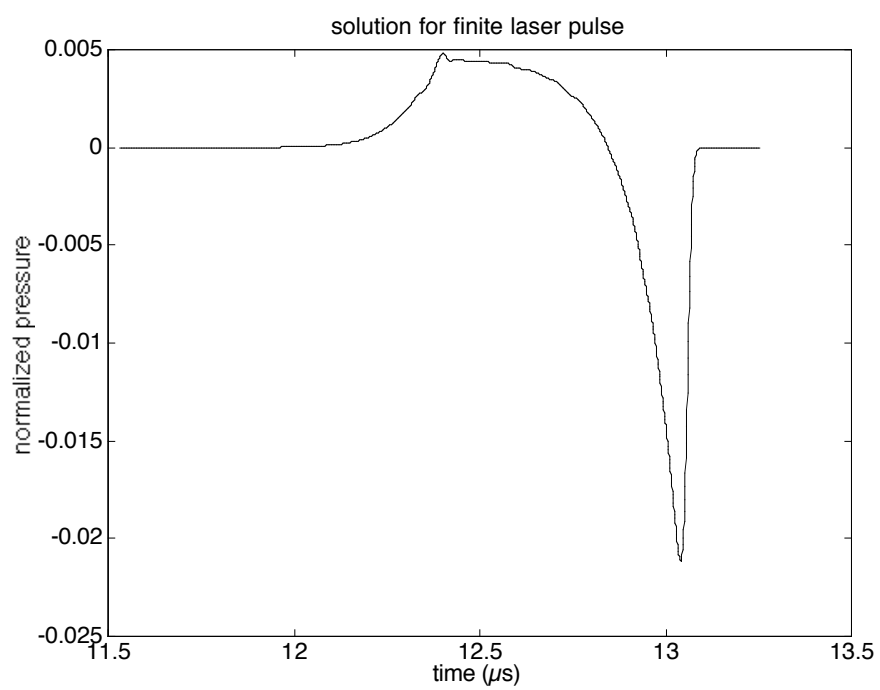


Figure 4.19: The acoustic wave simulation of a 2 mm diameter, 60 cm^{-1} sphere directly above a detector.

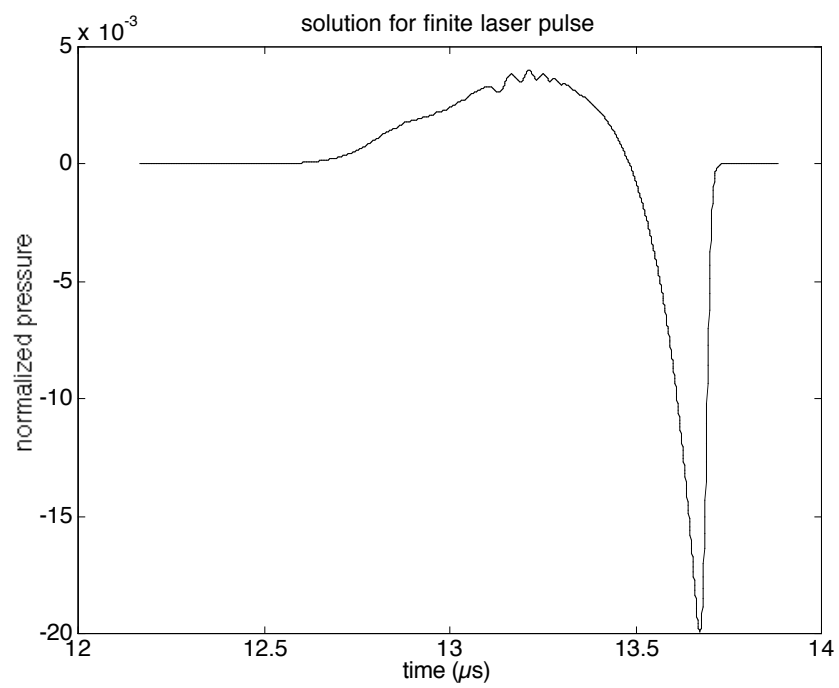


Figure 4.20: The acoustic wave simulation of a 2 mm diameter, 60 cm^{-1} sphere translated 6 mm laterally from above a detector.

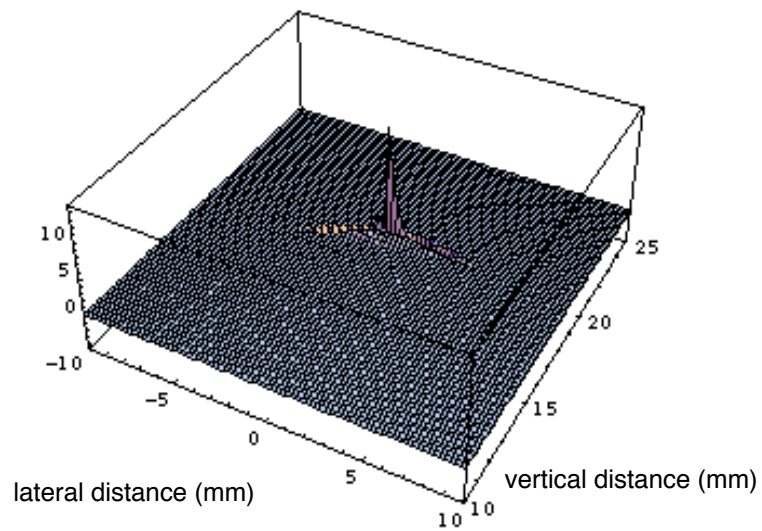


Figure 4.21: The localization map of the simulated acoustic waves. The source is shown by a sharp peak exactly on the simulate source location, directly above the detector at 18.5 mm.

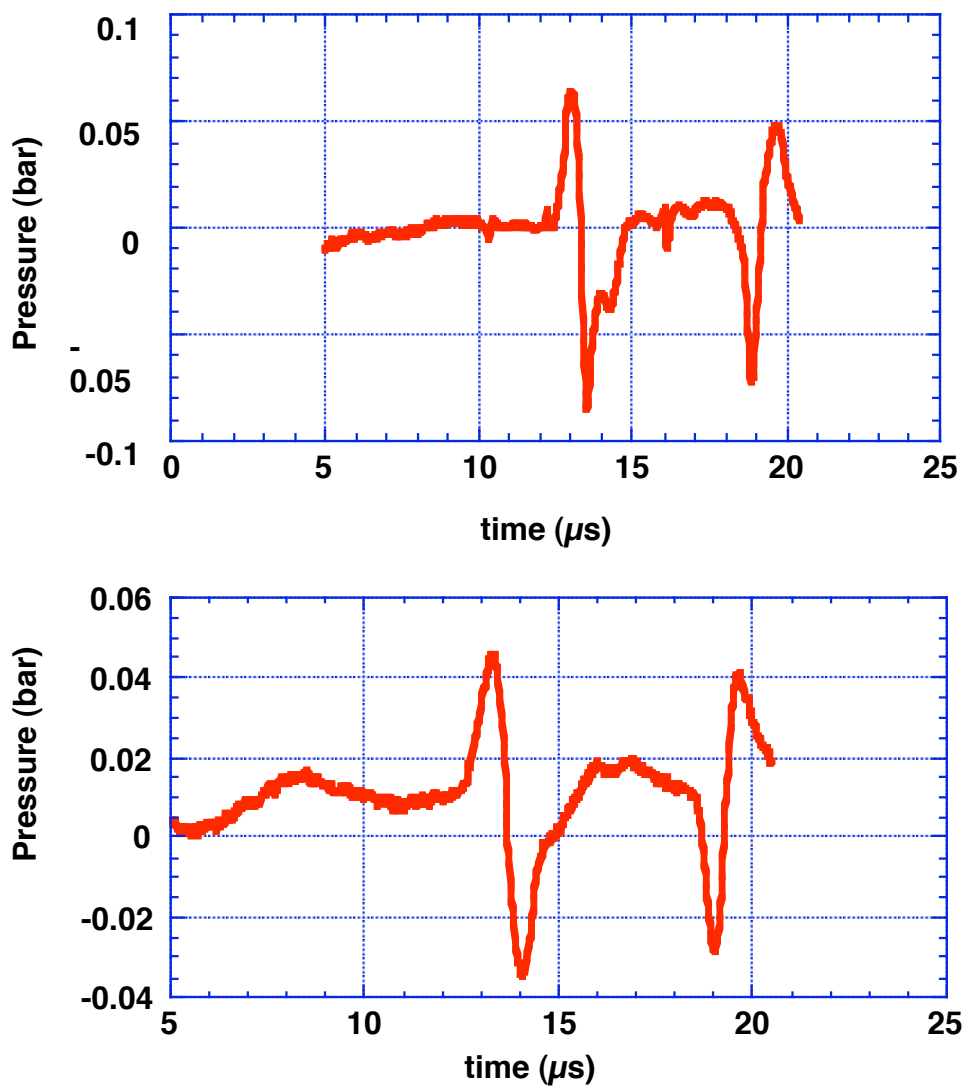


Figure 4.22: The two waveforms used for the localization algorithm are shown here. The first waveform (top) was from the initial detector position. The second waveform (bottom) was from the detector translated 6 mm laterally. The first peak on both waveforms was from the actual sphere. The second peak on both waveforms was from the acoustic reflection from the acrylamide surface.

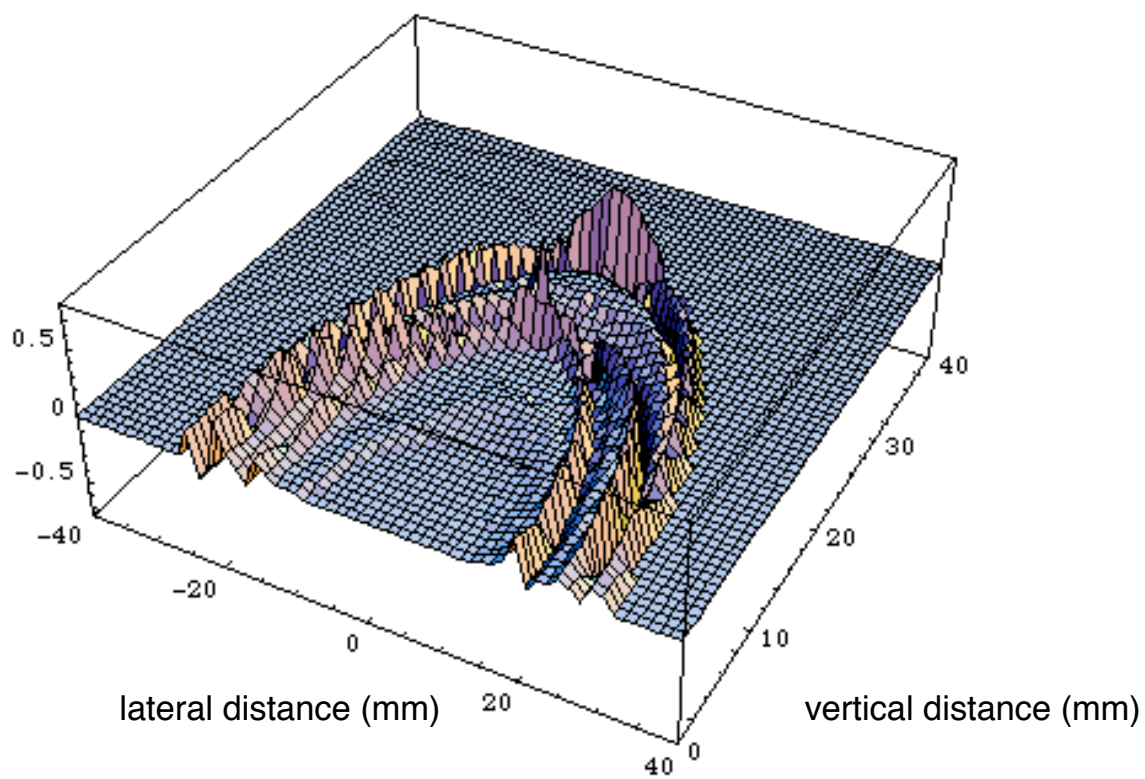


Figure 4.23: This is a 3-D graphic indicating the position of the spherical source as predicted by the localization algorithm.

distance of 21 mm. The true position was 20 mm, since the sphere was 2 mm in diameter and the distance from the bottom of the sphere to the detector was 18 mm. The prediction was within 5% of the true value. The image source was 8 mm above that, outside the tissue phantom, clearly indicating a virtual source.

4.3.6 Localization of Paired Sources

The acoustic waveform from a paired photoacoustic source is shown in figure 4.24. The spheres were 2 mm in diameter and had optical absorption coefficients of 60 cm^{-1} . The spheres were side by side, separated by 3.5 mm center to center. The upper figure shows the acoustic wave from directly beneath the pairs at a distance of 10 mm. The acoustic detector was then offset from the paired source, so that the detector was translated 4 mm from being directly beneath the center of mass of the paired source. The localization map for the paired source is shown in figure 4.25.

4.4 Discussion

Photoacoustic imaging has been studied recently with some success. Jacques *et al.* [31] and Andersen *et al.* [32] used optical detection schemes to find buried absorbers using photoacoustic methods. Liu offered theoretical investigations into photoacoustic imaging using the Radon transform and the P-transform [86, 87]. Esenaliev *et al.* [88] performed experiments to find the detection limit of tumor phantoms in gels and chicken breast tissue. They detected signals from 2 mm spheres in gelatin at a distance of 60 mm. They also detected small pieces of liver buried in chicken breast tissue at a distance of 80 mm. This chapter attempts similar detection using propagation time to detect optically absorbing spheres in tissue phantoms. The eventual goal is to localize tumors and determine size and optical properties.

4.4.1 Optical Scattering Measurements

The optical scattering measurements were used to ensure that the optical properties of the tissue phantoms were realistic for simulating tissue. A reduced scattering coefficient

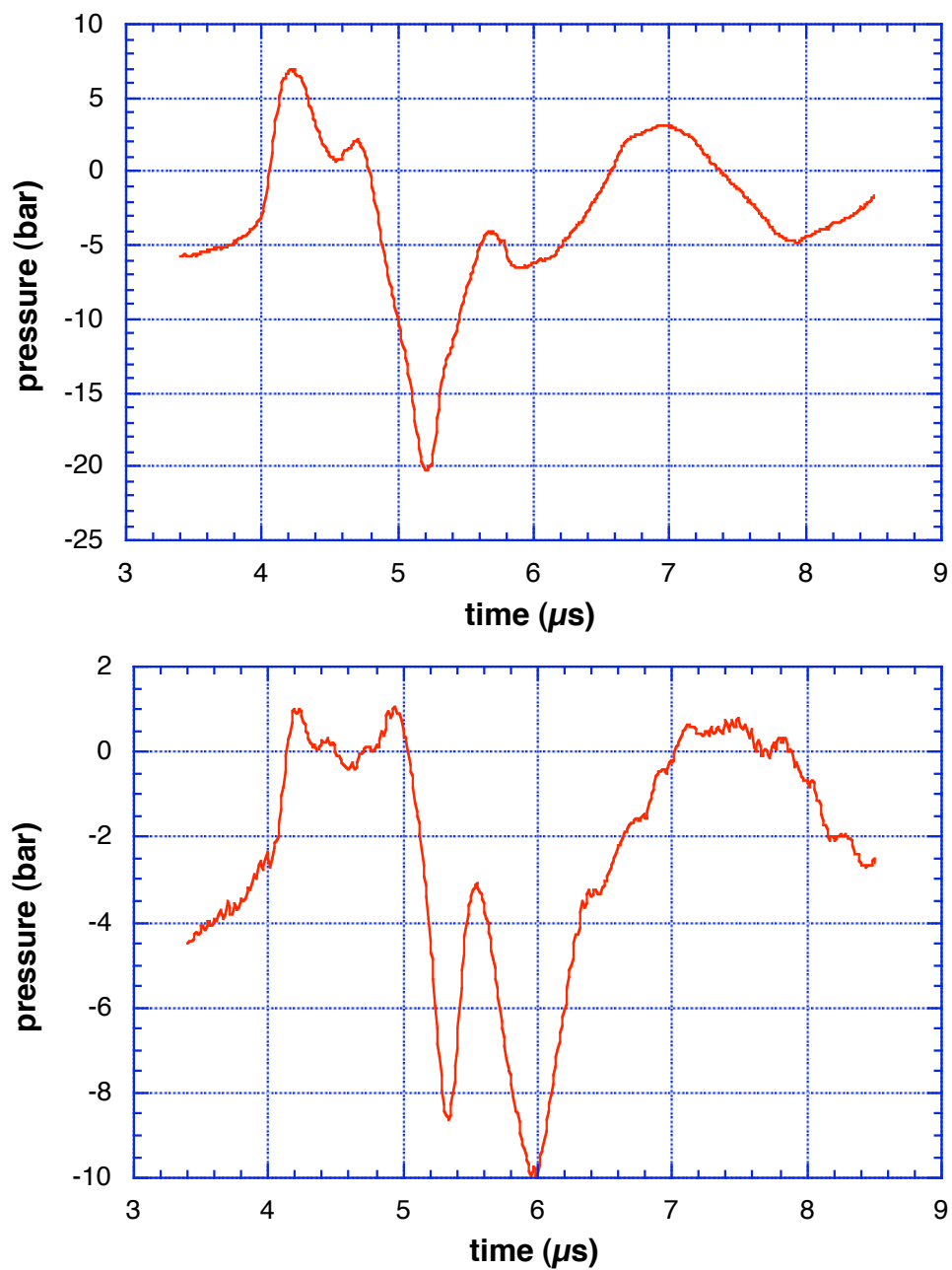


Figure 4.24: The acoustic waves from the irradiated pairs in turbid acrylamide. The spheres were 2 mm in diameter and space 3.5 mm center to center. They had an absorption coefficient of 60 cm^{-1} . The top waveform is from irradiating the spheres with the detector directly below. The lower waveform is after laterally translating the detector 4 mm.

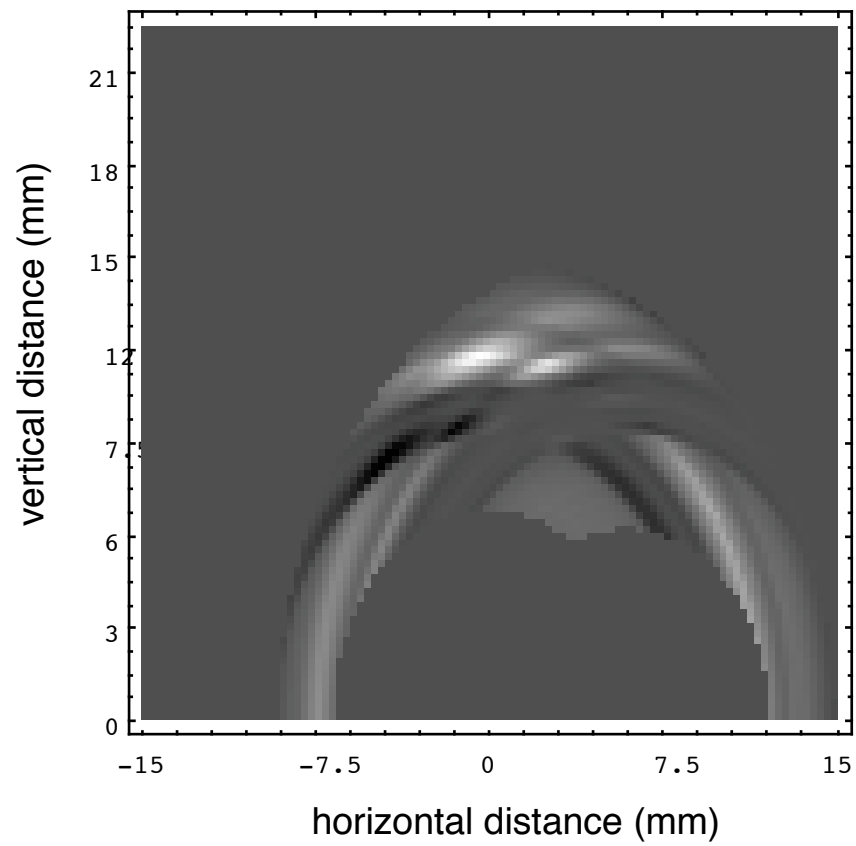


Figure 4.25: The localization map for the paired source is shown here. Though there is some noise, the two bright spots indicate the paired sources in their actual locations.

of $15\text{--}20\text{ cm}^{-1}$ at 532 nm was attempted. The 1% Intralipid solution was used to get this scattering and it was verified using diffusion theory and by a photoacoustic method. The diffusion theory method indicated a reduced scattering coefficient of $19.6 \pm 1.6\text{ cm}^{-1}$. The photoacoustic method indicated 23.8 ± 5.2 , 17.3 ± 1.4 , and 16.4 ± 0.8 , for each of three Intralipid targets. The first target had a high standard deviation due to difficulty in curve fitting of such a small amplitude pulse. The second and third targets had better curve fits, indicating that a reduced scattering coefficient of about 17 cm^{-1} . Thus the turbid phantoms, including a 0.5 cm^{-1} background absorption, was an appropriate model for tissue.

4.4.2 Acoustic Waveform from Optically Thick Spheres

The acoustic waveforms for optically thick spheres conformed closely to the simulations of optically thick spherical photoacoustic sources using the thermoelastic expansion model. The top cap of the sphere (the pole) was manifested as a negative peak. This correlated to measurements, including propagation time and the sphere size model. The reason that the cap was a negative peak could be explained by considering the cap as a small disk source, where the diameter and thickness are nearly equal, giving significant diffractive effects. As the disk diameter increases (by looking at lower latitudes of the sphere) the diffractive effect becomes less until the source becomes positive, as on the positive peak, indicating the sphere's equator.

A difference in the simulated waveform and the empirical one was shown as a plateau in the positive region in the simulated wave. This plateau was a result of the Beer's Law attenuation in the thermoelastic model. In the empirical data, the positive peak was narrower, although the drop to the negative peak was also somewhat exponential. The difference could have resulted from actual diffractive effects from the equatorial region, truncating the wave from its elongated simulation.

4.4.3 Sphere Size Determination

The sphere sizes were determined using a simple geometric model which assume that the spheres were optically thick. For the 59 cm^{-1} spheres, the experimentally derived

diameters were all within 5% of the actual diameter, except for the second largest sphere, which was within 7%. The largest sphere in all cases was bigger than the actual laser spot, so the derived diameters were all incorrect. These diameters should have been equal to the spot size, though the 8 and 59 cm⁻¹ spheres indicated that the largest spheres were about 2–2.5 mm, much smaller than the 3.3 mm laser spot. The 38 cm⁻¹ spheres showed derived diameters within 5% of the actual diameter, except for the 4 mm sphere. The 8 and 20 cm⁻¹ spheres showed incorrectly derived sphere diameters, probably due to the fact that the spheres were no longer optically thick and that the geometric model relied on that assumption. For a 20 cm⁻¹ sphere, the absorption depth was 500 μm, which was 1/2 of the smallest sphere radius. The 8 cm⁻¹ sphere had an absorption depth of 1.25 mm, which was greater than the smallest sphere radius. This geometric model could be modified to account for the large absorption depth, though prior knowledge of the absorption coefficient must be known. If it was known beforehand that the spheres were optically thin, then the geometric analysis would use $t_1 = \frac{z+2r}{c}$, as the top pole of the sphere remains the region of optical absorption most distant to the detector. The closest region would no longer be the equator, as the optically thick model showed, but it would be the bottom pole of the sphere. This would result in $t_2 = \frac{z}{c}$. Using this value for t_2 , the sphere size was determined to within 10% of the actual sphere size for the smallest 20 cm⁻¹ sphere and the 8 cm⁻¹ sphere with a diameter of less than 2 mm.

4.4.4 Localization of Spherical Sources

The backprojection algorithm was first tested on simulated acoustic waves (figures 4.19 and 4.20), obtained from the thermoelastic model. These acoustic waves were nearly noise free and the regions away before and after the waveform were uniformly zero. Thus the backprojection map was extremely clean, with a sharp source prediction within a few percent of its actual position. There were small backprojection arcs evident, though the signal to noise ratio was much greater than 10:1 for the correct position versus the arcs. An alternative use of the algorithm would be to backproject the velocity potential of the photoacoustic sources, where the velocity potential is the time integral of the pressure from the relation, $p(t) = \rho \frac{d\phi}{dt}$, where $p(t)$ is the pressure, ρ is the density, and ϕ is the

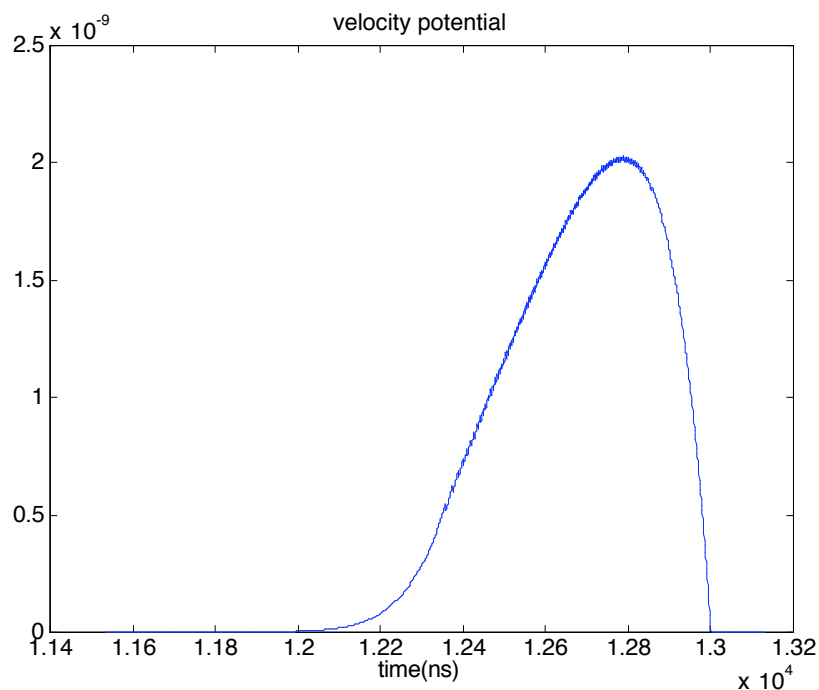


Figure 4.26: This is the velocity potential of the simulated acoustic wave from a 60 cm^{-1} spherical source, 18.5 mm above an acoustic detector. The function has only positive values, as it is the integral of a bipolar pulse with equal energy in the pressure and tensile components. The velocity potential is everywhere zero except where the pressure wave is nonzero.

velocity potential. The velocity potential of the on-axis simulated acoustic wave is shown in figure 4.26. The advantage of working with the velocity potential is that it has only positive values for a bipolar pressure wave where the energy is equally divided between the acoustic wave and the accompanying tensile wave. Additionally, the function returns to zero after the nonzero components of the pressure wave are integrated. Thus the backprojection would be localized exactly on the source, without a negative tensile peak. The algorithm was used for the simulated data, with the localization being within 2% of the source location. The integral of the pressure wave from the experimental data did not yield an actual velocity potential, since experimental noise made the energy balance with the tensile wave appear uneven. Thus the integrated pressure wave showed a pseudo-potential

that never returned to zero, but slowly diverged to infinity, causing the backprojection scheme to show a high source probability far from the source.

The backprojection algorithm on actual acoustic waves (figure 4.22) showed less of a defined source, with several backprojection arcs evident. The dominant source peak in the localization map was within 5% of its true position. Additionally, image sources were evident from reflection from the gel/air interface. The distance between the source and the interface was 4 mm, giving an image source 8 mm above the true source. This image source would not be confused with the true source, as it will always exist beyond the gel/air interface, outside of the tissue phantom. The acoustic waveforms exhibited some of the low frequency perturbations found by irradiating scattering media with a small background absorption. These small bumps in the signal contribute to false correlations on the localization map, though if the true signal has enough contrast (a much higher amplitude), the true source will be easily distinguished on the localization map.

The backprojection algorithm used here, being multiplicative, may show some advantage over the conventional method. In this application, each point on the first waveform is multiplied with each point on the second waveform. Thus, large amplitude spikes on one waveform enhance large amplitude spikes on the other waveform, while low amplitudes tend to inhibit other low amplitudes. Thus, the localization map shows a high peak for the position indicated by each acoustic wave as the source, while other points on the map tend to flatten out. This scheme may also be enhanced by extending the product in the backprojection algorithm to additional waveforms.

4.4.5 Localization of Paired Sources

The paired waveforms (figure 4.24) were much more problematic than either the simulations or the single sphere sources. The paired source, being two 2 mm diameter spheres, was 3.5 mm center to center distance. The pairs that were closer spaced were not well distinguished from each other. The on axis paired source acoustic wave, the waveform obtained by setting the detector directly below the pair, showed some low frequency perturbation after the initial waveform. The first peak showed some evidence of a paired

source, indicating the detector may have been slightly offset, as the pair would have appeared as a single source if the detector were directly beneath the source. The off axis wave definitely showed a second source, though the first peak was deformed, having a plateau. This may have been due to low frequency perturbations from the background absorption or pyroelectric effect on the transducer, since the source signal was weaker, since the detector was not directly beneath the source. The backprojection still managed to show two distinct sources, though the center to center distance seemed to be close to 3 mm. The bright spots on the localization map are the paired sources, with the vertical distance predicting about 11 mm, 10% greater than the true distance. The map may be enhanced by additional detection points being introduced into the algorithm or possibly by a reconstruction scheme. The density plot was chosen as it showed the sources better than the three dimensional map, due to extensive noise.

4.4.6 Conclusions

The goal of this chapter was to introduce a method for determining location and size of spherical photoacoustic sources in turbid media, as an attempt to model hypervascular tumor masses in scattering tissue. The optical properties of the turbid gels matched the expected scattering of some human tissue and included some background absorption to account for small amounts of perfusion. The sources were optically thick, as might be expected in a tumor, since a 10% perfusion in a tumor may give an absorption coefficient as high as 30 cm^{-1} at laser wavelengths near 532 nm. The sources were localized with the multiplicative backprojection and sphere size was determined for optically thick sphere. The greatest difficulty was from the optical scattering. The scattering of light onto the acoustic detector gave rise to a pyroelectric effect, manifested by a low frequency modulation that interfered with the true signals. Even more importantly, the scattering of light before reaching the spheres reduced the fluence at the sphere, making the background absorption near the surface significant when compared to the spherical sources themselves. The scattering and background absorption problems can be only aggravated *in vivo*, since the optical properties are not precisely known and may not even be uniform over the region under investigation. The backprojection algorithm was shown to be robust, however,

and a combination of proper laser energy, source strength, detector set up, and signal processing may allow precise imaging of tumor masses in tissue.

Chapter 5

Design and testing of an endoscopic photoacoustic probe for determining treatment depth after photodynamic therapy of esophageal cancer

5.1 Introduction

Photodynamic therapy (PDT) is a means of treating cancerous tumors by activating a drug which is preferentially absorbed or retained by the tumor. Drug activation is achieved by irradiating the tumor site, causing cell death in the tumor [89–96].* While the use of light for activating drugs has been known since the time of Herodotus in ancient Greece [97], the first use of PDT for oncologic reasons occurred in 1903, when eosin was used to treat skin cancer. More recently, PDT has been used to perform palliative treatment in esophageal cancer [89–92]. Currently, there is no means to evaluate the depth of treatment immediately following a PDT treatment in the esophagus. Knowledge of the treatment depth would aid the clinician in determining followup treatment, including the need for additional PDT procedures. This chapter describes the design, construction, testing, and use of a photoacoustic probe for use in determining treatment depth *in situ* immediately after the PDT treatment. This information may aid the clinician in deciding how to proceed with treatment of the tumor site.

*Part of this chapter was submitted to the Journal of Biomedical Optics.

5.1.1 Photodynamic Therapy for Esophageal Cancer

Esophageal cancer kills approximately 10,000 people per year [92, 98, 99]. The later stages of esophageal cancer are aggravated by dysphagia, weight loss, pain and fatigue. The dysphagia, or difficulty in swallowing, significantly decreases the patient's quality of life and is the chief aim of palliation. Additionally, palliation relieves pain and tumor bleeding [92]. Treatment of esophageal cancer includes mechanical dilation of the esophagus, stenting, and surgical esophagectomy [92, 100, 101]. Mechanical dilation tends to be ineffective for other than short periods and may cause tissue trauma. Esophagectomy is a drastic surgical procedure.⁵ In 1996, the FDA approved the use of PDT in palliative treatment of obstructing esophageal cancer.

In a PDT case, the patient is intravenously given a photosensitive drug, such a porphyrin sodium (Photofrin), which accumulates in the cancerous tissue. Approximately 48 hours later, an optical fiber is introduced within the esophagus via an endoscope. The optical fiber irradiates the tumor with approximately 300 J per cm of fiber over 10–12 minutes. The temperature rise in the tissue is physiologically negligible due to the laser light. The light activated drug produces oxygen radical species in the tumor which results in cell death. Upon light treatment, tissue blanching occurs due to the cessation of tissue perfusion, indicating the necrotic region of the treatment area. Photographs of the PDT treatment of an esophagus are shown in figure 5.1. The blanched areas indicate necrotic tumor tissue. The depth of necrosis should be equal to the blanched layer thickness, as indicated by the debridement of the tissue during the next 24 to 48 hours.

5.1.2 Photoacoustic Propagation Time

Photoacoustic propagation time has been used for locating positions of optical absorbers in tissue or tissue-like media. The key element in this type of scheme is that a known acoustic propagation time and sound speed will give an indication of the position of the acoustic source. This idea is at the heart of backprojection reconstruction. Esenaliev *et al.* [88] used propagation time methods to image deeply embedded tumor models in gelatin phantoms and to detect liver embedded in chicken breast. Viator *et al.* [69] used

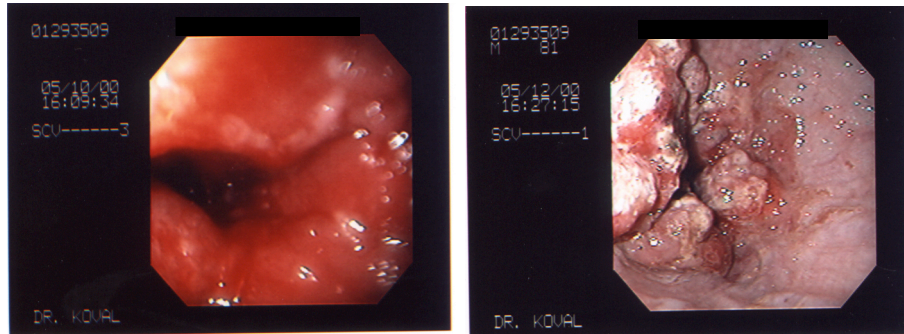


Figure 5.1: Photographs of the pre- and post-treatment esophagus. In the left photograph, the tumor area is shown as bulbous obstructions in the esophageal lumen. In the photograph on the right, the region of necrotic tissue is shown as a white, blanched area. The thickness of this blanched area indicates the depth of necrosis and hence, the depth of PDT treatment.

propagation time to detect small, optically absorbing spheres in turbid acrylamide gels. This chapter uses simple propagation time analysis to determine the thickness of a turbid layer over an optically absorbing layer in order to model the blanched (necrotic) layer after PDT treatment in esophageal cancer.

A photoacoustic probe was designed that contained both a piezoelectric transducer, made from a polyvinylidene fluoride (PVDF) film, and a $600\ \mu\text{m}$ optical fiber (figure 5.4). The optical fiber, referred to as side firing, delivered stress confined laser pulses in a direction orthogonal to the long axis of the fiber, while the PVDF film, located alongside the end of the side firing fiber, detected the resulting acoustic waves. The simple equation

$$d = c_s \tau \quad (5.1)$$

shows the relationship of the propagation time and sound speed to the source distance, where d denotes the distance from the transducer to the absorbing (perfused) layer, c_s is the speed of sound in the tissue, or tissue-like, medium, and τ is the time between the absorption of optical energy and the acoustic wave detection by the transducer. An artist's rendering of the use of the photoacoustic probe is shown in figure 5.2, where the probe is introduced to the esophagus via the working lumen of an endoscope. The probe comes into contact with blanched layers, where it irradiates the tissue and subsequently detects

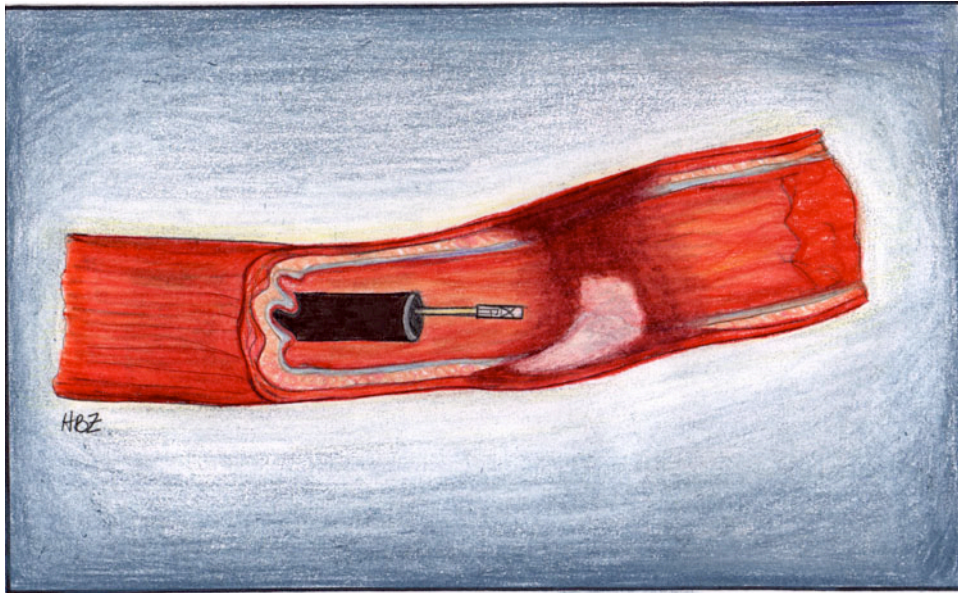


Figure 5.2: An artist's rendering of the use of the endoscopic photoacoustic probe. The probe emerges from the endoscope and is directed to treated (blanched) areas to determine the depth of necrosis.

acoustic waves resulting from absorption in the deeper, perfused layer of esophagus. The probe was constructed and tested on clear and turbid layers over optically absorbing layers of various absorption coefficients. The probe needed to fit into the working lumen of an endoscope used in esophageal PDT. It needed to be sturdy, so as not to disintegrate within the esophagus and sensitive enough to detect blood perfusion in the healthy esophageal tissue underlying the blanched, necrotic layer. The probe was then used to detect a buried vein phantom in a turbid medium. Finally, it was used to compare signals *in vivo* of a normally perfused and underperfused finger tips.

5.2 Materials and Methods

5.2.1 Photoacoustic Set Up

The set up for testing the photoacoustic probe is shown in figure 5.3. A Q-switched, frequency-doubled Nd:YAG laser (Quantel Brilliant, OPOTEK, Carlsbad, CA) operating

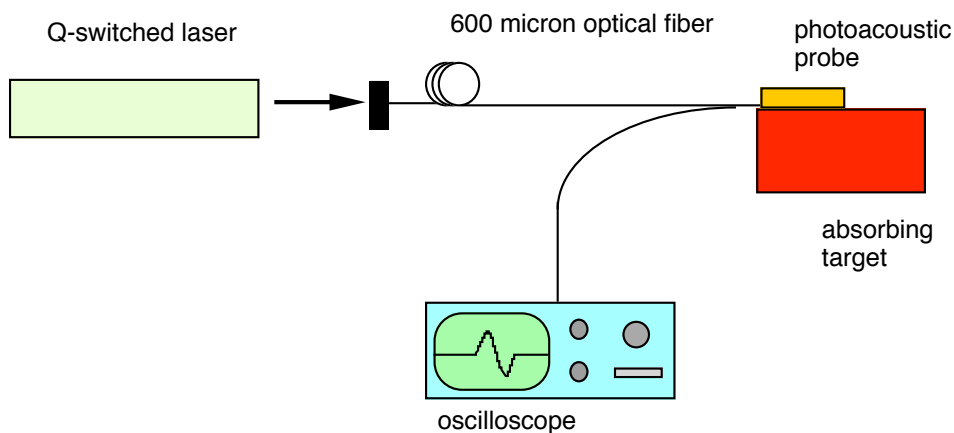


Figure 5.3: The Q-switched laser launched 532 nm, 5 ns pulses into a 600 μm fiber. A piezoelectric detector was positioned at the end of the optical fiber. Optically absorbing targets were irradiated by the fiber and the resulting acoustic waves were detected by the piezoelectric element. The signal was sent to the oscilloscope.

at 532 nm launched 5 ns pulses into a 600 μm quartz optical fiber. The pulse repetition rate was 10 Hz. The pulse energy out of the laser was approximately 5 mJ. The pulse energy out of the fiber was approximately 2–2.5 mJ. The optical fiber was mode mixed by coiling the fiber. The photoacoustic probe, described below, was attached to the end of the optical fiber. The probe was tested on various absorbing targets with the resulting acoustic signal being sent to an oscilloscope (DSA 602A, Tektronix, Wilsonville, OR). The bandwidth of the oscilloscope was 300 MHz with 1 Gsamples/s. The input impedance of the oscilloscope was 1 M Ω when the signal was not electronically amplified and 50 Ω when the signal was amplified. For all experiments in which the target was submerged within a scattering solution, a background measurement was taken on pure scattering solution without any embedded absorber. This background measurement was subtracted from all subsequent measurements to account for optical backscattering into the acoustic probe, resulting in an interfering pyroelectric signal, and to account for any absorption of the scattering solution itself.

5.2.2 Probe Construction

The photoacoustic probe was designed to couple an acoustic transducer to an optical fiber. The optical fiber delivered pulses of light from the Q-switched laser discussed previously in the set up. The acoustic transducer detected pressure signals resulting from the deposited laser energy. Both elements of the probe, the fiber and the transducer, were designed so that they would fit into the 2.8 mm working lumen of an endoscope used in the PDT procedure. The fiber/transducer pair were approximately 2.4 mm in diameter. The center to center distance from the fiber face to the acoustic detector was approximately 1100 μm . The optical fiber was side firing. This was accomplished by polishing the distal fiber face at a 45° angle. This angled fiber face directed the laser energy orthogonally to the axis of propagation of the fiber. To ensure a glass/air interface for proper reflection at the 45° angled face, the fiber tip was encased in a glass tube and sealed. The acoustic transducer was coupled alongside the fiber and was side detecting, meaning that the active area was positioned to optimally detect pressure signals emanating from the direction of the deposited laser energy. The acoustic transducer design is shown in figure 5.4. The transducer was made from miniature coaxial cable (UT-34, Micro-Coax, Pottstown, PA) with a total diameter of 860 μm . The coaxial cable was composed of a center conductor, a dielectric, and a conducting shield. The shield of the coaxial cable was made from silver plated copper wire. The dielectric was made from polytetrafluoroethylene (PTFE). The center conductor was made from silver plated copper wire and had a diameter of 200 μm . The characteristic impedance was 50 Ω . The capacitance was 95 pF/m. The last 7 mm of the coaxial cable was milled halfway, as shown in figure 5.5, for placement of the PVDF film. A 7 × 1 mm² sheet of 25 μm thick PVDF film, which had aluminum deposited on both sides, was connected to the center conductor by a small amount of conducting epoxy (Conducting epoxy, CircuitWorks, Inc., Garland, TX). The top of the PVDF film was electrically coupled to the coaxial cable's outer shield with conducting epoxy. A photograph of the probe is shown in figure 5.6.

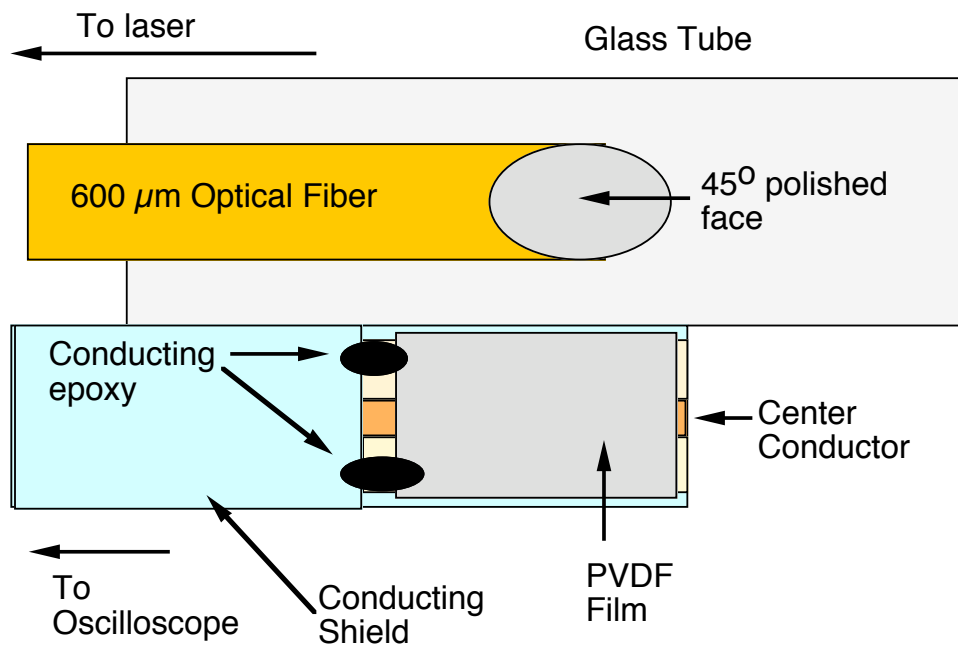


Figure 5.4: The photoacoustic probe is shown here. The 45° polished fiber face directed the laser light in a side firing mode (upwards, out of the plane of the page). The glass tube contained the fiber face and ensured a glass/air interface for proper reflection onto the target. The acoustic detector was positioned alongside the fiber. The detector was composed of a piezoelectric film on a miniature coaxial cable that sent the signal to the oscilloscope.

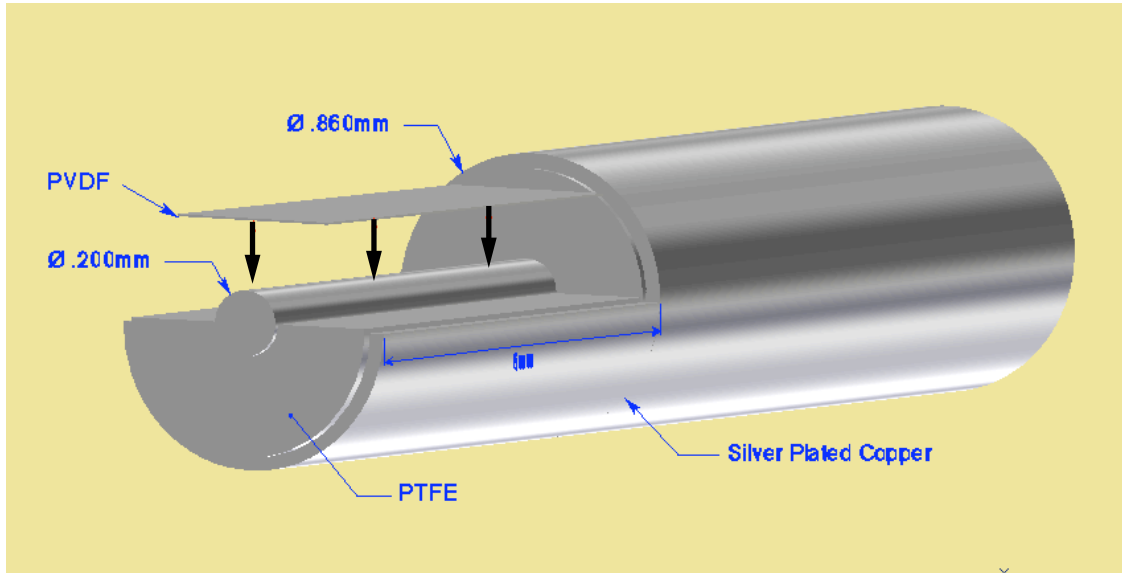


Figure 5.5: The acoustic detector was composed of an aluminized PVDF film in contact with the center conductor of a miniature coaxial cable (860 μm diameter), with the other side electrically connected to the conducting shield of the coaxial cable with conducting epoxy.

5.2.3 Amplification

A noninverting amplifier was built using a surface mount CLC425 ultra low noise, wideband operational amplifier (National Semiconductor, Arlington, TX) [102,103]. The gain–bandwidth product of the op amp was 1.9 GHz. Appropriate resistor values were used in the amplifier circuit to maintain a gain of 45. The circuit board was etched from a copper sheet over a plastic substrate. Conductive traces were designed to minimize RF noise. The circuit is shown in figure 5.7.

5.2.4 Transducer Characteristics

The sensitivity of the acoustic transducer was characterized by irradiating Direct Red solutions of various absorption coefficients with 2.0 mJ of laser light in contact with the active area of the transducer. The relationship [27,69]

$$p(0) = \frac{1}{2}\Gamma\mu_a H_0 \quad (5.2)$$

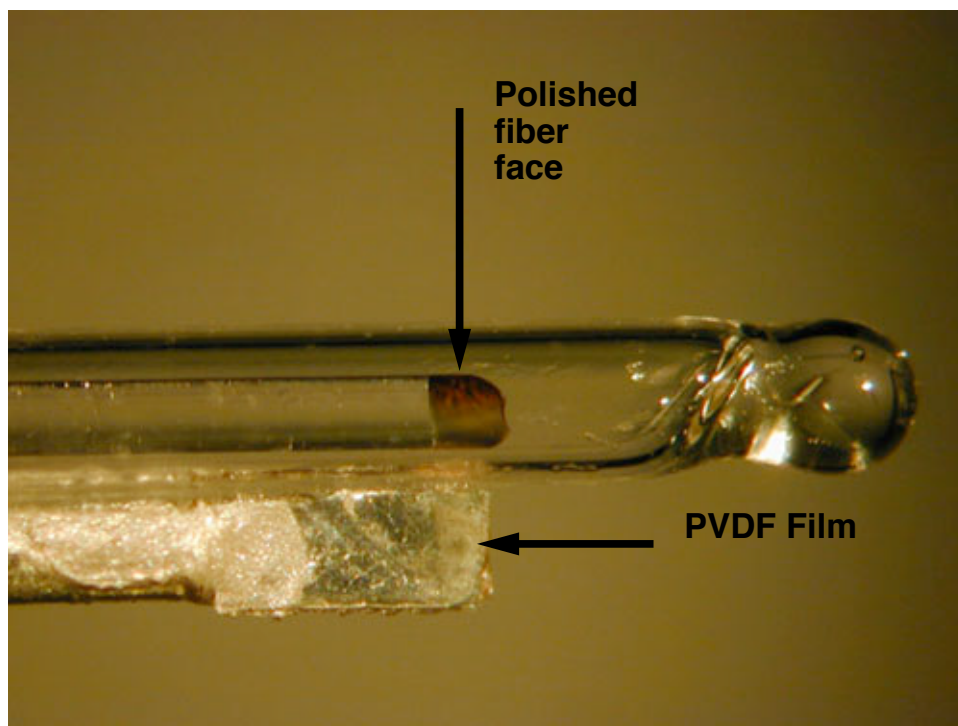


Figure 5.6: The photoacoustic probe is shown here. The total width of the fiber–detector pair is 2.1 mm. The glass tube is rounded at the tip to prevent damage to tissue.

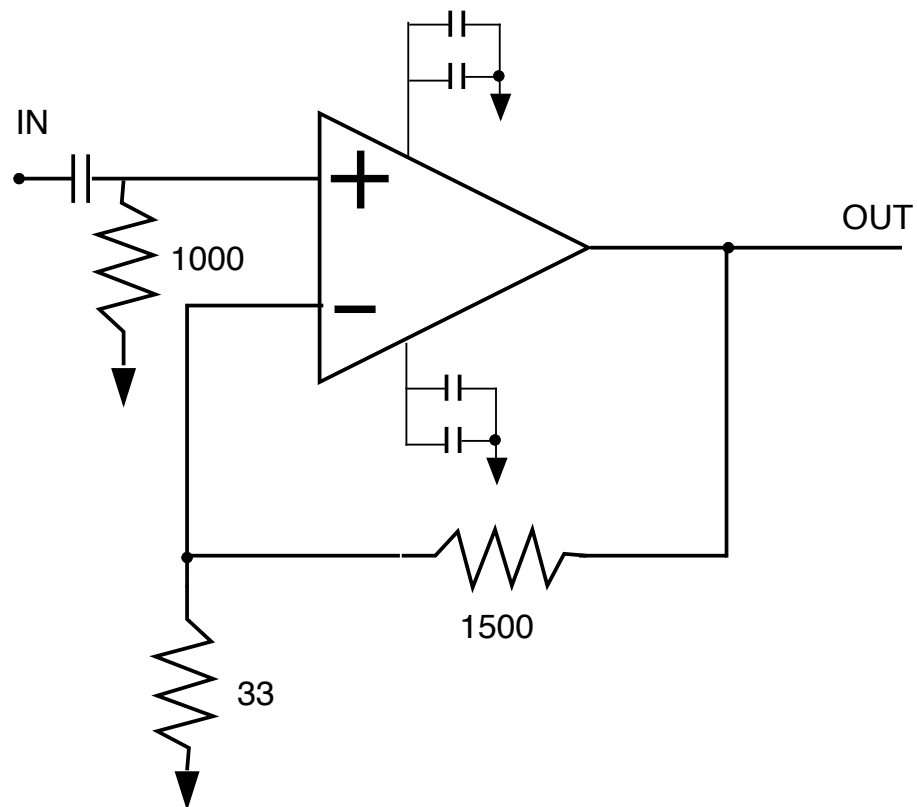


Figure 5.7: The circuit schematic for the operational amplifier is shown here. The operational amplifier was a CLC425 ultra low noise, wideband operational amplifier. The resistor pair, R1 and R2, theoretically provided a gain of 45, though actual resistance values provided a gain of 40.

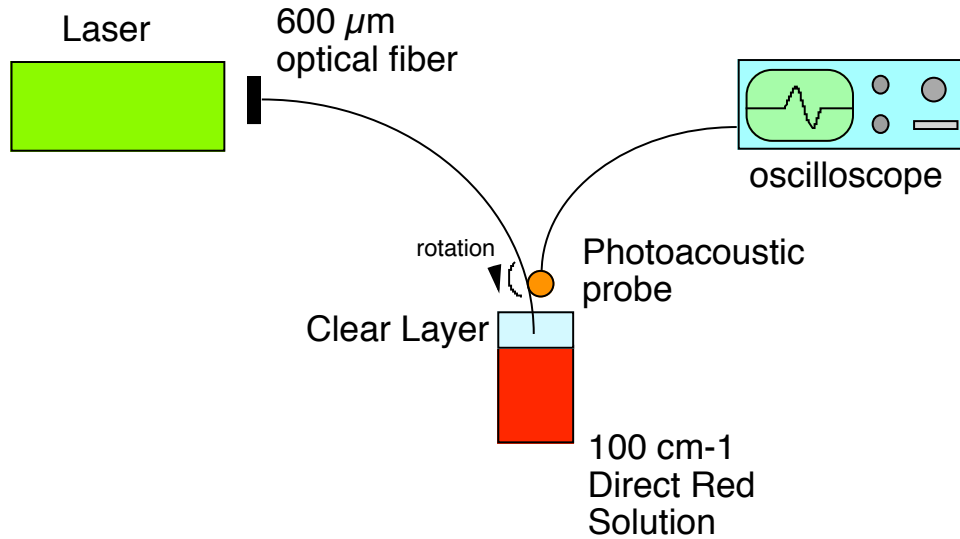


Figure 5.8: The set up for determining the directivity of the detector is shown here. A $600\ \mu\text{m}$ optical fiber irradiated an absorbing solution under clear water. The acoustic detector was positioned above the irradiation site and rotated to determine the detector response as a function of angle.

where $p(0)$ is the pressure of the wave at the surface (point of detection), Γ is the Grüneisen coefficient, here assumed to be 0.12 [27, 69, 77], μ_a is the absorption coefficient of the solution and H_0 is the radiant exposure. The Direct Red solutions had absorption coefficients of 8, 16, 31, and $61\ \text{cm}^{-1}$. The spot sizes were approximately 1 mm in diameter. The radiant exposure was $0.064\ \text{J}/\text{cm}^2$. This gave a temperature rise of less than 1°C , by the relation [82, 104]

$$\Delta T = \frac{\mu_a H_0}{\rho C} \quad (5.3)$$

where ΔT is the change in temperature in degrees Celsius, and ρ is the density and C is the specific heat of the solutions.

The antenna function, or response as a function of angle, of the acoustic transducer was determined by rotating the transducer over an acoustic source. The set up is shown in figure 5.8. The Q-switched laser irradiated a 4 mm spot on a $100\ \text{cm}^{-1}$ Direct Red solution in a cuvette. The acoustic transducer was positioned above the Direct Red solution with a 6 mm layer of clear water. The transducer was rotated with a rotation stage (Rotation

Stage, Thorlabs, Newton, NJ) in 5° increments, from -40° to 40° , where 0° was oriented directly toward the laser spot. The detected acoustic waveforms were averaged over 64 pulses. The acoustic waves were not amplified in this experiment. The acoustic wave amplitudes were measured and plotted to determine the sensitivity of the detector as a function of detection angle.

5.2.5 Acoustic Testing

The photoacoustic probe was tested on tissue phantoms. These tissue phantoms were meant to simulate a necrotic blanched layer of tissue over a perfused layer of esophagus. The phantoms were made with Direct Red 81 (Sigma Chemical, St. Louis, MO) in water. Four solutions were made with absorption coefficients of 8, 16, 30, and 61 cm^{-1} at 532 nm. Assuming an absorption coefficient of 300 cm^{-1} at 532 nm, these absorption coefficients correspond to 3, 6, 10, and 20%, respectively. The solutions were contained in a plastic circular cuvette 20 mm in diameter and 20 mm tall. Cuvettes containing distilled water or 1% Intralipid solutions (Liposyn, Abbott Laboratories, Abbott Park, Illinois) were placed above the cuvette with the red absorbing solution (figure 5.9). The 1% Intralipid solutions were used to simulate the reduced scattering coefficient of the blanched layer of esophagus, which was estimated at 15 cm^{-1} [105]. These cuvettes were 1–8 mm in height, in 1 mm increments. The photoacoustic probe was set in contact with the clear or turbid solutions. The detected acoustic waves were averaged over 32 pulses at a 10 Hz. The signal to noise ratio was calculated as a function of depth for the clear and turbid solutions. The noise was approximated by calculating the standard deviation of 50 points of a signal obtained from irradiating a phantom with no absorber. The noise value used was 2 mV. The signal amplitude was calculated by the peak height of the acoustic signal.

5.2.6 Sound Speed

The speed of sound was calculated in the clear and turbid solutions by tracking the peak of the acoustic pulse as a function of depth. The sound speed was determined as the average of the difference in time between successive 1 mm layers of solution for the depths of 1 mm to 8 mm.

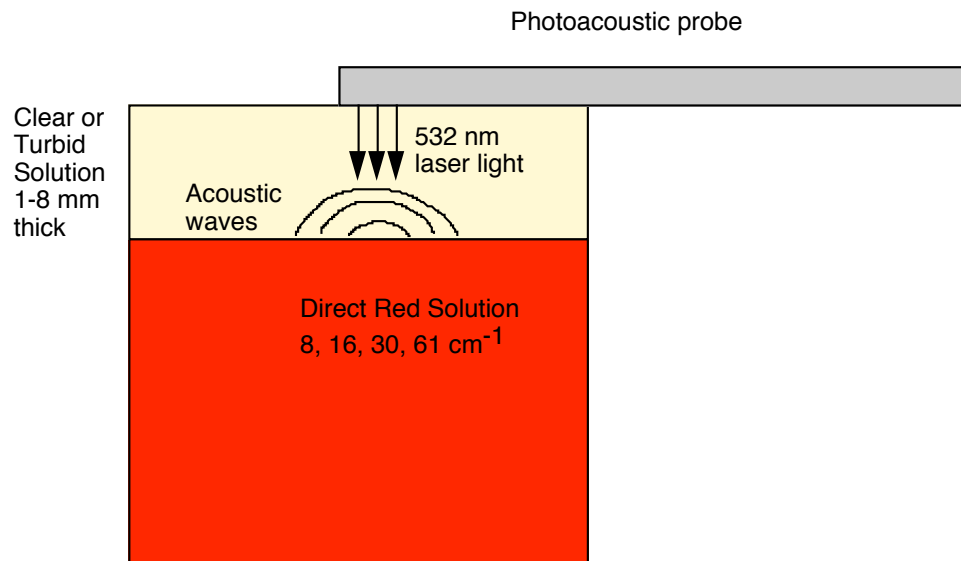


Figure 5.9: The acoustic testing of the photoacoustic probe was performed by irradiating solutions of various absorption coefficients under clear or turbid solutions of various thicknesses. The resulting acoustic waves were detected by the photoacoustic probe and sent to an oscilloscope.

5.2.7 Vein Model Test

An *in vitro* vein model was made using a cylindrical tube filled with Direct Red 81 (Sigma Chemical, St. Louis, MO) solution with an absorption coefficient of 300 cm^{-1} at 532 nm. This absorption coefficient was chosen to simulate the absorption of whole blood with hematocrit of 0.41 [5]. The 12 mm long cylindrical tube was made of Teflon (Zeus Industrial Products, Orangeburg, SC), and had an outer diameter of 1.3 mm. The inner diameter was 0.7 mm. The tube was submerged 3 mm into a scattering solution that had a scattering coefficient of approximately 20 cm^{-1} at 532 nm. This scattering coefficient was chosen to simulate the scattering properties of human skin. A scan with the photoacoustic probe was made across the axis of the cylindrical tube. This scan provided pressure signals from the submerged vein model. The scan was made in 0.8 mm increments. The scan was made over 11.6 mm so that the probe was directly over the submerged tube approximately halfway into the scan.

5.2.8 *In Vivo* Testing

The photoacoustic probe was tested on a human finger of a caucasian male volunteer. The probe was placed above an acrylic sheet of 1 mm thickness that was situated over the finger. The pulse energy was approximately 4 mJ, with a spot size approximately 1 mm in diameter. When the acrylic sheet exerted pressure uniformly over the finger, the tissue achieved a blanched look, becoming more yellow, while blood perfusion, indicated by redness, appeared only at the boundary of the acrylic sheet. The probe measured photoacoustic signals over the perfused and blanched finger. The acrylic sheet, finger, and probe were acoustically coupled with thin water layers of less than 1 mm.

5.3 Results

5.3.1 Transducer Characteristics

The acoustic transducer had a sensitivity of 1.5 mV/bar. The amplifier circuit had an electronic gain of 40, so that amplified signals would have a sensitivity of 60.0 mV/bar.

The transducer antenna function is shown in figure 5.10

5.3.2 Acoustic Testing

The results of the acoustic testing are shown in this section. A montage of the acoustic waveforms for the 60 cm^{-1} absorbing solutions are displayed, with the clear intervening layers in figure 5.11 and the turbid intervening layers in figure 5.12. The depths of intervening layers are 1–8 mm in 1 mm increments. The acoustic wave delay was approximately $0.7\ \mu\text{s}$ between graphs, though a small meniscus contributed to measurement error. The meniscus was approximately 1 mm. For a 1 mm intervening layer, this accounts for 50% of the acoustic delay, though at 8 mm, it only accounts for a 13% of the acoustic delay.

The signal to noise ratios for all four absorption coefficient solutions as a function of depth with clear and turbid intervening layers are shown in figure 5.13 and figure 5.14, respectively.

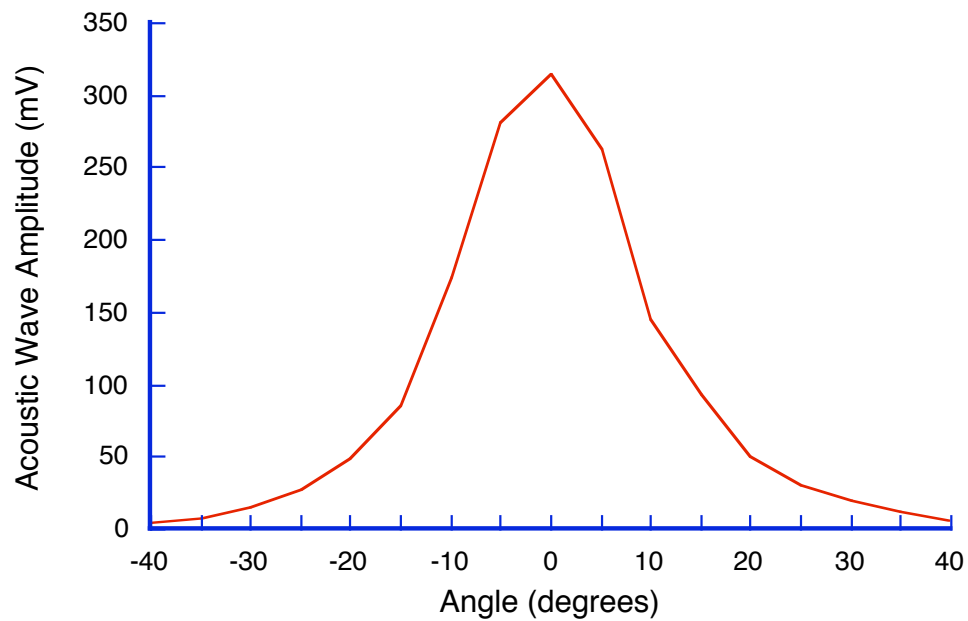


Figure 5.10: The sensitivity of the acoustic transducer is shown here as detector response to plane acoustic wave as a function of angle.

5.3.3 Sound Speed

The sound speed was calculated in each of the experiments for the four absorption coefficients through clear and turbid layers. The result is shown in figure 5.15. All sound speeds were within 4% of $1.5 \text{ mm}/\mu\text{s}$.

5.3.4 Vein Model Test

A typical acoustic waveform is shown in figure 5.16. This waveform was taken at the 7th scan position, directly above the absorbing tube.

The result of the vein model test is shown in figure 5.17. The circle indicates the position of the vein determined by the initial acoustic wave peak. The initial peak was taken as the top surface of the vein model.

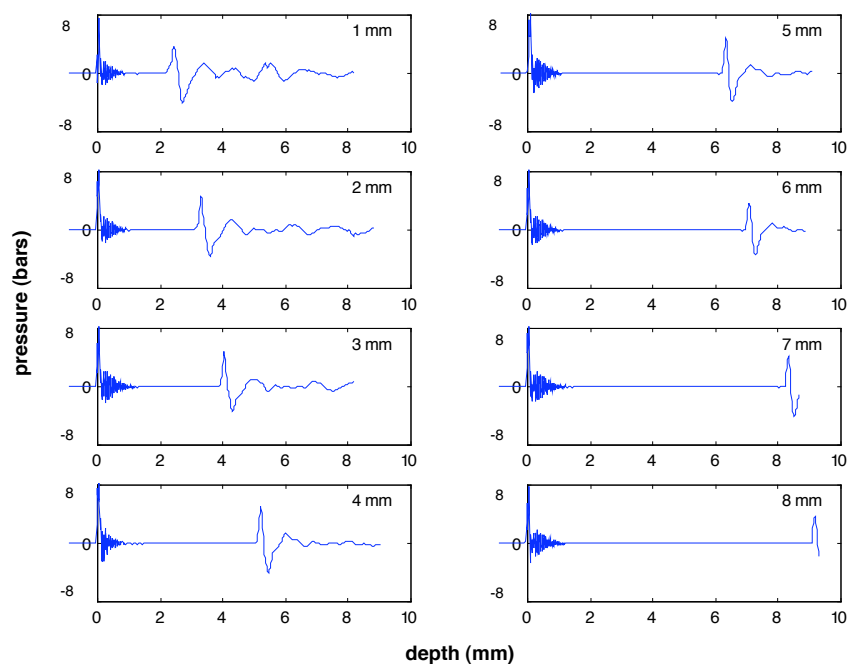


Figure 5.11: The acoustic waves resulting from irradiating a Direct Red solution ($\mu_a = 60 \text{ cm}^{-1}$) with various thicknesses (1–8 mm) of clear water between the absorbing solution and the detector. The signal, easily discernible from the noise level, was delayed as the clear layers become thicker. Zero on the horizontal axis indicates the laser pulse trigger.

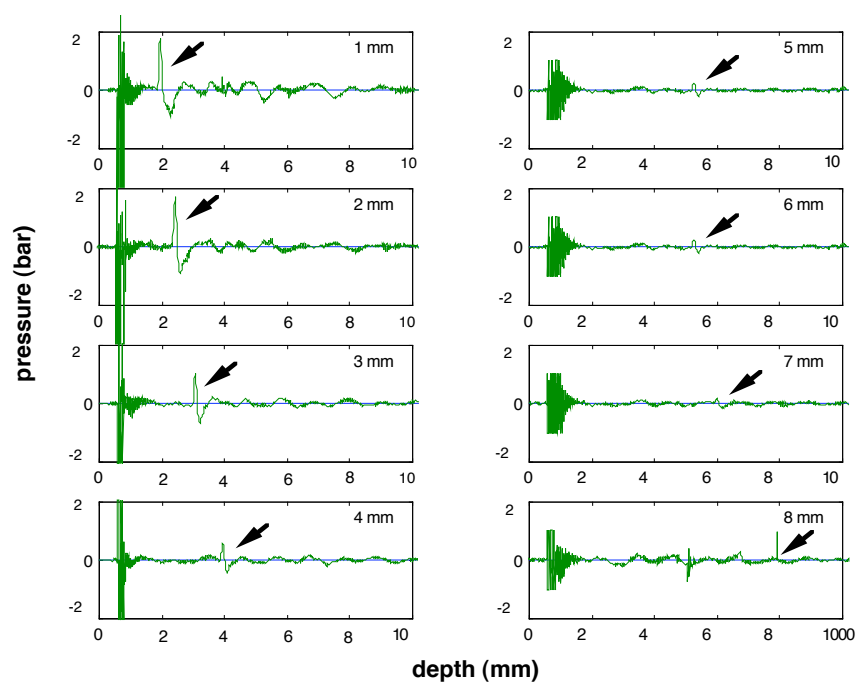


Figure 5.12: The acoustic waves resulting from irradiating a Direct Red solution ($\mu_a = 60 \text{ cm}^{-1}$) with various thicknesses (1–8 mm) of turbid solution ($\mu_s \doteq 15 \text{ cm}^{-1}$) between the absorbing solution and the detector. The signal, easily discernable from the noise level, was delayed as the turbid layers become thicker.

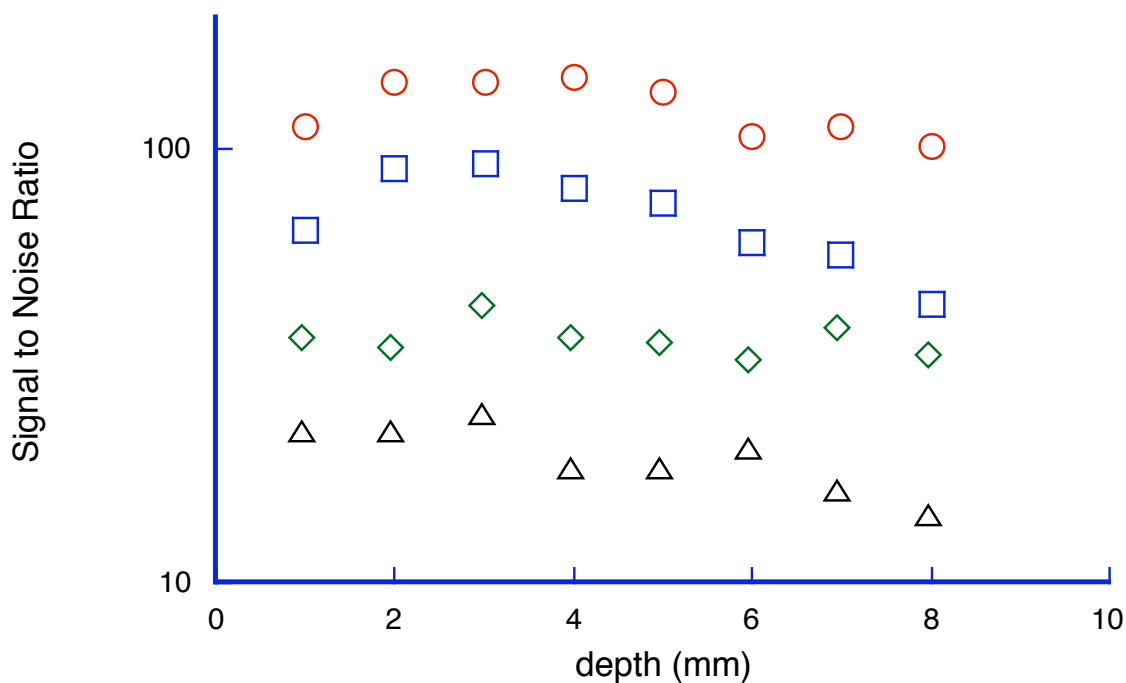


Figure 5.13: The signal to noise ratios for the solutions of various absorption coefficient are shown as a function of depth of clear layer. The maximum signal occurred at 3–4 mm of depth, due to the offset of the acoustic detector from the optical fiber. This offset caused the acoustic wave source to be not directly underneath the detector, decreasing the detector sensitivity. The acoustic signal maximized at about 3–4 mm away, as the resultant larger spot created acoustic waves directly beneath the detector. For greater than 4 mm, the lower radiant exposure dominated the the acoustic signal generation, resulting in a weaker acoustic detection.

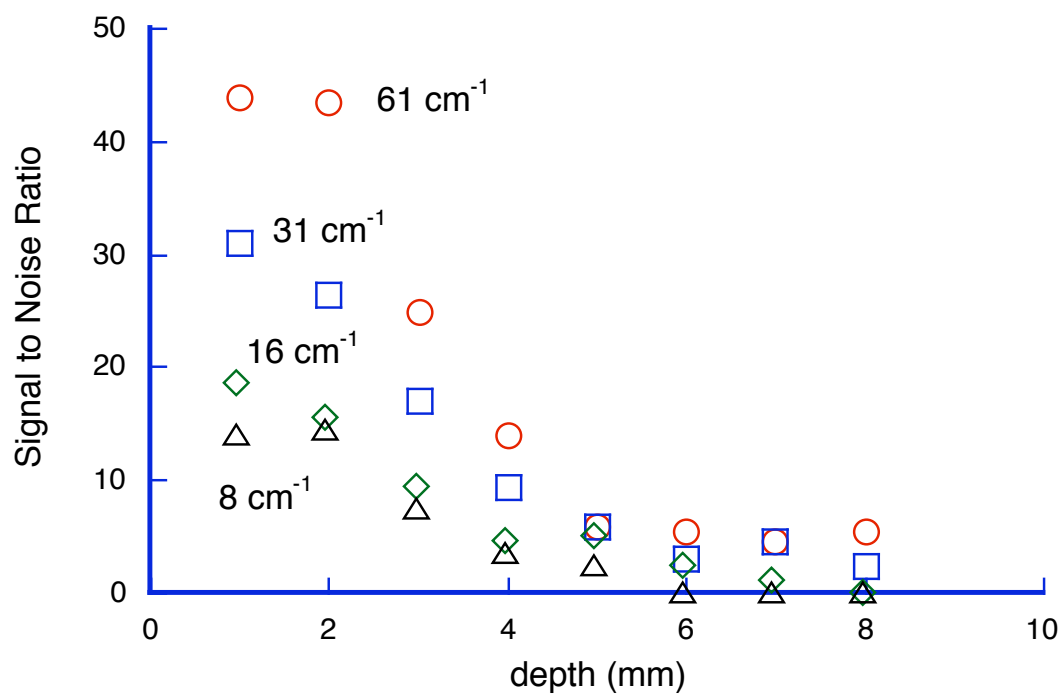


Figure 5.14: The signal to noise ratios for the solutions of various absorption coefficient are shown as a function of depth of turbid layer. The maximum signal occurred at 1 mm, as the highest radiant exposure occurred and optical diffusion was stronger at greater distances, decreasing the acoustic signal strength.

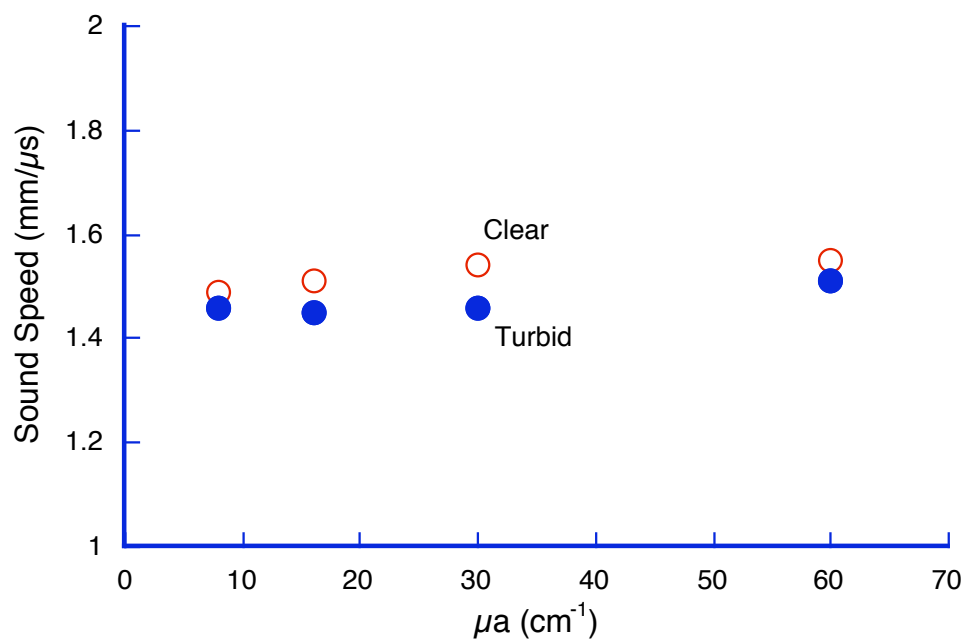


Figure 5.15: The calculated sound speeds through clear and turbid layers are shown here. All are within 4% of $1.5 \text{ mm}/\mu\text{s}$.

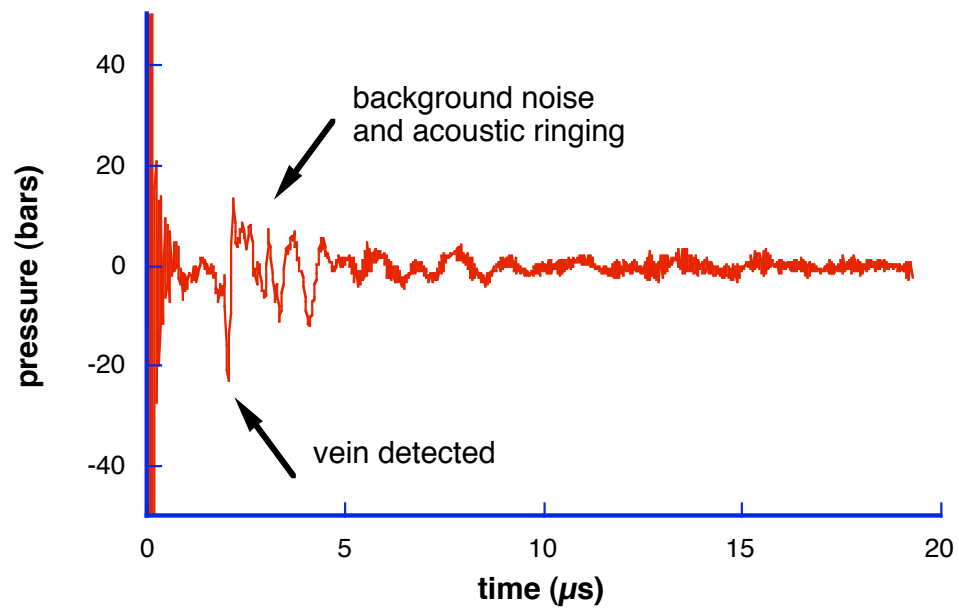


Figure 5.16: This is the acoustic wave on the 7th of 15 scans on the vein model. The vein model was directly underneath the detector on this scan. The initial peak indicates the detected vein model and the propagation time, though several following peaks occur.

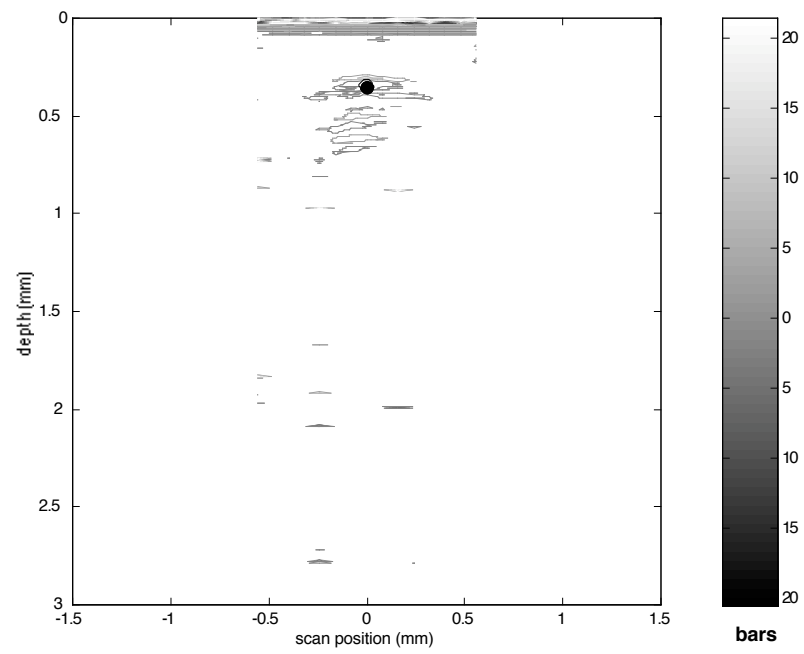


Figure 5.17: A localization map of the vein model was constructed using all 15 scans. The result is a map showing the vein model in depth and scan position. The small circle, superimposed onto the first region of acoustic energy, indicates the vein model position.

5.3.5 *In Vivo* Testing

The acoustic waves resulting from irradiation of the perfused and less perfused finger are shown in figure 5.18.

5.4 Discussion

5.4.1 Photoacoustic Propagation Time

The concept of propagation time is simple, assuming a constant sound speed to calculate a distance based on the time of arrival of an acoustic wave. The assumption of sound speed in tissue-like media as $1.5 \text{ mm}/\mu\text{s}$ is valid for water, milk, fat, nerve tissue, muscle, etc [70,72,74,106]. The situation for a post-treatment esophagus, however, is aggravated by the complex geometry caused by uneven uptake of photosensitizer, treatment light distribution, or other factors. These factors, though not affecting sound speed, would change the propagation path, making the distance calculation inaccurate. The geometry of the post-treatment esophagus may not be planar, nor even a reasonable approximation of one. Repeated measurements and systematic scans may smooth these inhomogenous effects by integrating the bumps in an otherwise smooth heating distribution which creates the photoacoustic field.

5.4.2 Amplification

The amplifier used in these experiments was a simple non-inverting instrumentation amplifier. The gain was chosen so that the gain-bandwidth product of 1.9 GHz would allow a good response up to about 50 MHz. The input impedance of the amplifier was $1 \text{ k}\Omega$, which was not optimal for integration of the charge from the PVDF transducer. The PVDF film had a capacitance of about 100 pF . This capacitance with $1 \text{ k}\Omega$ results in a time constant of 100 ns . Thus any acoustic measurement of greater than four or five such time constants would lose charge, resulting in an inaccurate pressure measurement. The result is that the incoming waveform was a transition between a charge measurement and a pressure measurement. While this has little effect on the propagation time, any attempt to derive optical properties from the pressure signal, or integration of the pressure signal

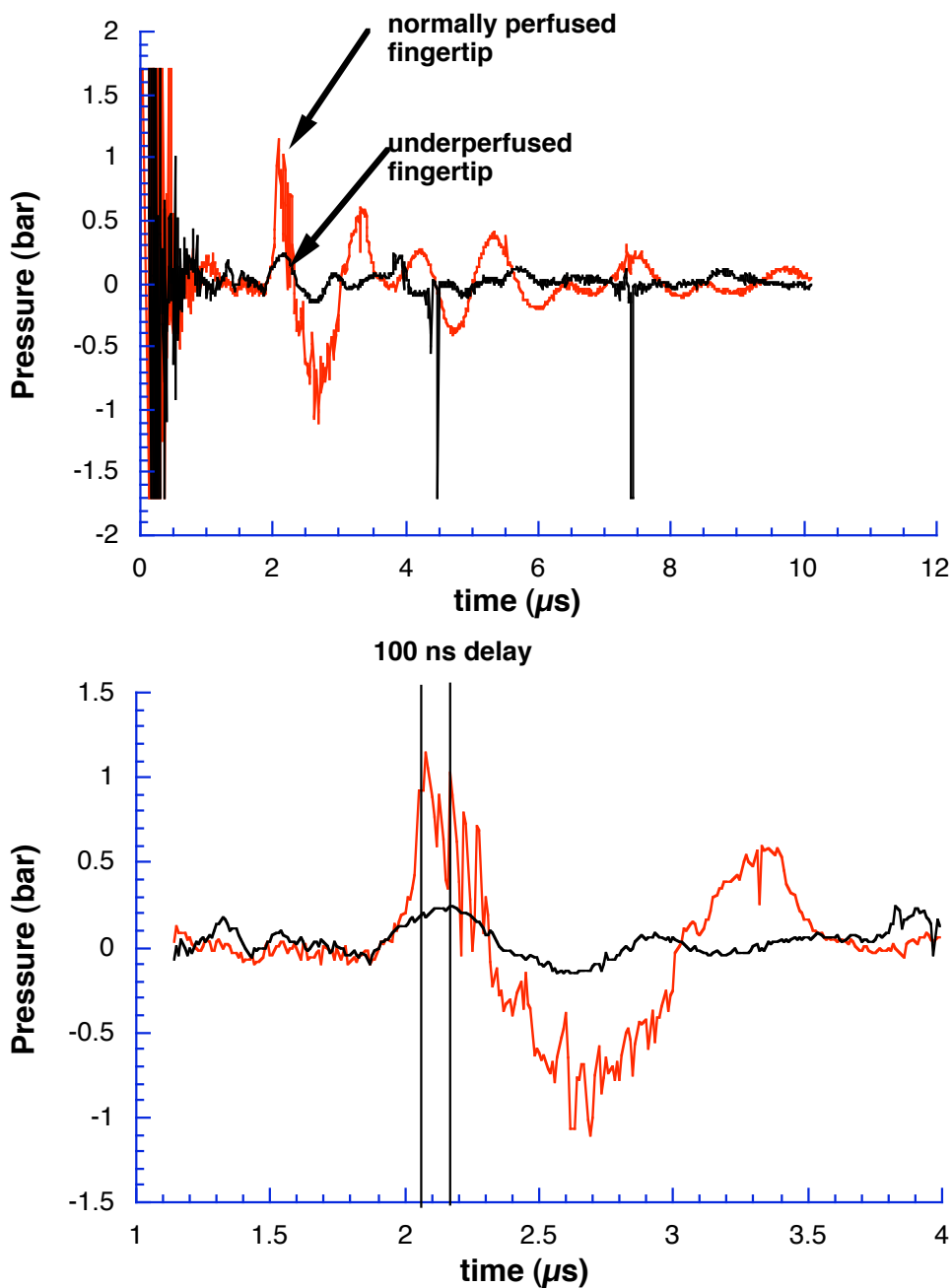


Figure 5.18: The top graph shows the acoustic waves from the normally perfused and underperfused finger tip. The acoustic signal from the normally perfused fingertip (red) is greater in amplitude than the underperfused fingertip (blue), and the peak of the underperfused fingertip appears to be delayed by about 100 ns, corresponding to $150 \mu\text{m}$ (lower graph). The peak times are indicated by the vertical bars. The amount of ringing and noise from the transducer prevent precise analysis of layered structures, though the discrimination of the two perfusion levels is evident by a factor of four difference in acoustic amplitude. A 3 mm water layer separated the fingertip from the acoustic detector, accounting for the $2 \mu\text{s}$ delay in the signals.

for a velocity potential, must be considered an inaccurate measurement with regard to amplitude, though not for propagation time. As all methods in these experiments use only propagation time, the shape of the acoustic waveform was neglected. The results of the propagation time and sound speed showed that the methods used were satisfactory for determining the depth of the intervening, nonabsorbing layers.

5.4.3 Acoustic Testing

The results of the acoustic wave generation in the 8, 16, 31, and 61 cm^{-1} absorption coefficient solutions with clear intervening layers showed signal to noise (SNR) ratios as high as 150. In the 16, 31 and 61 cm^{-1} solutions, the SNR was greatest for the 3 and 4 mm layers. The 8 cm^{-1} solutions were much lower than the others. The greatest SNR occurring at 3 or 4 mm is explained by the fact that at 1 and 2 mm, the PVDF film is not directly over the laser spot, as the distance from the fiber to spot is comparable to the separation distance of the fiber and the PVDF film (figure 5.19). The drop off in SNR after 4 mm is due to decrease in radiant exposure, due to spot size increase and acoustic attenuation. The SNR's shown in the turbid layers didn't show the high SNR behavior at 3 or 4 mm since the light was diffuse, causing the laser spots to be larger and encompassing the region below the fiber and detector.

The turbid solutions were a better model of the esophagous, as the blanched layer in the post-treatment esophagous is scattering. Assuming a whole blood optical absorption of 300 cm^{-1} at 532 nm, the 8, 16, 31, and 61 cm^{-1} solutions represented perfusions of 3, 5, 10, and 20%, respectively. A perfusion of 5–10% is reasonable for elevated perfusion levels in cancerous tissue, so detection of perfused layers in the esophagous may occur in as deep as 7-8 mm, with an SNR of 4 or higher, neglected other factors such as high background absorption or nonplanar geometry. Even with a 3% perfusion, detection may occur to 4 or 5 mm.

5.4.4 Sound Speed

The sound speed derived averaged to $1.52 \pm 0.03 \text{ mm}/\mu\text{s}$ for the clear water and $1.47 \text{ mm}/\mu\text{s}$ for the turbid solution. The inherent error in the turbid measurements were

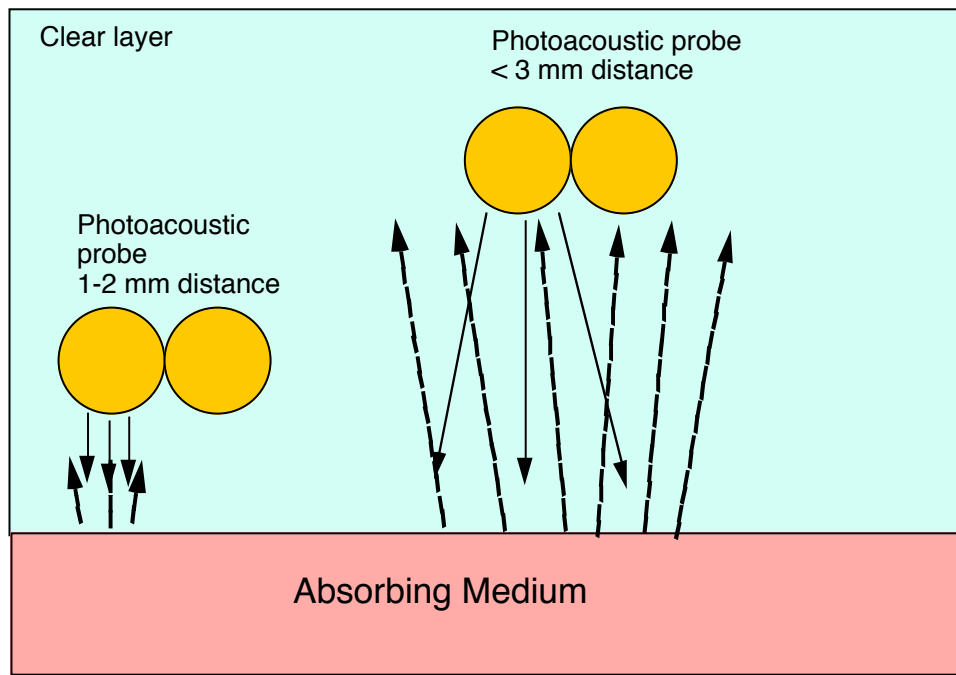


Figure 5.19: For the clear intervening layer, the acoustic signal for distances of 1-2 mm is weaker than signals detected at 3-5 mm, as the acoustic sensor is not directly over the acoustic source when the probe is so close. This is due to the antenna function of the probe and the small spot size. After about 5 mm, the decreased radiant exposure results in a weaker acoustic wave, making the detected signal weaker.

primarily a result of low signal to noise ratio in the deeper measurements, making an accurate pinpoint of the acoustic peak difficult. The process was robust enough so that the two measurements were within 4% of the value of pure water, $1.481 \text{ mm}/\mu\text{s}$ at 20°C [67].

5.4.5 Vein Model

While the photoacoustic probe wasn't designed for blood vessel imaging, its compact size and sensitivity made it an obvious candidate for an endoscopic imaging device. The probe was designed to be endoscopic, making imaging during endoscopic procedures a possibility. The small active area and the antenna function of the transducer made it directional, though the laser pulse, while not omni-directional, loses its localization quickly in turbid media.

5.4.6 *In Vivo* Testing

The blanching of the finger tip was an *in vivo* model of the esophagous. The discrimination of blanched and unblanched finger tips was indicated by an acoustic amplitude ratio of 4:1. The results of the phantom tests in conjunction with the finger tip models indicate that the photoacoustic probe may provide depth information for the clinician in the post-treatment environment. This test indicated a possible $150 \mu\text{m}$ layer of nonperfused skin in the finger in the underperfused case, corresponding to a $100 \mu\text{s}$ delay. The environment in the esophageal case, however, can be more complicated, making the task of probing the post-treatment esophagous a greater challenge.

5.4.7 Probe Design

The requirements for the photoacoustic probe were that it be small enough to fit into a 2.7 mm endoscopic channel, sturdy enough that it wouldn't disintegrate during an endoscopic procedure, and sensitive enough to detect perfusion layers under several millimeters of blanched tissue. The current probe design satisfies all counts, as shown in the previous discussion. The final probe was a culmination of a considerable amount of design and testing of prototypes that failed on one or more of the probe criteria. Earlier designs incorporated an acrylic cylinder housing the fiber tip, with a PVDF film attached to the

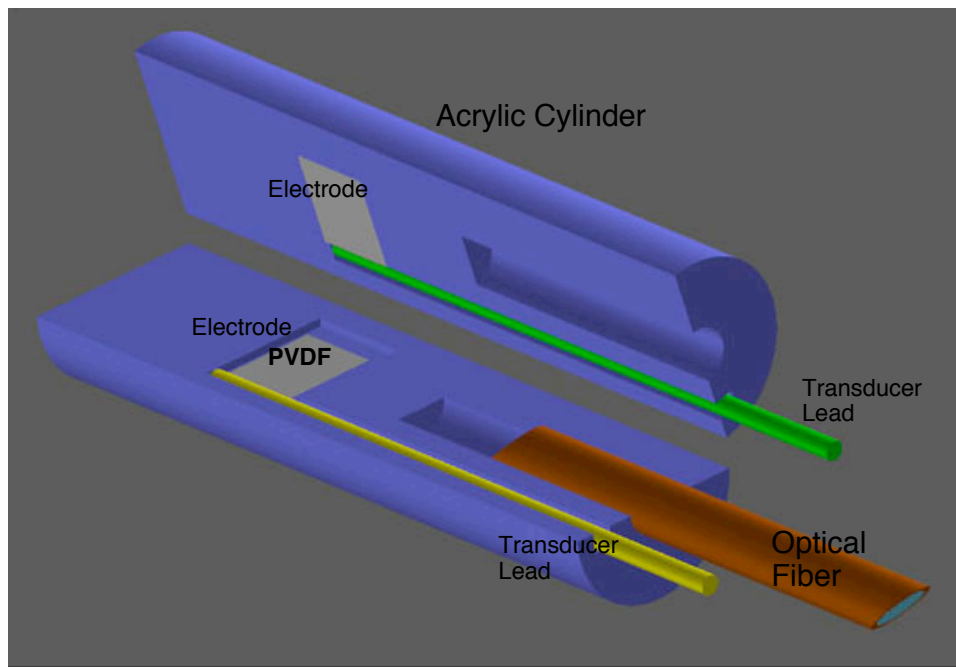


Figure 5.20: Earlier versions of the photoacoustic probe were made from acrylic cylinders housing a side firing optical fiber and a PVDF film between two electrodes. The acrylic cylinder wasn't optically clear enough after machining. At such small dimensions, the acrylic was weak and unsuitable for a robust photoacoustic probe.

surface. One example is shown in figure 5.20. These acrylic designs were not optically clear, since machining of the fiber channel caused frosting of the optical path. Building the acoustic detector was problematic in the connection of small electrodes to the PVDF film. Attempts to create electrical connections between the PVDF film and the electrodes included directly adhering wires to the aluminum on the film with epoxy, connecting aluminum foil to the electrodes and using the foil as the capacitive surface of non-aluminized PVDF and finally, a spring connection between the aluminum capacitive surface of the PVDF and the electrodes. All of these attempts failed. The reasons for the failures included inability to get a good cure on the epoxy, tearing of the aluminum foil, and difficulty in maintaining quality control for such small connections. In addition to the electrical connection problems, the acrylic itself, being about 2 mm in diameter and containing channels and grooves, was too weak to be used clinically. The final probe was

strong, as the PVDF substrate was a single length of coaxial cable and the optical path glass and air.

5.5 Conclusions

The photoacoustic probe described in this chapter is a small, durable, sensitive device suitable for use in an endoscope. The sensitivity shown by the turbid tissue phantoms showed that the perfused layers may be detected to 5 mm or greater under good conditions. Detecting perfused layers under lesser depths of necrotic layer may be possible under conditions of high background absorption or nonplanar optical absorption. An *in vivo* test of a finger tip showed a 4:1 discrimination in normally perfused and underperfused tissue, showing an ability to detect perfusion, though admittedly in a controlled manner with a quasi-planar geometry. The probe may also have application in photoacoustic imaging, as shown by the vein model mapping. The ability to deploy this device endoscopically makes its application extend to the many endoscopic procedures performed clinically.

Chapter 6

General discussion and conclusions

This dissertation has presented a theoretical framework for certain geometries encountered in biomedical photoacoustics, adapted from classical acoustical theory, and has demonstrated experimental results of several photoacoustic applications. The parameters in broadband photoacoustic pulse propagation in tissue phantoms, including attenuation, dispersion, and diffraction were shown in chapter two. A method for depth profiling of optical absorption in dyed acrylamide gels and a stained elastin biomaterial was developed in chapter three. Chapter four showed an investigation of spherical photoacoustic sources in turbid media. Absorbing spheres embedded in clear and turbid acrylamide gels were irradiated with a stress confined laser pulse, generating photoacoustic waves. These waves were analyzed, giving sphere size and location. Additionally, a dipole photoacoustic source was irradiated, showing minimum center to center distances for discrimination between the two sources. Finally, chapter five detailed the design, construction, and testing of a photoacoustic probe for use in an endoscopic procedure for determining treatment depth after photodynamic therapy in esophageal cancer. The probe was ready for clinical testing.

6.1 Broadband Photoacoustic Pulse Propagation in Tissue

This preliminary chapter presented standard acoustical theory and applied it to certain geometries found in biomedical photoacoustics, particularly the planar deposition of laser energy on a circular spot. This situation was modeled as a baffled, piston acoustical source. Axial attenuation was modeled and verified with experiment for 25, 50, 100, and 200 cm^{-1} Direct Red solutions. The experimental attenuation results were matched to

the theoretical model. Diffraction of a piston source was stated as the interference of the plane wave, from the circular spot, and the boundary wave, from the circumferential wall of the disk of irradiation. The disk thickness was equal to the absorption depth. An optical method of acoustic detection was used in order to discriminate between the plane and boundary wave. The progression of the boundary wave into the plane wave was documented graphically, resulting in a diffracted acoustic pulse, when the disk diameter to thickness ratio was less than 10:1.

Dispersion of the photoacoustic pulses was measured by looking at the frequency spectrum of a diffraction free sample. Diffraction was minimized by ensuring the disk of irradiation diameter was much greater than the thickness. This constraint was ensured by using a 200 cm^{-1} absorbing solution, making the absorption depth, and hence the disk thickness, $50\text{ }\mu\text{m}$. With a laser spot of 5 mm , the ratio was 100:1. The spectrum was displayed for acoustic propagation distances of $0.4\text{-}3.4\text{ cm}$. The results showed minimal dispersion at these propagation distances.

Finally, the use of Direct Red solutions as tissue phantoms for these experiments was justified by showing the similarity of acoustic impedance for various tissues and water. The density and sound speeds were all within 5%, making the impedance difference minimal, justifying the use of a Direct Red solution tissue phantom.

Although there was correlation between the theory and experiment, actual clinical relevance of the piston geometry may be questionable. The piston source exist in planar geometries, which would only exist in certain regimes of biomedical treatments. Either the irradiated spot must be small, in which case acoustic diffraction would need to be considered, or the irradiated spot would be a departure from the planar geometry. Thus the model must be modified or the shortcoming must be acknowledged.

Furthermore, the justification of the Direct Red solutions is valid only for plane wave analysis, as the acoustic impedance is equal to the product of the density and sound speed only for plane waves. If the waves are spherical or otherwise, the geometry must be taken into account for determination of the acoustic impedance. Also, acoustic impedance is not the only factor in acoustic propagation. Particularly in nonlinear cases, a more sophisticated model must be developed and for acoustic propagation studies.

6.2 Depth profiling of absorbing soft materials using photoacoustic methods

Depth profiling of tissue and tissue-like media that are dominated by optical absorption is a successful application of photoacoustics. The algorithm in chapter 3 was used to determine the optical absorption coefficient of acrylamide gels and a stained elastin sheet. The resolution of the measurement and calculation was about $10\ \mu\text{m}$, though this limitation was probably primarily due to laser pulse duration. The product of the pulse duration and sound speed gives a theoretical limit to the layer resolution, so a sub-nanosecond pulse with enough energy may increase the layer resolution even further, though a test of the limit is difficult, as a gel phantom with layers thinner than $70\ \mu\text{m}$ could not be made with the method used in this chapter. For applications such as laser-tissue welding where biomaterials are stained with Indocyanine Green (ICG), the absorption must be high, as the welding process is thermal. In such situations, absorption would dominate scattering, making the depth profiling method a tool in understanding the thermal profile of the welding process, in turn giving insight into the welding mechanism, which is currently unknown.

While the technique was successfully demonstrated, the process depends on the dominance of absorption in the light-tissue interaction. In cases where absorption is low, the exponential curve fitting becomes more difficult. In fact, absorption coefficients of less than $10\ \text{cm}^{-1}$ often give erroneous fits. Unfortunately, for very high absorptions, nonlinear effects may occur, in which case all of the modeling presented falls short. So absorption coefficients of $10\text{--}300\ \text{cm}^{-1}$ may be the acceptable range for this method. One must also worry about divergence in the algorithm presented. The positive exponential term in the algorithm for determining μ_a makes the calculated values blow up, so noise must be limited for effective absorption reconstruction.

6.3 Localization of spherical photoacoustic sources in acrylamide gel phantoms using time domain measurements

This chapter constituted a substantial part of the experimental work. A spherical shell model was developed to describe photoacoustic generation in an optically thick sphere. This model provided a means for calculating the beam profile of a spherical shell source and showed that the beam pattern was similar to a plane piston. Thermoelastic modeling was used to simulate acoustic waves from spherical sources. A backprojection algorithm was developed to take photoacoustic signals from an optically thick sphere embedded in clear and turbid acrylamide phantoms and determine the sphere locations. The resulting image plot revealed sphere sources to within 5% of the true location. The simulations were also backprojected into an image plot. Sources near reflecting boundaries were backprojected and the image sources showed up as virtual sources outside of the gel phantom. Acoustic wave shape was analyzed and related to the geometry of the optical absorption in the sphere. Sphere size was determined from the acoustic wave using a simple geometric model. Finally, dipole sources of optically thick spheres were irradiated and a minimum separation distance was determined.

The localization algorithm, a multiplicative backprojection scheme, successfully located optically thick spherical sources in turbid gels. The technique has yet to be successfully tested *in vivo*. Though there was background absorption in the gels, the case of living tissue is much more complex than a homogenous turbid medium. Stress confined irradiation of a turbid medium with a background absorption with an embedded absorber creates photoacoustic sources in the embedded absorber and in the medium itself, decreasing the contrast between the two. While it may be possible to minimize the background interference by subtracting the signal obtained by irradiating the medium in the absence of an embedded absorber, this technique is not practical clinically, as a pure background signal may not be available, and a background phantom will not necessarily be accurate with respect to tissue optical properties.

6.4 Design and testing of an endoscopic photoacoustic probe for determining treatment depth after photodynamic therapy of esophageal cancer

An endoscopic probe was designed and developed for the purpose of inducing photoacoustic waves in PDT treated esophageal lumens. The acoustic wave propagation time would be used to determine the depth of treatment from PDT. The probe was made from a 600 μm , side-firing optical fiber, which delivered the stress confined laser pulses and a 890 μm semi-rigid, coaxial cable with a PVDF film transducer attached to the tip. The PVDF sensor was oriented to detect returning acoustic waves from the side-fired laser pulses. The optical fiber and coaxial cable were attached alongside each other. The probe was tested on clear and turbid tissue phantoms and the SNR was determined for 8, 16, 31, and 60 cm^{-1} absorbing layers. An SNR of over 3 was achieved for the 8 cm^{-1} layer under 5–6 mm of a 20 cm^{-1} scattering layer. The probe was also tested to image a vein model in a scattering solution. The probe was also used to determine the depth of a denatured layer of liver *in vitro*. Finally, the probe was used to discriminate between various perfusion states of a human fingertip *in vivo*.

The problems associated with probing an complex, optically turbid medium, as discussed in the previous section, also exist in this application. The testing on turbid layers showed that signals attenuated much more quickly than in the clear case, where signal strength dropped by a factor of five even with 1 mm of intervening layer between the probe and the planar absorber. The problems are aggravated in the esophagus by the nonplanar geometry, which may be manifested by bulbous tumor growth and curves in the esophageal lumen. Additionally, the blanching effect, which is the basis of the depth profiling technique, may not be consistent, where treated areas may manifest swelling and redness, masking the PDT treatment. The depth profiling method may still detect changes in the optical properties of the treated area, though not in the ideal manner of determining blanched layer thickness.

6.5 Conclusions

The use of photoacoustics in biomedical applications can be superficially described as a blending of optical and ultrasound methods in diagnostic applications. The availability and safety of optical sources, being non-ionizing radiation, are advantages of optical diagnostics over radiographic methods in medicine. Unlike radiographic or nuclear medicine techniques, the main hazard of optical sources is ocular damage, which is easily obviated by standard eye protection. Unfortunately, the ability for light to propagate in tissue is hampered by the scattering nature of tissue, making probing, particularly in imaging applications, difficult beyond a few millimeters. In photoacoustics, since regions of tissue become acoustic sources themselves, the propagation distances are extended to the centimeter regime. Unlike conventional ultrasound, where imaging contrast results from small differences in acoustic impedance of tissue regions, the tissue of interest is the acoustic source itself, maximizing the contrast between it and the surrounding tissue. Additionally, optical diagnostic methods may be used in conjunction with photoacoustic methods, such as coupling a pair of optical fibers to an acoustic transducer (figure 6.1).

A laser pulse can be delivered via one optical fiber to induce an acoustic wave, while simultaneously sending white light via the same fiber. The second fiber can collect reflectance measurements, while the acoustic transducer detects the resultant acoustic wave. Thus an immediate sampling of superficial optical properties can be gained, with photoacoustic information supplementing it.

Photoacoustics extends the use of medical lasers as diagnostic tools, in some cases overcoming the difficulties of optical scattering, while possibly providing a safe, effective means for probing a tissue environment. It is the aim of this dissertation to extend the knowledge and practical use of this fundamental interaction of light and tissue.

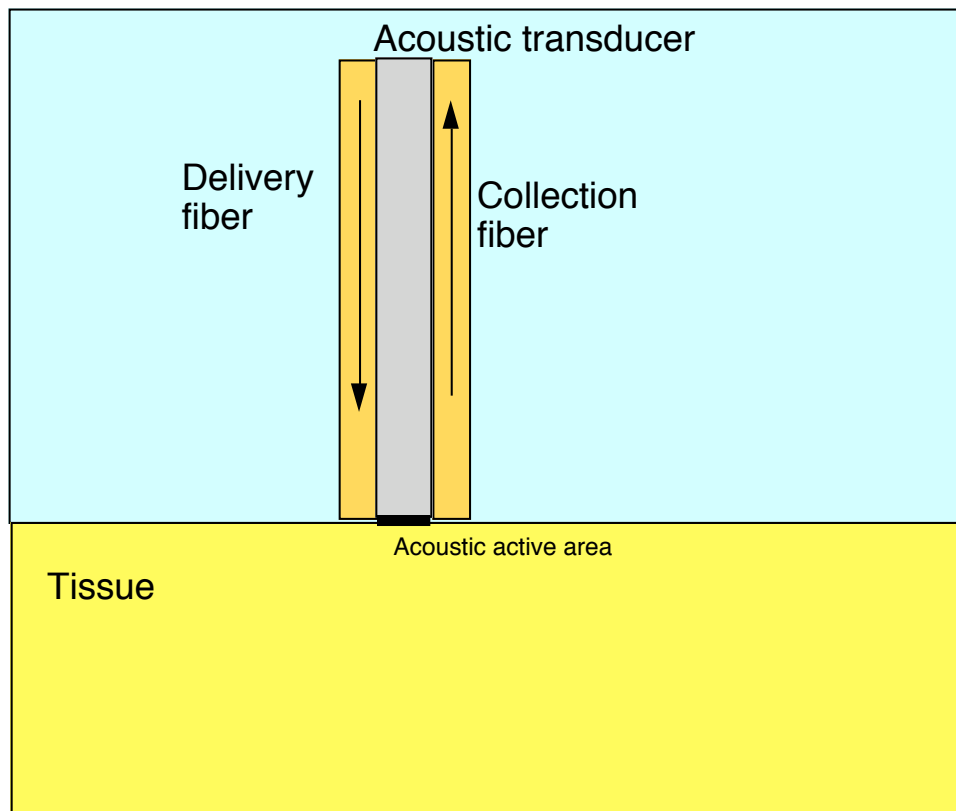


Figure 6.1: A scheme for combining optical and acoustic diagnostic methods. A delivery fiber is used to introduce a stress confined heating in tissue with a fast laser pulse, while simultaneously delivering white light. A collection fiber detects reflectance from the white light for optical property determination. The acoustic transducer detects the resultant acoustic wave from the fast laser pulse.

Bibliography

- [1] A. B. Bell, “On the production and reproduction of sound by light,” *Am. J. Sci.*, vol. 20, p. 305, 1880.
- [2] W. C. Roentgen *Philos. Mag.*, vol. 11, p. 308, 1881.
- [3] R. G. Brewer and K. E. Rieckhoff, “Stimulated brillouin scattering in liquids,” *Phys. Rev. Lett.*, vol. 13, p. 334a, 1964.
- [4] V. E. Gusev and A. A. Karabutov, *Laser Optoacoustics*. AIP Press, 1993.
- [5] W. F. Cheong, “Appendix to chapter 8: Summary of optical properties,” in *Optical–Thermal Response of Laser–Irradiated Tissue* (A. J. Welch and M. J. C. van Gemert, eds.), pp. 275–303, New York: Plenum Press, 1995.
- [6] A. Rosencwaig, *Photoacoustics and Photoacoustic Spectroscopy*. John Wiley & Sons, Inc, 1980.
- [7] M. W. Sigrist, “Laser generation of acoustic waves in liquids and gases,” *J. Appl. Phys.*, vol. 60, pp. R83–121, 1986.
- [8] W. P. Arnott, H. Moosmüller, R. E. Abbott, and M. D. Ossofsky, “Thermoacoustic enhancement of photoacoustic spectroscopy: Theory and measurements of the signal to noise ratio,” *Rev. Sci. Instrum.*, vol. 66, pp. 4827–4833, 1995.
- [9] D. P. Hand, S. Freeborn, P. Hodgson, T. A. Carolan, K. M. Quan, H. A. MacKenzie, and J. D. C. Jones, “Optical fiber interferometry for photoacoustic spectroscopy in liquids,” *Optics Lett.*, vol. 20, pp. 213–215, 1995.
- [10] P. C. Beard and T. N. Mills, “Characterization of *post mortem* arterial tissue using time–resolved photoacoustic spectroscopy at 436, 461, and 532 nm,” *Phys. Med. Biol.*, vol. 42, pp. 177–197, 1997.
- [11] G. J. Diebold and P. J. Westervelt, “The photoacoustic effect generated by a spherical droplet in a fluid,” *J. Acoust. Soc. Am.*, vol. 84, pp. 2245–2251, 1988.

- [12] G. J. Diebold, M. I. Khan, and S. M. Park, "Photoacoustic "signatures" of particulate matter: Optical production of acoustic monopole radiation," *Science*, vol. 250, pp. 101–104, 1990.
- [13] G. J. Diebold, T. Sun, and M. I. Khan, "Photoacoustic monopole radiation in one, two, and three dimensions," *Phys. Rev. Lett.*, vol. 67, pp. 3384–3387, 1991.
- [14] M. I. Khan, T. Sun, and G. J. Diebold, "Photoacoustic waves generated by absorption of laser radiation in optically thin cylinders," *J. Acoust. Soc. Am.*, vol. 94, pp. 931–940, 1993.
- [15] M. I. Khan and G. J. Diebold, "The photoacoustic effect generated by an isotropic solid sphere," *Ultrasonics*, vol. 33, pp. 265–269, 1995.
- [16] R. R. Anderson and J. A. Parrish, "Selective photothermolysis: Precise microsurgery by selective absorption of pulsed radiation," *Science*, vol. 220, pp. 524–527, 1983.
- [17] W. Lauterborn and W. Hentschel, "Cavitation bubble dynamics studied by high speed photography and holography: part one," *Ultrasonics*, vol. 9, pp. 260–267, 1985.
- [18] A. Vogel and W. Lauterborn, "Acoustic transient generation by laser-produced cavitation bubbles near solid boundaries," *J. Acoust. Soc. Am.*, vol. 84, pp. 719–731, 1988.
- [19] A. Vogel, P. Schweiger, A. Frieser, M. N. Asiyó, and R. Birngruber, "Intraocular end:yag laser surgery: Light-tissue interaction, damage range, and reduction of collateral effects," *IEEE J. of Quant. Elec.*, vol. 26, pp. 2240–2260, 1990.
- [20] E. D. Jansen, T. H. Le, and A. J. Welch, "Excimer, ho:yag, and q-switched ho:yag ablation of aorta: a comparison of temperatures and tissue damage *in vitro*," *Appl. Optics*, vol. 32, pp. 526–534, 1993.
- [21] E. D. Jansen, T. Asshauer, M. Frenz, M. Motamedi, G. Delacrétaz, and A. J. Welch, "Effect of pulse duration on bubble formation and laser-induced pressure waves during holmium laser ablation," *Lasers in Surg. and Med.*, vol. 18, pp. 278–293, 1996.
- [22] H. Shangguan, L. W. Casperson, A. Shearin, K. W. Gregory, and S. A. Prahl, "Drug delivery with microsecond laser pulses into gelatin," *Appl. Optics*, vol. 35, pp. 3347–3357, 1996.

- [23] H. Shangguan, , K. W. Gregory, L. W. Casperson, and S. A. Prahl, “Enhanced laser thrombolysis with photomechanical drug delivery: An in vitro study,” *Lasers in Surg. and Med.*, vol. 23, pp. 151–160, 1998.
- [24] A. A. Oraevsky, S. L. Jacques, and F. K. Tittel, “Determination of tissue optical properties by piezoelectric detection of laser-induced stress waves,” *Laser-Tissue Interactions IV, SPIE Proceedings*, vol. 1882, pp. 86–101, 1993.
- [25] A. A. Oraevsky, S. L. Jacques, R. O. Esenaliev, and F. K. Tittel, “Laser-based optoacoustic imaging in biological tissues,” *Laser-Tissue Interactions V, SPIE Proceedings*, vol. 2134, pp. 122–128, 1994.
- [26] A. A. Oraevsky, R. Esenaliev, F. K. Tittel, M. Ostermeyer, L. Wang, and S. L. Jacques, “Laser opto-acoustic imaging of turbid media: determination of optical properties by comparison with diffusion theory and monte carlo simulations,” *Laser-Tissue Interactions VII, SPIE Proceedings*, vol. 2681, pp. 277–284, 1996.
- [27] G. Paltauf, H. Schmidt-Kloiber, and H. Guss, “Light distribution measurements in absorbing materials by optical detection of laser-induced stress waves,” *Appl. Phys. Lett.*, vol. 69, pp. 1526–1528, 1996.
- [28] G. Paltauf and H. Schmidt-Kloiber, “Measurement of laser-induced acoustic waves with a calibrated optical transducer,” *J. Appl. Phys.*, vol. 82, pp. 1525–1531, 1997.
- [29] G. Paltauf and H. Schmidt-Kloiber, “Optical method for two-dimensional ultrasonic detection,” *Appl. Phys. Lett.*, vol. 75, pp. 1–3, 1999.
- [30] G. Paltauf, H. Schmidt-Kloiber, K. P. Kostli, M. Frenz, and H. P. Weber, “Optoacoustic imaging using two-dimensional ultrasonic detection,” *Biomedical Optoacoustics, SPIE Proceedings*, vol. 3916, pp. 240–248, 2000.
- [31] S. L. Jacques, P. E. Andersen, S. G. Hanson, and L. R. Lindvold, “Non-contact detection of laser-induced acoustic waves from buried absorbing objects using a dual-beam common-path interferometer,” *Laser-Tissue Interactions IX, SPIE Proceedings*, vol. 3254, pp. 307–318, 1998.
- [32] P. E. Andersen, S. G. Hanson, and S. L. Jacques, “Photoacoustic imaging of buried objects using an all-optical detection scheme,” *Laser-Tissue Interactions IX, SPIE Proceedings*, vol. 3601, pp. 303–309, 1999.
- [33] P. C. Beard and T. N. Mills, “Extrinsic optical fiber ultrasound sensor using a thin polymer film as a low-finesse fabry-perot interferometer,” *Appl. Optics*, vol. 35, pp. 663–675, 1996.

- [34] P. C. Beard and T. N. Mills, "Miniature optical fibre ultrasonic hydrophone using a fabry-perot polymer film interferometer," *Electron. Lett.*, vol. 33, 19.
- [35] P. C. Beard, F. Pérennès, E. Draguioiti, and T. N. Mills, "Optical fiber photoacoustic-photothermal probe," *Optics Lett.*, vol. 23, pp. 1235–1237, 1998.
- [36] P. C. Beard and T. N. Mills, "Optical detection system for biomedical photoacoustic imaging," *Biomedical Optoacoustics, SPIE Proceedings*, vol. 3916, pp. 100–109, 2000.
- [37] E. Jacobs, *Medical Imaging: A Concise Textbook*. Igaku-Shoin, 1987.
- [38] K. M. Mudry, "Imaging," in *The Biomedical Engineering Handbook* (J. D. Bronzino, ed.), pp. 949–951, Boca Raton, FL: CRC Press, 1995.
- [39] J. R. E. Shroy, M. S. V. Lysel, and M. J. Yaffe, "X-ray," in *The Biomedical Engineering Handbook* (J. D. Bronzino, ed.), pp. 953–989, Boca Raton, FL: CRC Press, 1995.
- [40] I. A. Cunningham and P. F. Judy, "Computed tomography," in *The Biomedical Engineering Handbook* (J. D. Bronzino, ed.), pp. 990–1005, Boca Raton, FL: CRC Press, 1995.
- [41] M. Born and E. Wolf, *Principles of Optics*. Cambridge University Press, 1999.
- [42] J. Weir and P. H. Abrahams, *An Imaging Atlas of Human Anatomy*. Mosby-Wolfe, 1992.
- [43] J. R. J. Bartrum and H. C. Crow, *Real Time Ultrasound: A Manual for Physicians and Technical Personnel*. W. B. Saunders Co., 1983.
- [44] S. L. Hagen-Ansert, *Textbook of Diagnostic Ultrasonography*. The C. V. Mosby Co., 1989.
- [45] R. L. Goldberg, S. W. Smith, J. G. Mottley, and K. W. Ferrara, "Ultrasound," in *The Biomedical Engineering Handbook* (J. D. Bronzino, ed.), pp. 1077–1118, Boca Raton, FL: CRC Press, 1995.
- [46] K. L. Moore, *Clinically Oriented Anatomy*. Williams & Wilkins, 1992.
- [47] V. G. Andreev, A. A. Karabutov, S. V. Solomatin, E. V. Savateeva, V. Aleynikov, Y. V. Zhulina, R. Fleming, and A. A. Oraevsky, "Optoacoustic tomography of breast cancer with arc-array transducer," *Biomedical Optoacoustics, SPIE Proceedings*, vol. 3916, pp. 36–47, 2000.

- [48] J. R. A. Kruger and W. L. Kiser, K. D. Miller, H. E. Reynolds, D. R. Reinecke, G. A. Kruger, and P. J. Hofacker, "Thermoacoustic ct: imaging principles," *Biomedical Optoacoustics, SPIE Proceedings*, vol. 3916, pp. 150–159, 2000.
- [49] J. A. Viator, G. Paltauf, S. L. Jacques, and S. A. Prahl, "Localization of spherical photoacoustic sources in acrylamide gels using time domain measurements," *Biomedical Optoacoustics, SPIE Proceedings*, vol. 3916, pp. 89–99, 2000.
- [50] S. L. Jacques, J. A. Viator, and G. Paltauf, "Optoacoustic imaging of tissue blanching during photodynamic therapy of esophageal cancer," *Biomedical Optoacoustics, SPIE Proceedings*, vol. 3916, pp. 322–330, 2000.
- [51] A. Rosencwaig, "Noninvasive monitoring of glucose and other biological compounds with a thermal wave assisted technique," *Biomedical Optoacoustics, SPIE Proceedings*, vol. 3916, pp. 2–8, 2000.
- [52] A. A. Bednov, A. A. Karabutov, E. V. Savateeva, W. F. March, and A. A. Oraevsky, "Monitoring glucose in vivo by measuring laser-induced acoustic profiles," *Biomedical Optoacoustics, SPIE Proceedings*, vol. 3916, pp. 9–18, 2000.
- [53] R. Fainchtein, B. J. Stoyanov, J. C. Murphy, D. A. Wilson, and D. F. Hanley, "Local determination of hemoglobin concentration and degree of oxygenation in tissue by pulsed photoacoustic spectroscopy," *Biomedical Optoacoustics, SPIE Proceedings*, vol. 3916, pp. 19–33, 2000.
- [54] M. W. Sigrist, A. M. Bohren, I. G. Calasso, M. Naegele, and A. Romann, "Sensitive and selective monitoring of trace gases by laser photoacoustic spectroscopy," *Biomedical Optoacoustics, SPIE Proceedings*, vol. 3916, pp. 286–294, 2000.
- [55] J. Oomens, S. E. Bisson, M. Harting, T. J. Kulp, and F. J. M. Harren, "New laser sources for photoacoustic trace gas detection with applications in biomedical science," *Biomedical Optoacoustics, SPIE Proceedings*, vol. 3916, pp. 295–300, 2000.
- [56] G. Yao and L. V. Wang, "Two-dimensional tissue imaging by use of parallel detection of ultrasound-modulated laser speckles," *Biomedical Optoacoustics, SPIE Proceedings*, vol. 3916, pp. 140–146, 2000.
- [57] P. M. Morse, *Vibration and Sound*. AIP Press, 1981.
- [58] M. J. Crocker, "Introduction," in *Handbook of Acoustics* (M. J. Crocker, ed.), pp. 3–20, New York: John Wiley & Sons, Inc., 1998.

- [59] A. D. Pierce, "Mathematical theory of wave propagation," in *Handbook of Acoustics* (M. J. Crocker, ed.), pp. 21–38, New York: John Wiley & Sons, Inc., 1998.
- [60] P. M. Morse and K. U. Ingard, *Theoretical Acoustics*. Princeton University Press, 1968.
- [61] J. W. S. Rayleigh, *The Theory of Sound, Vol. I*. Dover Publications, Inc., 1945.
- [62] J. W. S. Rayleigh, *The Theory of Sound, Vol. II*. Dover Publications, Inc., 1945.
- [63] I. Tolstoy and C. S. Clay, *Ocean Acoustics, Theory and Experiment in Underwater Sound*. AIP Press, 1987.
- [64] F. B. Jensen, W. A. Kuperman, M. B. Porter, and H. Schmidt, *Computational Ocean Acoustics*. AIP Press, 1994.
- [65] A. P. Dowling, "Steady-state radiation from sources," in *Handbook of Acoustics* (M. J. Crocker, ed.), pp. 99–118, New York: John Wiley & Sons, Inc., 1998.
- [66] R. Knobel, *An Introduction to the Mathematical Theory of Waves*. American Mathematical Society, 2000.
- [67] L. E. Kinsler, A. B. Coppens, A. R. Frey, and J. V. Sanders, *Fundamentals of Acoustics, 3rd Edition*. John Wiley & Sons, Inc., 1982.
- [68] G. Paltauf and H. Schmidt-Kloiber, "Photoacoustic waves excited in liquids by fiber-transmitted laser pulses," *J. Acoust. Soc. Am.*, vol. 104, pp. 890–897, 1998.
- [69] J. A. Viator, S. L. Jacques, and S. A. Prahl, "Depth profiling of absorbing soft materials using photoacoustic methods," *IEEE J. Sel. Topics Quant. Electron.*, vol. 5, pp. 989–996, 1999.
- [70] F. A. Duck, *Physical Properties of Tissue*. Academic Press, 1990.
- [71] A. Tolstoy, *Matched Field Processing for Underwater Acoustics*. World Scientific, 1993.
- [72] P. N. T. Wells, "Absorption and dispersion of ultrasound in biological tissue," *Ultrasound in Med. and Biol.*, vol. 1, pp. 369–376, 1975.
- [73] J. V. Geleskie and K. K. Shung, "Further studies on acoustic impedance of major bovine blood vessel walls," *J. Acoust. Soc. Am.*, vol. 71, pp. 467–470, 1982.
- [74] C. R. Mol and P. A. Breddels, "Ultrasound velocity in muscle," *J. Acoust. Soc. Am.*, vol. 71, pp. 455–461, 1982.

- [75] R. A. Kruger, "Photoacoustic ultrasound," *Med. Phys.*, vol. 21, pp. 127–131, 1994.
- [76] J. A. Viator, S. L. Jacques, and S. A. Pahl, "Generating subsurface acoustic waves in indocyanine green stained elastin biomaterial using a q-switched laser," *Laser-Tissue Interactions IX, SPIE Proceedings*, vol. 3254, pp. 104–111, 1998.
- [77] A. A. Oraevsky and S. L. Jacques, "Mechanism of laser ablation for aqueous media irradiated under confined-stress conditions," *Appl. Phys.*, vol. 78, pp. 1281–1290, 1995.
- [78] U. S. Sathyam and S. A. Pahl, "Limitations in measurements of subsurface temperatures using pulsed photothermal radiometry," *J. Biomed. Optics*, vol. 2, pp. 251–261, 1997.
- [79] R. S. Crissman, "Comparison of two digestive technique for preparation of vascular networks for sem observation," *J. Electron Microscopy Tech.*, vol. 6, pp. 335–348, 1987.
- [80] H. S. Carslaw and J. C. Jaeger, *Conduction of Heat in Solids*. Oxford University Press, 1959.
- [81] S. L. Jacques, "Laser-tissue interactions: Photochemical, photothermal, and photomechanical," *Lasers in General Surg.*, vol. 72, pp. 531–558, 1992.
- [82] J. A. Viator and S. A. Pahl, "Laser thrombolysis using long pulse frequency-doubled nd:yag lasers," *Lasers in Surg. and Med.*, vol. 25, pp. 379–388, 1999.
- [83] B. C. Wilson and S. L. Jacques, "Optical reflectance and transmittance of tissues: principles and applications," *IEEE J. of Quant. Elec.*, vol. 26, pp. 2186–2199, 1990.
- [84] B. C. Wilson, "Measurement of tissue optical properties: Methods and theories," in *Optical-Thermal Response of Laser-Irradiated Tissue* (A. J. Welch and M. J. C. van Gemert, eds.), pp. 233–274, New York, NY: Plenum Press, 1995.
- [85] B. C. Wilson, "Modeling and measurements of light propagation in tissue for diagnostic and therapeutic applications," in *Laser Systems for Photobiology and Photomedicine* (A. N. Chester, ed.), pp. 13–27, New York, NY: Plenum Press, 1991.
- [86] P. Liu, "Image reconstruction from photoacoustic pressure signals," *Laser-Tissue Interactions VII, SPIE Proceedings*, vol. 2681, pp. 285–296, 1996.
- [87] P. Liu, "The p-transform and photoacoustic image reconstruction," *Phys. Med. Biol.*, vol. 43, pp. 667–674, 1998.

- [88] R. O. Esenaliev, A. A. Karabutov, and A. A. Oraevsky, "Sensitivity of laser opto-acoustic imaging in detection of small deeply embedded tumors," *IEEE J. Sel. Topics Quant. Electron.*, vol. 5, pp. 981–988, 1999.
- [89] S. Heier, K. Rothman, L. Heier, and W. Rosenthal, "Photodynamic therapy for obstructing esophageal cancer: Light dosimetry and randomized comparison with nd:yag laser therapy," *Gastroenterology*, vol. 109, pp. 63–72, 1995.
- [90] J. M. Jr., E. C. Ellison, J. Guy, W. Hicks, J. Jones, L. Laufman, E. May, T. Nims, C. H. Spiridonidis, and T. Williams, "Photodynamic therapy for esophageal malignancy: A prospective twelve-year study," *Ann. Thoracic Surgery*, vol. 62, pp. 1005–1010, 1996.
- [91] C. Lightdale, S. Heier, N. Marcon, J. M. Jr., H. Vgerdes, B. Overholt, M. S. and G. Stiegmann, and H. Nava, "Photodynamic therapy with porfimer sodium versus thermal ablation therapy with nd:yag laser for palliation of esophageal cancer: A multicenter randomized trial," *Gastrointestinal Endoscopy*, vol. 42, pp. 507–512, 1995.
- [92] S. B. Narayan and M. V. S. Jr., "Palliation of esophageal carcinoma," *Chest Surg. Clinics of N. Am.*, vol. 4, pp. 347–367, 1994.
- [93] A. L. Abramson, M. J. Shikowitz, V. M. Mullooly, B. M. Steinberg, C. A. Amella, and H. R. Rothstein, "Clinical effects of photodynamic therapy on recurrent laryngeal papillomas," *Arch. Otolaryngol. Head Neck Surg.*, vol. 118, pp. 25–29, 1992.
- [94] J. Moan and K. Berg, "Photochemotherapy of cancer: experimental research," *Photochemistry and Photobiology*, vol. 55, pp. 931–948, 1992.
- [95] A. D. Nguyen, "Photodynamic therapy with porfimer sodium (photofrin)," *Highlights in Oncology Practice*, vol. 15, pp. 21–24, 1997.
- [96] H. I. Pass, "Photodynamic therapy in oncology: Mechanisms and clinical use," *J. Nat. Cancer Inst.*, vol. 85, pp. 443–456.
- [97] M. D. Daniell and J. S. Hill, "A history of photodynamic therapy," *Aust. N. Z. J. Surg.*, vol. 61, pp. 340–348, 1991.
- [98] S. Landis, T. Murray, S. Bolden, and P. Wingo, "Cancer statistics," *CA-A Cancer J. for Clinicians*, vol. 49, pp. 8–31, 1999.
- [99] H. W. Boyce, "Stents for palliation due to esophageal cancer," *New England J. of Med.*, vol. 18, pp. 1345–1346, 1993.

- [100] M. B. Orringer, B. Marshall, and M. D. Iannettoni, "Transhiatal esophagectomy: clinical experience and refinements," *Ann. of Surg.*, vol. 3, pp. 392–403.
- [101] M. G. Patti, C. U. Corvera, R. E. Glasgow, and L. W. Way, "A hospital's annual rate of esophagectomy influences the operative mortality," *J. of Gastrointestinal Surg.*, vol. 2, pp. 186–192, 1998.
- [102] P. Horowitz and W. Hill, *The Art of Electronics*. Cambridge University Press, 1990.
- [103] J. C. Boyce, *Operational Amplifiers and Linear Integrated Circuits*. PWS–Kent Publishing Co, 1990.
- [104] U. S. Sathyam, A. Shearin, E. A. Chastaney, and S. A. Prahl, "Threshold and ablation efficiency studies of microsecond ablation of gelatin under water," *Lasers in Surg. and Med.*, vol. 19, pp. 397–406, 1996.
- [105] S. T. Flock, S. L. Jacques, B. C. Wilson, W. M. Star, and M. J. C. van Gemert, "Optical properties of intralipid: A phantom medium for light propagation studies," *Lasers in Surg. and Med.*, vol. 12, pp. 510–519, 1992.
- [106] C. Javanaud, R. R. Rahalkar, and P. Richmond, "Measurement of speed and attenuation of ultrasound in egg white and egg yolk," *J. Acoust. Soc. Am.*, vol. 76, pp. 670–675, 1984.

Biographical Note

John Andrew Viator was born in Tokyo, Japan, on August 24, 1964, the son of John Dunis Viator and Fujiko Gomi Viator. He entered the University of Washington in Seattle on a Naval ROTC scholarship in 1981 and received the B.S. in physics in 1985. After serving for four years on active duty as a surface warfare officer, he entered graduate school at the University of Oregon in Eugene, Oregon. He was recalled to active duty for Operation Desert Shield in 1990, where he served with the Military Sealift Command in the Persian Gulf Theater. He returned to the University of Oregon, where he earned the M.S. in mathematics in 1993. He entered the Oregon Graduate Institute of Science and Technology in 1995, where he received the M.S. in applied physics in 1997.

Permanent address: 8115 NE 100th St
Vancouver, WA 98662

This dissertation was typed by the author and typeset in L^AT_EX.